

**OPTIMIZATION OF GPU THERMAL MANAGEMENT VIA RESPONSE  
SURFACE METHODOLOGY (RSM) ANALYSIS**



**UNIVERSITI TEKNIKAL MALAYSIA MELAKA**

**OPTIMIZATION OF GPU THERMAL MANAGEMENT VIA RESPONSE  
SURFACE METHODOLOGY (RSM) ANALYSIS**

**LIM CHIN HUI**



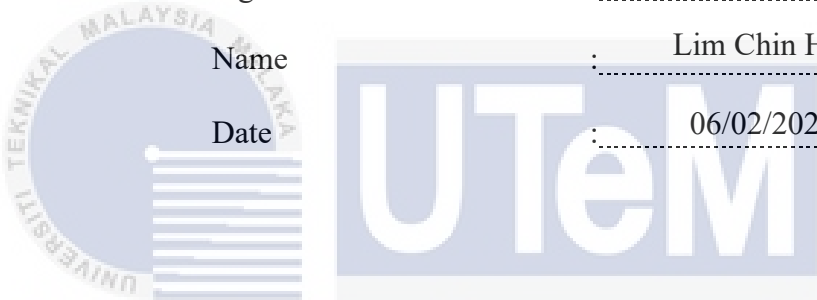
**UNIVERSITI TEKNIKAL MALAYSIA MELAKA**

**2024**

## DECLARATION

I declare that this project report entitled “Optimization of GPU Thermal Management Via Response Surface Methodology (RSM) Analysis” is the result of my own work except as cited in the reference.

|           |   |   |
|-----------|---|---|
| Signature | : |  |
| Name      | : | Lim Chin Hui  |
| Date      | : | 06/02/2024  |

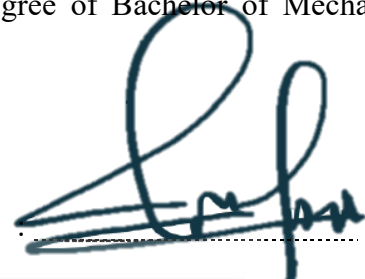


اونيورسيتي تيكنيكل مليسيا ملاك  
UNIVERSITI TEKNIKAL MALAYSIA MELAKA

## APPROVAL

I hereby declare that I have read this project report and in my opinion this report is sufficient in terms of scope and quality for the award of the degree of Bachelor of Mechanical Engineering.

Signature



Name of Supervisor

: Dr. Muhammad Zuffattah Bin Zakaria

Date

6/2/2024



اونيورسيتي تيكنيكل مليسيا ملاك

UNIVERSITI TEKNIKAL MALAYSIA MELAKA

## DEDICATION

I'm grateful to my parents, friends, and everyone else that assisted with this project. This was unforgettable. I'd like to thank Dr. Muhammad Zulfattah Bin Zakaria, my distinguished project supervisor, for his time brainstorming, reading, encouraging, directing, and, most importantly, being patient. The dissertation would not have been completed without his guidance and support.

This dissertation is also dedicated to the numerous friends and family members who have provided unwavering support over the entirety of this research endeavour. I am deeply grateful for the invaluable contributions made by Mr Nor Izwan Bin Junoh, who graciously facilitated my research endeavours and readily offered any necessary support. I consistently express gratitude for the actions they have undertaken.

I'd like to thank my supervisor, Dr. Muhammad Zulfattah Bin Zakaria, for his direction, encouragement, and patience throughout this research. Sorry for whatever trouble I caused during this study.

I dedicate this work to my dearest friend, Khaw Khai Yung, who supported me throughout this project. You guys are my biggest fans. Finally, I'm writing this for my committed faculty, project panels, teachers, and dean, who have taught me so much. Many thanks for your assistance.

## ABSTRACT

The recent rapid progress in information technology (IT) has highlighted the negative impact of excessive temperatures on computer systems, particularly the GPU. This can significantly impair the device's performance and reduce its lifespan. Presently, GPU cooling systems utilise two distinct cooling methods: active and passive cooling. Therefore, it is imperative to have a robust cooling system in order to effectively dissipate heat. Hence, it is imperative to do thorough research and innovate novel cooling systems that are more efficient. This study aims to address the knowledge gaps regarding GPU thermal regulation by specifically examining the influence of fan speed on GPU temperatures. The investigation will be conducted under identical GPU load situations. The GPU stress indicated pertains to the Dagger-Hashimoto mining algorithm. Additionally, there are three distinct thermal pad materials: silicone, nickel, and copper. These materials were examined to analyse the thermal regulation of the GPU while also considering the impact of fan speed. The employed model consists of a sandwich structure consisting of a microchip, a thermal pad, and a heat sink. The study utilised the response surface methodology (RSM) with a single factor to forecast the ideal fan speeds necessary to achieve certain temperatures. To ensure the accuracy of the model, we conducted additional experiments to assess how the suggested GPU temperature affects the fan speed, as predicted by the RSM model. For the given scenario, the most accurate prediction for the GPU temperature of the stock thermal pad, specifically the Arctic TP-3, is achieved using a quartic model. Conversely, the most accurate prediction for the nickel thermal pad can be achieved by employing a quartic model for the GPU core

temperature and a cubic model for the GPU memory temperature. The cubic model of a copper thermal pad is the most appropriate form for determining GPU temperature. When evaluating the accuracy of the chosen model, three categories of materials displayed a margin of error below 5%, with the highest error being a mere 1.62%. Furthermore, it has been discovered that employing a copper thermal pad remains an advantageous option for intensive activities such as gaming, cryptocurrency mining, and similar duties. It efficiently reduces the temperature of the memory, even when the fan speeds are modest, leading to energy savings on the cooling system while still maintaining a high hash rate.



## ABSTRAK

*Perkembangan pesat dalam era kontemporari ini dalam teknologi maklumat (IT) telah menonjolkan kesan negatif peningkatan suhu pada sistem komputer, terutamanya GPU. Ini boleh menjejaskan prestasi peranti dan mengurangkan jangka hayatnya. Pada masa ini, sistem penyejukan GPU menggunakan dua kaedah penyejukan yang berbeza iaitu penyejukan aktif dan pasif. Oleh itu, ia adalah penting untuk mempunyai sistem penyejukan yang teguh untuk mengalihkan panas secara berkesan. Oleh itu, ia adalah penting untuk melakukan penyelidikan menyeluruh dan inovasi sistem penyejukan baru yang lebih berkesan. Kajian ini bertujuan untuk mengatasi kesenjangan pengetahuan mengenai kawalan haba GPU dengan mengkaji secara khusus pengaruh kelajuan kipas pada suhu GPU. Penyelidikan akan dijalankan di bawah keadaan beban GPU yang sama. Tekanan GPU yang dinyatakan berkaitan dengan algoritma perlombongan Dagger-Hashimoto. Selain itu, terdapat tiga bahan pad haba yang berbeza: silikon, nikel, dan tembaga. Bahan-bahan ini telah diperiksa untuk menganalisis kawalan haba GPU sambil juga mempertimbangkan kesan kelajuan kipas angin. Model yang digunakan terdiri daripada struktur sandwich yang terdiri daripada mikrochip, pad haba, dan sinki haba. Kajian ini menggunakan kaedah permukaan respons (RSM) dengan faktor tunggal untuk meramalkan kelajuan kipas ideal yang diperlukan untuk mencapai suhu tertentu. Untuk memastikan ketepatan model, kami menjalankan eksperimen tambahan untuk menilai bagaimana suhu GPU yang disyorkan mempengaruhi kelajuan optimal, seperti yang diramalkan oleh model RSM. Untuk senario yang diberikan, ramalan yang paling tepat untuk suhu GPU pad haba*

*stok ataupun silikon, khususnya Arctic TP-3, dicapai menggunakan model kuartik. Sebaliknya, ramalan yang paling tepat untuk pad haba nikel boleh dicapai dengan menggunakan model kuartik untuk suhu teras GPU dan model kubik untuk suhu memori GPU. Model kubik pad haba tembaga adalah model yang paling sesuai untuk menentukan suhu GPU. Apabila menilai ketepatan model yang dipilih, tiga kategori bahan menunjukkan margin kesalahan di bawah 5%, dengan kesilapan tertinggi hanya 1.62%. Selain itu, telah ditemui bahawa menggunakan pad haba tembaga kekal pilihan yang menguntungkan untuk aktiviti intensif seperti permainan, perlombongan cryptocurrency, dan tugas-tugas serupanya. Ia secara berkesan mengurangkan suhu memori, walaupun pada kelajuan kipas sederhana, turut membawa kepada penjimatan tenaga pada sistem penyejukan sambil mengekalkan kadar hash yang tinggi.*



## ACKNOWLEDGEMENT

Dr. Muhammad Zulfattah Bin Zakaria, my advisor, deserves the utmost gratitude for allowing me to work on this subject for my dissertation. With his help, I was able to complete my dissertation successfully. Whenever I was in a sticky situation, he was the first person I turned to for sound advice and direction. I appreciated the time and effort put into guiding me through this task.

Second, I'd like to express my gratitude to the lab assistant, Mr Nor Izwan Bin Junoh, who was always there to help me out with any technical issues I was having. He'd go out of his way to help me out with things like getting an air gun so that I could blow the dust off from my graphics processing unit (GPU) specimen. I'd also like to express my appreciation for the time he saved me by advising when it would be best to use the laboratory equipment.

I would like to thank my coursemates for offering me their support, patience, and motivation. God, too, deserves my gratitude for helping me weather these storms. I'd like to end by expressing my gratitude to my loved ones.

## TABLE OF CONTENTS

|  |              |
|--|--------------|
| <b>DECLARATION</b>   | <b>i</b>     |
| <b>APPROVAL</b>  | <b>ii</b>    |
| <b>DEDICATION</b>  | <b>iii</b>   |
| <b>ABSTRACT</b>  | <b>iv</b>    |
| <b>ABSTRAK</b>   | <b>vi</b>    |
| <b>ACKNOWLEDGEMENT</b>   | <b>viii</b>  |
| <b>TABLE OF CONTENTS</b>   | <b>ix</b>    |
| <b>LIST OF TABLES</b>  | <b>xiii</b>  |
| <b>LIST OF FIGURES</b>   | <b>xvi</b>   |
| <b>LIST OF ABBEREVATIONS</b>   | <b>xx</b>    |
| <b>LIST OF SYMBOLS</b>   | <b>xxii</b>  |
| <b>LIST OF APPENDICES</b>  | <b>xxiii</b> |
| <b>CHAPTER 1 INTRODUCTION</b>  | <b>1</b>     |
| 1.1 Background Study   | 1            |
| 1.2 Problem Statement  | 4            |
| 1.3 Objectives   | 5            |
| 1.4 Scope of Study   | 6            |
| <b>CHAPTER 2 LITERATURE REVIEW</b>   | <b>7</b>     |
| 2.0 Overview   | 7            |
| 2.1 Introduction of Graphic Processing Unit (GPU)  | 8            |
| 2.2 Thermal Management of GPU under Computational Fluid Dynamics Simulation                                    | 9            |
| 2.3 GPU Cooling System   | 17           |
| 2.4 Fan-cooling  | 17           |
| 2.4.1 Study of Glass Fibre Reinforced Plastic on Fan Blades  | 18           |
| 2.4.2 Study of short inlet duct cooling fan design on aerodynamic noise reduction                              | 23           |
| 2.4.3 Study of fan blade sweep angle on aerodynamic fan noise production rate.                                 | 25           |
| 2.4.4 Aerodynamic and structural multidisciplinary optimization of fan rotors towards aerodynamic performance. | 30           |

|         |  |    |
|---------|--|----|
| 2.4.5   | Experimental study on blade thickness on the overall and local performance of axial-flow fan   | 34 |
| 2.5     | Liquid Cooling   | 36 |
| 2.5.1   | Performance analysis and structural optimization of a finned liquid-cooling radiator for chip heat dissipation                         | 40 |
| 2.5.2   | Evaluation of Water-Cooling Heat Sink Performance and Dynamic Flow Effect  | 44 |
| 2.5.3   | Study of an adjustable closed-loop liquid-based thermoelectric electronic cooling system (LTEEC) for variable load thermal management. | 45 |
| 2.6     | Heat Sink  | 48 |
| 2.6.1   | Studies of material used in Heat Pipe  | 49 |
| 2.6.2   | Study on the thermal dissipation performance of GPU cooling system with nanofluid as coolant   | 54 |
| 2.6.3   | Study of heat transport behaviour of micro channel heat sink with graphene based nanofluids  | 57 |
| 2.6.4   | Numerical and experimental models study on flat and embedded heat pipes applied in high-end VGA card cooling system                    | 63 |
| 2.7     | Mode of Heat Transfer  | 64 |
| 2.8     | Basic of thermal resistance and heat dissipation   | 67 |
| 2.9     | Crypto Mining  | 68 |
| 2.9.1   | Crypto Exchange Platform   | 69 |
| 2.9.2   | Introduction to NiceHash   | 70 |
| 2.9.2.1 | NiceHash Miner   | 71 |
| 2.9.2.2 | Crypto Mining Algorithms   | 71 |
| 2.9.2.3 | DaggerHashimoto Mining Algorithm   | 73 |
| 2.9.2.4 | ETCHash Mining Algorithm   | 74 |
| 2.9.2.5 | Autolykos Mining Algorithm   | 74 |
| 2.9.2.6 | KAWPOW Mining Algorithm  | 74 |
| 2.9.2.7 | Neoscrypt Mining Algorithm   | 75 |
| 2.10    | Introduction to Design Expert  | 75 |
| 2.10.1  | Introduction to Response Surface Methodology (RSM)   | 76 |
| 2.10.2  | Introduction to Factorial Design   | 78 |
| 2.10.3  | Introduction to Mixture Design   | 79 |

|   |            |
|---|------------|
| 2.10.4 Introduction to Combined Design  | 81         |
| <b>CHAPTER 3 METHODOLOGY</b>  | <b>83</b>  |
| 3.0 Introduction  | 83         |
| 3.1 Literature Review   | 83         |
| 3.2 General Methodology of PSM  | 85         |
| 3.3 Initial stages of setting up the experiment   | 86         |
| 3.4 Graphic Processing Unit (GPUs) selection  | 89         |
| 3.4.1 Specifications pertaining to the ASUS TUF Gaming 3060   | 92         |
| 3.4.2 ASUS TUF GAMING 3060 GPU Mining Setting   | 93         |
| 3.4.3 Setup of the Nicehash miner prior to testing  | 95         |
| 3.5 Variable fan speed impact upon GPU temperature under identical GPU load and RSM Analysis optimal fan speed prediction validation                  | 96         |
| 3.6 Variable material of thermal pad on thermal dissipation performance of GPU memory by utilizing RSM analysis                                       | 99         |
| 3.7 Performing Response Surface Methodology (RSM) analysis  | 104        |
| 3.8 Summary   | 106        |
| <b>CHAPTER 4 RESULTS AND DISCUSSION</b>   | <b>107</b> |
| 4.0 Overview of RSM analysis  | 107        |
| 4.1 Results of Design of Experiments (DOE) for variable fan speed under identical GPU load  | 108        |
| 4.1.1 Optimization of GPU core temperature-dependent fan speed via response surface-based Response Surface Methodology (RSM) with a single factor     | 108        |
| 4.1.2 Optimization of GPU memory temperature-dependent fan speed via response surface-based Response Surface Methodology (RSM) with a single factor   | 119        |
| 4.2 Results of RSM analysis of Nickel thermal pad on GPU core and memory temperature  | 128        |
| 4.2.1 Optimization of GPU Core Temperature on nickel thermal pad via response surface-based Response Surface Methodology (RSM) with a single factor   | 128        |
| 4.2.2 Optimization of GPU memory temperature on nickel thermal pad via response surface-based Response Surface Methodology (RSM) with a single factor | 139        |
| 4.3 Results of RSM analysis of copper thermal pad on GPU core and memory temperature  | 144        |

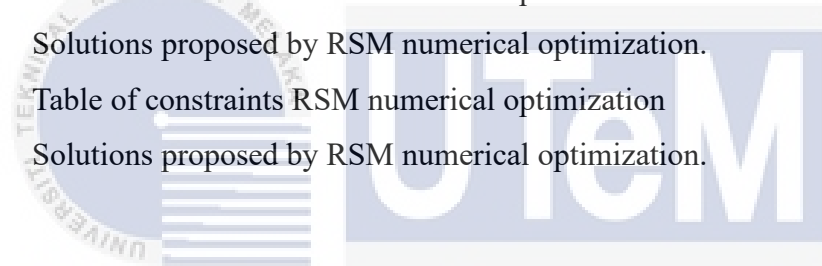
|   |            |
|---|------------|
| 4.3.1 Optimization of GPU Core Temperature on nickel thermal pad via response surface-based Response Surface Methodology (RSM) with a single factor           | 144        |
| 4.3.2 Optimization of GPU memory temperature on copper thermal pad via response surface-based Response Surface Methodology (RSM) with a single factor         | 151        |
| 4.4 Discussion on the GPU core and memory temperature achieved by various thermal pad material.   | 156        |
| 4.5 Verification and validation of GPU core and memory temperatures in accordance with the RSM mathematical model's optimised fan speed.                      | 159        |
| 4.5.1 Verification on GPU Core Temperature and memory temperature for stock thermal pad in accordance with the RSM mathematical model's optimised fan speed.  | 159        |
| 4.5.2 Verification on GPU Core Temperature and memory temperature for nickel thermal pad in accordance with the RSM mathematical model's optimised fan speed. | 160        |
| 4.5.3 Verification on GPU Core Temperature and memory temperature for copper thermal pad in accordance with the RSM mathematical model's optimised fan speed. | 162        |
| <b>CHAPTER 5 CONCLUSION AND RECOMMENDATIONS</b>   | <b>164</b> |
| 5.1 Conclusions   | 164        |
| 5.2 Recommendations for future study  | 166        |
| <b>REFERENCES</b>   | <b>167</b> |
| <b>APPENDIX A</b>   | <b>177</b> |

## LIST OF TABLES

| <b>TABLE</b> | <b>TITLE</b>   | <b>PAGE</b> |
|--------------|--|-------------|
| 2.1          | Material for each component  | 11          |
| 2.2          | Maximum temperature of heat sink for different velocity  | 13          |
| 2.3          | Initial & final temperatures of each heat sink.  | 15          |
| 2.4          | Tensile Properties of composites.  | 19          |
| 2.5          | Laminate designation for various cases   | 21          |
| 2.6          | Tensile stress obtained from tension test vs ANSYS R19.2 results                                 | 21          |
| 2.7          | Comparison of the experimental and numerical results for the mass flow rate                      | 26          |
| 2.8          | Comparison of experimental and numerical results for OASPL                                       | 27          |
| 2.9          | The main design parameter of the fan stage   | 31          |
| 2.10         | Physical properties of aluminium alloy   | 32          |
| 2.11         | Grid sensitivity analysis of fan rotor stress  | 32          |
| 2.12         | Comparison of design point performance of Baseline, Optimization A, and Optimization B           | 33          |
| 2.13         | Blade cascade parameters for the reference <i>FA</i>   | 35          |
| 2.14         | Summary of the application of nanofluid or hybrid nanofluid in the liquid cooling system for CPU | 38          |
| 2.15         | Applications of nanofluid or hybrid nanofluid with heat transfer coefficient                     | 39          |
| 2.16         | Thermal conductivity of nanoparticles  | 40          |
| 2.17         | Equipment parameters used in the experimental water-cooling system                               | 42          |
| 2.18         | Main parameters of heat sink   | 44          |
| 2.19         | Compatible and Incompatible materials suitable for different working fluids                      | 50          |
| 2.20         | Heat Pipe Temperature Range  | 51          |
| 2.21         | Working fluids used in heat pipe   | 52          |

|      |   |     |
|------|---|-----|
| 2.22 | Summarization of research done on material for container, wick structure and working fluid combinations   | 53  |
| 2.23 | Experimental results for the embedded heat pipe thermal module  | 64  |
| 3.1  | Specifications comparison between RTX 30 series GPU   | 91  |
| 3.2  | Specifications of ASUS TUF GAMING 3060  | 93  |
| 3.3  | RTX 3060 ETChash Mining Overclocks setting  | 94  |
| 3.4  | Completed RSM fan speed optimisation experiment design.   | 99  |
| 3.5  | Detail Specification of original, nickel and copper thermal pad   | 100 |
| 3.6  | Performance Comparison between Arctic MX4, MX5 & MX6.   | 102 |
| 3.7  | General Specification of Thermal Paste Arctic MX4   | 102 |
| 4.1  | Results of Design of Experiments for variable fan speed on original thermal pad.                          | 108 |
| 4.2  | Model Evaluation of Quartic Order for GPU Core and Memory Temperature                                     | 109 |
| 4.3  | Summary of Statistics of various models for GPU Core Temperature  | 110 |
| 4.4  | ANOVA outcome for the suggested cubic model on GPU Core Temperature                                       | 111 |
| 4.5  | ANOVA outcome for the suggested quartic model on GPU Core Temperature                                     | 115 |
| 4.6  | Summary of Statistics of various models for GPU Memory Temperature  | 119 |
| 4.7  | ANOVA outcome for the suggested cubic model on GPU Memory Temperature                                     | 120 |
| 4.8  | ANOVA outcome for the suggested quartic model on GPU Memory Temperature                                   | 124 |
| 4.9  | Results of Design of Experiments for variable fan speed on nickel thermal pad.                            | 128 |
| 4.10 | Model Evaluation of Quartic Order for GPU Core and Memory Temperature on nickel thermal pad.              | 129 |
| 4.11 | Summary of Statistics of various models for GPU Core Temperature  | 130 |
| 4.12 | ANOVA outcome for the suggested cubic model on GPU Core Temperature on nickel thermal pad                 | 131 |
| 4.13 | ANOVA outcome for the suggested quartic model of GPU Core Temperature on nickel thermal pad               | 135 |
| 4.14 | Summary of statistical data on GPU memory temperature across different models using a nickel thermal pad. | 139 |
| 4.15 | ANOVA outcome for the suggested cubic model on GPU Memory Temperature                                     | 140 |

|      |   |     |
|------|---|-----|
| 4.16 | Results of Design of Experiments for variable fan speed on copper thermal pad.                            | 144 |
| 4.17 | Model Evaluation of Quartic Order for GPU Core and Memory Temperature on copper thermal pad.              | 145 |
| 4.18 | Summary of Statistics of various models for GPU Core Temperature on copper thermal pad                    | 146 |
| 4.19 | ANOVA outcome for the suggested cubic model on GPU Core Temperature on copper thermal pad                 | 147 |
| 4.20 | Summary of statistical data on GPU memory temperature across different models using a copper thermal pad. | 151 |
| 4.21 | ANOVA outcome for the suggested cubic model on GPU Memory Temperature                                     | 152 |
| 4.22 | Table of constraints RSM numerical optimization   | 159 |
| 4.23 | Solutions proposed by RSM numerical optimization.   | 159 |
| 4.24 | Table of constraints RSM numerical optimization   | 161 |
| 4.25 | Solutions proposed by RSM numerical optimization.   | 161 |
| 4.26 | Table of constraints RSM numerical optimization   | 162 |
| 4.27 | Solutions proposed by RSM numerical optimization.   | 162 |



اونيورسيتي تيكنيكل مليسيا ملاك

UNIVERSITI TEKNIKAL MALAYSIA MELAKA

## LIST OF FIGURES

| FIGURE | TITLE   | PAGE |
|--------|---|------|
| 2.1    | Example of GPU  | 9    |
| 2.2    | Three heat sink case studies  | 10   |
| 2.3    | Boundary conditions   | 10   |
| 2.4    | Components of GPU   | 11   |
| 2.5    | Temperature contours on heat sink   | 12   |
| 2.6    | Heat transfer performance against number of fins  | 13   |
| 2.7    | Graph of relationship between convective heat transfer coefficients against air velocity.   | 14   |
| 2.8    | Temperature distribution contour of each heat sink for speed $1\text{ms}^{-1}$ at different time interval.  | 15   |
| 2.9    | Temperature distribution in CPU case with time interval $t = 100\text{ s}, 200\text{ s}, 300\text{ s}, 400\text{ s}, 500\text{ s}.$   | 16   |
| 2.10   | Axial Flow Fans   | 18   |
| 2.11   | Layer Sequence of GFRP blade material [CSM/(GR/WR) <sub>4</sub> /UD/(WR/GR) <sub>2</sub> ]  | 19   |
| 2.12   | Layout Sequence of blade material with and without woven jute reinforcements [CSM/(GR/WR) <sub>4</sub> /UD/(WR/GR) <sub>2</sub> ]   | 20   |
| 2.13   | Shear Strength from experiment  | 20   |
| 2.14   | Axial Young's modulus of 32 cases by CLT  | 22   |
| 2.15   | Typical cooling fan configuration   | 24   |
| 2.16   | Picture of installation method for the short inlet duct   | 24   |
| 2.17   | Geometries of automotive cooling fan: (a) definition of sweep angle of fan. (b) straight fan with no sweep angle, (c) swept fan with 45 degrees forward sweep angle, and (d) swept fan with 45 degrees backward sweep angle | 26   |
| 2.18   | Overall A-weighted sound pressure levels of the straight, forward- and backward-swept fans depending on rotational speeds (filled symbol: experimental results, open symbol: numerical prediction)                          | 27   |

|      |   |    |
|------|---|----|
| 2.19 | Velocity vector in the xz plane: (a) backward and (b) forward-swept fans.   | 28 |
| 2.20 | Velocity vector in the xy plane: (a) backward and (b) forward-swept fans.   | 28 |
| 2.21 | Averaged noise contributions at the observer: (a) backward and (b) forward-swept fans.  | 29 |
| 2.22 | Time derivative of the surface pressure on backward-swept fan depending on the azimuth angles: (a) 0 degree, (b) 10 degrees, and (c) 20 degrees                 | 30 |
| 2.23 | Time derivative of the surface pressure on forward-swept fan depending on the azimuth angles: (a) 0 degree, (b) 10 degrees, and (c) 20 degrees                  | 30 |
| 2.24 | Grid and stress distribution diagram for fan motor FEM analysis   | 32 |
| 2.25 | Comparison of the static stress of Baseline, Optimization A, and Optimization B   | 34 |
| 2.26 | Views of the two fans, Front view, sections of thick and thin profiles at various span locations and thickness distribution law along the meridional coordinate | 35 |
| 2.27 | Schematic diagram of water cooling block channel  | 37 |
| 2.28 | Flow chart of the optimization procedure  | 41 |
| 2.29 | Thermal resistance and pressure drop of the radiator under different inlet and outlet modes   | 42 |
| 2.30 | Thermal resistance and pressure drop for different areas of the fin-covered plate for the radiator.   | 43 |
| 2.31 | Structure of heat sink (1) Drop-shaped pin fin, (2) Circle pin fin, (3) Square pin fin  | 44 |
| 2.32 | Comparison between the commercial and the proposed LTEEC system for heater input power of 16.7W and the cooling system power of 5.4W                            | 46 |
| 2.33 | Comparison between different power inputs to proposed LTEEC system  | 47 |
| 2.34 | Variation of GPU temperature for de-ionized water as coolant.   | 55 |
| 2.35 | Variation of GPU temperature for Ag nanofluid as coolant.   | 55 |
| 2.36 | Variation of thermal resistance for de-ionized water as coolant.  | 56 |
| 2.37 | Variation of thermal resistance for Ag nanofluid as coolant.  | 57 |
| 2.38 | Thermal conductivity variation for GnP  | 59 |
| 2.39 | Variation of Nusselt number at different vol%   | 60 |
| 2.40 | Variation of pressure drop at different vol %   | 61 |
| 2.41 | Variations of pressure drop at different vol%   | 61 |
| 2.42 | Variation of thermal entropy generation rate. (left) Varying heat load at 0 vol%, (Right) Varying heat load at 0.2 vol%   | 62 |
| 2.43 | Operation and services provided by NiceHash.  | 70 |

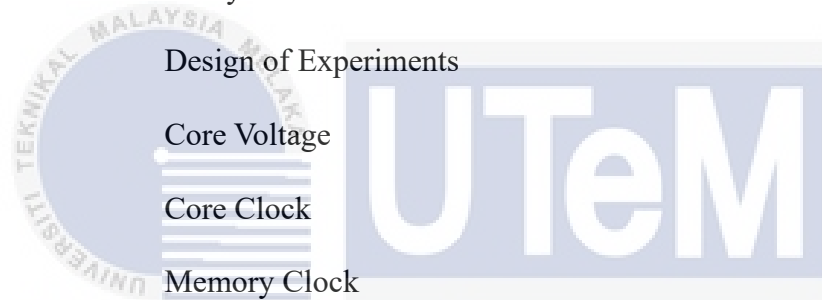
|      |  |     |
|------|--|-----|
| 3.1  | General Methodology of PSM.  | 85  |
| 3.2  | Graphics processing unit (GPU) fan speed and radiator heatsink material experiment flowchart                                   | 88  |
| 3.3  | Physical appearance of ASUS TUF GAMING 3060  | 92  |
| 3.4  | GPU Mining Setting through MSI Afterburner   | 94  |
| 3.5  | Initial GPU core and memory temperature checks.  | 95  |
| 3.6  | Method to log GPU temperature before and after the test.   | 96  |
| 3.7  | RSM sequence for the GPU fan speed optimization.   | 97  |
| 3.8  | Single-factor RSM input for 550–3000 rpm fan speed.  | 98  |
| 3.9  | The disassembled ASUS TUG GAMING 3060  | 100 |
| 3.10 | Placement location of nickel thermal pad on GPU PCB.   | 101 |
| 3.11 | Thermal Paste covered area for GPU on different thermal pad materials.   | 103 |
| 4.1  | Normal Plot of Residuals against Externally Studentized Residuals of Cubic model on GPU Core Temperature                       | 112 |
| 4.2  | Graph of Predicted against Actual of cubic model on GPU Core Temperature   | 113 |
| 4.3  | Model Graph of cubic model on GPU Core Temperature   | 114 |
| 4.4  | Normal Plot of Residuals against Residuals of quartic model on GPU Core Temperature  | 116 |
| 4.5  | Graph of Predicted against Actual of quartic model on GPU Core Temperature   | 117 |
| 4.6  | Model Graph of Quartic model on GPU Core Temperature   | 118 |
| 4.7  | Normal Plot of Residuals against Externally Studentized Residuals of cubic model on GPU Memory Temperature                     | 121 |
| 4.8  | Graph of Predicted against Actual of cubic model on GPU Memory Temperature   | 122 |
| 4.9  | Model Graph of Cubic model on GPU Memory Temperature   | 123 |
| 4.10 | Normal Plot of Residuals against Residuals of quartic model on GPU Memory Temperature  | 125 |
| 4.11 | Graph of Predicted against Actual of quartic model on GPU Memory Temperature   | 126 |
| 4.12 | Model Graph of quartic model on GPU Memory Temperature   | 127 |
| 4.13 | Normal Plot of Residuals against Externally Studentized Residuals of Cubic model of GPU Core Temperature on nickel thermal pad | 132 |
| 4.14 | Graph of Predicted against Actual of cubic model of GPU Core Temperature on nickel thermal pad.                                | 133 |

|      |  |     |
|------|--|-----|
| 4.15 | Model Graph of cubic model of GPU Core Temperature on nickel thermal pad   | 134 |
| 4.16 | Scatter plot of residuals versus residuals of a quartic model representing the relationship between GPU core temperature and nickel thermal pad. | 136 |
| 4.17 | Comparison of the quartic model's predicted and actual values for the temperature of GPU memory on a nickel thermal pad                          | 137 |
| 4.18 | Model Graph of quartic model of GPU Core Temperature on nickel thermal pad   | 138 |
| 4.19 | The thermal nickel pad for normal plot of residuals versus externally standardised residuals of a cubic model of GPU memory temperature          | 141 |
| 4.20 | Graph comparing the predicted values to the actual values of a cubic model representing the GPU memory temperature on a nickel thermal pad.      | 142 |
| 4.21 | Graphical representation of a cubic model of the temperature of GPU memory on a nickel thermal pad   | 143 |
| 4.22 | Normal Plot of Residuals against Externally Studentized Residuals of Cubic model of GPU Core Temperature on copper thermal pad                   | 148 |
| 4.23 | Graph of Predicted against Actual of cubic model of GPU Core Temperature on copper thermal pad.  | 149 |
| 4.24 | Graph depicting the cubic model of GPU core temperature on a copper thermal pad.   | 150 |
| 4.25 | The thermal copper pad for normal plot of residuals versus externally standardised residuals of a cubic model of GPU memory temperature          | 153 |
| 4.26 | Graph comparing the predicted values to the actual values of a cubic model representing the GPU memory temperature on a copper thermal pad.      | 154 |
| 4.27 | Graphical representation of a cubic model of the temperature of GPU memory on a copper thermal pad   | 155 |
| 4.28 | Graph of GPU Core Temperature against variations of thermal pad.   | 156 |
| 4.29 | Graph of GPU Memory Temperature against variations of thermal pad.   | 156 |
| 4.30 | Temperature validation on 1430 RPM on stock thermal pad  | 160 |
| 4.31 | Temperature validation on 2979 RPM on nickel thermal pad   | 161 |
| 4.32 | Temperature validation on 1365 RPM on copper thermal pad   | 162 |

## LIST OF ABBEREVATIONS

|        |  |
|--------|--|
| GPU    | Graphic Processing Unit                                    |
| CPU    | Central Processing Unit                                    |
| TEC    | Thermal Electric Cooler                                    |
| OpenGL | Open Graphic Library                                       |
| API    | Application Programming Interface                          |
| CFD    | Computational Fluid Dynamics                               |
| STAR   | Simulation of Turbulence Flow in Arbitrary region          |
| CCM+   | Computational Continuum Mechanics                          |
| GFRP   | Glass Fibre Reinforced Plastic                             |
| BPF    | Blade Passing Frequency                                    |
| OASPL  | Overall Sound Pressure Levels                              |
| BVI    | Blade Vortex Interaction                                   |
| FFD    | Free Form Deformation                                      |
| LTEEC  | Closed-loop liquid-based thermoelectric electronic cooling |
| COP    | Coefficient of Performance                                 |
| LPM    | Litre per Minute   |
| f-Gnp  | Functionalized graphene nanoplatelets                      |
| CHTC   | Convective heat transfer coefficient                       |
| TDP    | Thermal Design Power                                       |
| CUDA   | Compute Unified Device Architecture                        |

|        |  |
|--------|--|
| AMCA   | The Air Movement and Control Association International |
| ASICs  | Application-Specific Integrated Circuits               |
| BTC    | Bitcoin  |
| ETH    | Ethereum   |
| LTC    | Litecoin   |
| ADA    | Cardano  |
| DOGE   | Dogecoin   |
| PoW    | Proof of Work  |
| RSM    | Response Surface Methodology                           |
| ANOVA  | Analysis of Variance                                   |
| DOE    | Design of Experiments                                  |
| VDD    | Core Voltage   |
| CCLOCK | Core Clock   |
| MCLOCK | Memory Clock   |



اونيورسيتي تيكنيكل مليسيا ملاك  
 UNIVERSITI TEKNIKAL MALAYSIA MELAKA

## LIST OF SYMBOLS

|               |   |                                      |
|---------------|---|--------------------------------------|
| $\rho$        | = | Density                              |
| $\mu$         | = | Dynamic Viscosity                    |
| $Q$           | = | Heat Capacity                        |
| $C_p$         | = | Specific Heat                        |
| $\Delta T$    | = | Temperature Difference               |
| $Q_{cond}$    | = | Rate of Heat Conduction              |
| $k$           | = | Thermal Conductivity                 |
| $h$           | = | Convection Heat Transfer Coefficient |
| $T_s$         | = | Surface Temperature                  |
| $T_\infty$    | = | Ambient Temperature                  |
| $\varepsilon$ | = | Emissivity                           |
| $\sigma$      | = | Stefan-Boltzmann constant            |
| $P$           | = | Heat Flux                            |

## LIST OF APPENDICES

APPENDIX A

PSM GANTT CHART

177



# CHAPTER 1

## INTRODUCTION

### 1.1 Background Study

The density of transistors in CPUs and GPUs is increasing at an exponential rate due to the rapid advancement of Information Technology (IT) (Abu Raihan Mohammad Siddique, et al., 2019). Traditional computers lack the processing speed and efficiency needed to run the latest software, which has emerged in response to the explosion of available data. For example, video editing software like Adobe Premiere Pro, Solidworks, Catia, AutoCAD, and others need not only powerful computers, but also powerful graphics cards, in order to function properly. In this case, it's not feasible to use a general-purpose computer that just relies on the Central Processing Unit (CPU) to run high-resolution video rendering and real-time 3-D picture decoding. An alternative processing architecture, GPU has found widespread adoption for data-intensive operations in this area (Matthews, 2018).

A GPU, or graphics processing unit, is a dedicated chip or electronic circuit for the purpose of producing display-ready visuals on a computer or other electronic device (Jake Frankenfield, 2021). The GPU is a non-graphics compute processor that differs in architecture from conventional sequential processors in a number of ways (Wong et al., 2010). The graphics processing unit (GPU) was first released to the public in 1999, and its primary function is to ensure the high-quality visuals present in today's popular videos and

games. The multi-threading capacity of GPUs makes them ideal for processing huge datasets quickly and efficiently (Crespo et al., 2011). Because of its ability to do several calculations in parallel, a graphics processing unit (GPU) can improve computer efficiency by handling more computationally complex tasks, such as rendering, that would otherwise fall to the central processing unit (CPU). Unlike typical multi-core CPUs, which cannot offer this parallel level, GPUs can accomplish several hundred jobs concurrently, making them what is known as a multi-core processor (Fritzen et al., 2014). Nvidia, Advanced Micro Devices (AMD), Intel, and ARM are among the few GPU manufacturers that have been considered market leaders.

The elevated temperature of the system as a result of rising component density in electronic components is having an adverse effect on the device's performance and lifespan (O. Khonsue, A.I. Uddin et al., 2012). As a consequence of this for the past few decades, people have been researching and developing on superior methods of cooling. (X.P. Yang et al., 2022) split typical thermal management techniques into three distinct groups: active heat dissipation, passive heat dissipation, and thermoelectric cooling. In passive cooling, heat transfer takes place by means of the mediums of convection, conduction, and radiation. Active cooling, on the other hand, makes use of energy meant for cooling purposes only. These two types of cooling methods have current applications in heat sinks and heat spreaders. Electronic devices include two types of components: active and passive, and both of these contribute to the overall temperature of the system. The GPU is just one of many hard-working components that produce tremendous heat. This necessitates the use of an active thermal cooling system to keep the internal temperature down (A. Siricharoenpanich et al., 2021).

Active cooling methods include the use of fans and water, whereas passive cooling methods include the use of heat sinks. The GPU cooling system makes use of these three

main systems for cooling. For a fan-cooling system, the graphics processing unit is cooled using an air-based system that includes a fan, a finned heat sink, and heat pipes. The GPU's working temperature can be lowered with the help of a fan, which will generate forced air convection and aid in the heat sink's dissipation of the GPU's heat. As opposed to fan-cooling, which relies on air to vent GPU heat, water-cooling employs liquid. Compared to air, liquids are superior heat transfer media because their heat capacities and thermal conductivities are much larger (F. Meng et al., 2019). Compared to air cooling, commercially available liquid cooling systems are said to be more effective. There are four main parts to a liquid cooling system: the heat sink, the pump, the radiator, and the fan. These parts are often prefilled with liquid and connected via piping systems (Abu Raihan Mohammad Siddique et al., 2019). An electronic component or chip's heat can be dissipated by a heat sink. According to research (Jeehoon Choi et al., 2012), a heat sink's effectiveness is mostly determined by the forced air convection created by its fans. (Amir Faghri et al., 2020) found that among the many heat sink types, two-phase forced-convection cooling of high-heat-flux/high-power electronic devices were one of the most effective methods of thermal management.

## 1.2 Problem Statement

The development of cutting-edge energy technology has been an increasingly popular topic in recent years. As the information technology industry continues to advance at a breakneck pace, the potential of individual computer cabinets to generate heat is also growing. However, if the temperature in the computer system gets too high, the chip within could be damaged, leading to errors (He W et al., 2022). Thus, internal heat is the primary cause of performance issues within computers. When computers are left on for too long in hot environments, they can lose functionality and fail sooner than expected. Solid-state devices start to degrade and fry at temperatures over 120 degrees Celsius (Paul Chamber, Element Digital, 2016). As the need for more powerful computing systems increases exponentially, cooling electronic chips has been identified as one of the greatest difficulties (Vargas-Vazquez et al., 2018).

A powerful cooling system is required for heat dissipation. This is why it's important to research and develop new, more effective cooling techniques. The cooling system of a computer can be either active cooled i.e., air-cooled, water-cooled, or passively cooled by a heat sink, all of which are available on the present market. To improve the efficiency of a regular air-cooling system, however, one must currently resort to increase the fan's size, the number of fans, the radiator's size, the pump's size, and the power input to the fans and pump. An increase in the size of any component in a cooling system may necessitate an increase in the amount of physical space required, which in turn may increase the cost of the cooling system, reduce its efficiency, and make it less convenient for the user (Abu Raihan Mohammad Siddique et al., 2019). Therefore, to improve cooling system performance, new developments in technology and system optimisation are needed. These include, but are not limited to, optimising water blocks (A.B. Etemoglu, 2007), employing nanofluids (I. Sauciuc et al., 2005), employing two-phase cooling techniques (J.V. Es et al., 2013), enhancing

vapour chambers (S.S. Khaleduzzaman et al., 2014), and use of thermoelectric cooler (TEC) (A.H. Shourideha et al., 2018) to achieve higher cooling capacity and better thermal management of GPU cooling system.

In order to fill in some knowledge gaps about controlling GPU temperature with cooling technologies, the goal of this study is to do new research on GPU thermal control. The primary purpose of this research is to investigate the impact of fan speed on GPU temperature under identical GPU load situations and to figure out the ideal fan speed that is able to attain minimal GPU core and memory temperature through the application of Design Expert software. The GPU load addressed in this context corresponds to the use of Nicehash, notably with respect to the Dagger Hashimoto mining algorithm. This load is influenced by elements such as the GPU power limit, core clock, and memory clock speed. The second purpose of this study is to explore the impact of various materials for radiator heatsinks, notably copper and nickel, on the thermal dissipation performance of GPU memory. The literature research has shown that the memory component of the GPU is the principal cause of heat generation. Therefore, this research attempts to further explore the radiator heatsink material properties of GPU memory and their influence on thermal dissipation.

### **1.3 Objectives**

The objective of this study are as follows:

1. To investigate the effects of fan speed on GPU temperature under identical GPU load conditions.
2. To obtain and validate the optimal fan speed through numerical solution of RSM on GPU core and memory temperature.

3. To investigate the impact of various material of thermal pad on GPU memory thermal dissipation performance by utilizing RSM analysis.

#### 1.4 Scope of Study

The bounds of this project are:

1. The research scope is limited to GPU active cooling system which is fan-cooled.
2. The GPU used for this study is limited to ASUS Tuf Gaming 3060.
3. The investigation will focus solely on the thermal dissipation performance of GPU core and memory temperature.
4. The fan speed of the ASUS TUF Gaming 3060 is set at 550 rpm as the lowest, while 3000 rpm is the maximum fan speed for the analysis.
5. The fan speed obtained through RSM numerical optimization will be verified and validated to ensure the suitability of the mathematical model chosen.
6. The deviation between the optimised memory temperature and the actual temperature would be determined.
7. The materials used for testing heatsink radiator thermal performance will be limited to copper and nickel.
8. The thermal performance comparison between original, nickel and copper thermal pad would be compared based on the memory temperature achieved at the same fan speed.

## CHAPTER 2

### LITERATURE REVIEW

#### 2.0 Overview

This chapter will provide a basic overview of the GPU and its various components. The primary emphasis lies on the heat-generating components and cooling infrastructure of the GPU. The literature review will encompass three primary classifications of GPU cooling systems, namely air-cooled, liquid-cooled, and heat sink. The three fundamental concepts, namely material, design, and size, will be further categorised into three separate categories. By integrating these three approaches, it enables a more effective approach towards achieving proficiency in GPU heat control. To acquire knowledge regarding the execution of an optimal fan speed experiment and the selection of suitable materials for a radiator heat sink in a GPU, it is imperative to consult relevant literature. This literature should encompass topics such as GPU load generation, heat transfer mode, mining activities, mining platforms, mining algorithms, and the utilisation of Design Expert software. The Design Expert software serves as a tool for conducting optimisation through analytical and graphical approaches.

## 2.1 Introduction of Graphic Processing Unit (GPU)

GPUs are designed for data-parallel processing and 3D graphics rendering. Rendering 3D graphics shows intensive parallel processing. It calculates geometric (vertex) and raster (pixel). GPUs are continually improving towards highly parallel, configurable processors with plenty of GFLOPS and fast throughput to meet market needs and the rapidly growing gaming sector. GPUs' transition from fixed pipelining to programmable parallel processors is well documented. Vector architectures' simultaneous instruction management and ILP-accelerated graphical processing. SWAYAM (2011) stated that GPUs use parallel threads to hide the high cost of global memory accesses, making them data-parallel and throughput-oriented CPUs. According to Fujihiko Ino (2013), CPUs focus on latency and can multitask. GPUs require thousands of threads, making them many-core processors. CPUs may use several threads at once. GPUs work well with CPUs in scenarios with lots of predictable data and calculations. The CPU performs sequential programming parts, while the GPU handles computationally intensive parts to boost throughput.

Early GPUs used open GL and the Microsoft DX API to render 3D graphics with fixed-function vertex pixel shaders. The quest for more complex visual effects from fixed-function graphics hardware led the trend towards programmable CPUs. After that SWAYAM (2011) claimed that Nvidia launched the first programmable vertex processor with vertex shaders in 2001. Later, DX9 and OpenGL GPUs were available. Nvidia released dynamic parallelism-based Kepler in 2012. Shilan Ahmed Mohammed et al (2021) stated that Nvidia bought a pascal with advanced AI, deep learning, and other computing capabilities. GPUs have many uses. The academic community was an early user, but the general research community has since caught on because of its massive speedups in several sectors. GPUs

are used in banking, oil and gas exploration, computational physics, chemistry, life sciences, and signal processing.



**Figure 2.1** Example of GPU

## 2.2 Thermal Management of GPU under Computational Fluid Dynamics Simulation

The use of graphics processing units (GPUs) in high-performance computing has turned into the major heat source. When a computer gets too hot, the graphics processing unit (GPU) stops working as efficiently, which slows down the machine's performance. However, the distribution of temperature at the heat sink and the direction and rate of heat transmission inside a computer case remain mysteries. To find a solution to the graphics card overheating problem, a team of researchers led by Zambri Harun et al. (2019) used a computational fluid dynamics (CFD) simulation to investigate and observe the transfer of heat flow within a computer case and heat sink.

Zambri Harun et al. (2019) modelled a computer casing and a simplified graphic card to simulate a computer's functionality. Size, shape, and material of graphic card and heat sink are represented similarly to market availability. The simulation is carried out using a programme called STAR-CCM+. Case dimensions were specified as  $0.5 \text{ m} \times 0.5 \text{ m} \times 0.2 \text{ m}$ , with the GPU taking up  $30 \text{ cm} \times 10 \text{ cm} \times 2 \text{ cm}$  of space. Then, three heat sink models were built to examine how changing the shape, size, or number of fins on a heat sink might affect

its ability to dissipate heat. Below is a diagram detailing the shape and dimensions of a heat sink:

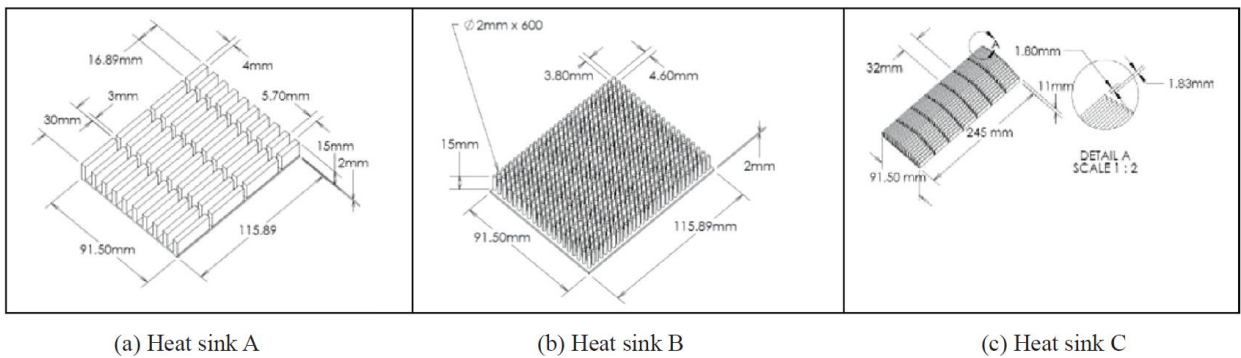


**Figure 2.2** Three heat sink case studies (Zambri Harun et al., 2019)

The simulation's boundary conditions were designed so that the air input velocity and pressure outlet velocity were each  $1 \text{ ms}^{-1}$ . The air was thought to be moving steadily and incompressible the whole time, with a constant density of  $1.225 \text{ kg/m}^3$ . Both the air temperature and air pressure were considered to be standard conditions, with a value of  $25^\circ\text{C}$  and  $101325 \text{ Pa}$ , respectively. Below is a diagram depicting the simulation's boundary conditions.

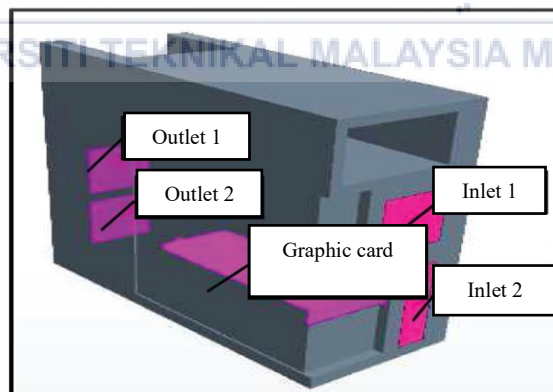


**Figure 2.3** Boundary conditions (Zambri Harun et al., 2019)

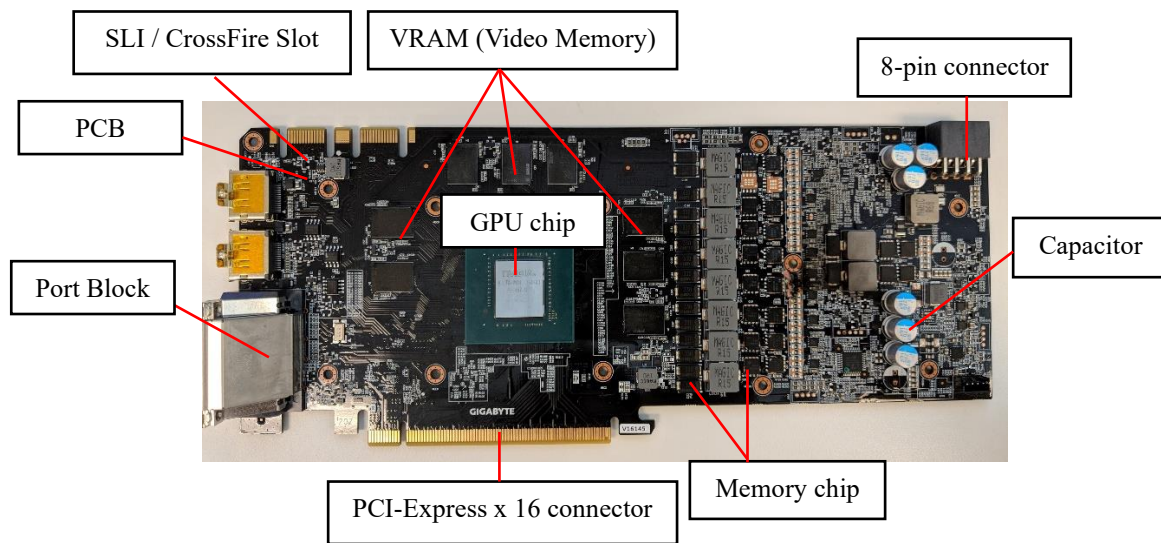


**Figure 2.4** Components of GPU

The material properties of the components are according to the standard mechanical properties of each material. The materials for heat sink and graphic card are shown in Table 2.1.

**Table 2.1** Material for each component

| Component                   | Material      |
|-----------------------------|---------------|
| Heat sink                   | Aluminum      |
| Capacitor                   | Alumina       |
| Memory chip                 | Silicon       |
| GPU chip                    | Aluminum      |
| Printed circuit board (PCB) | FR-4 + copper |
| Connector port block        | Aluminum      |
| Back plate                  | Aluminum      |

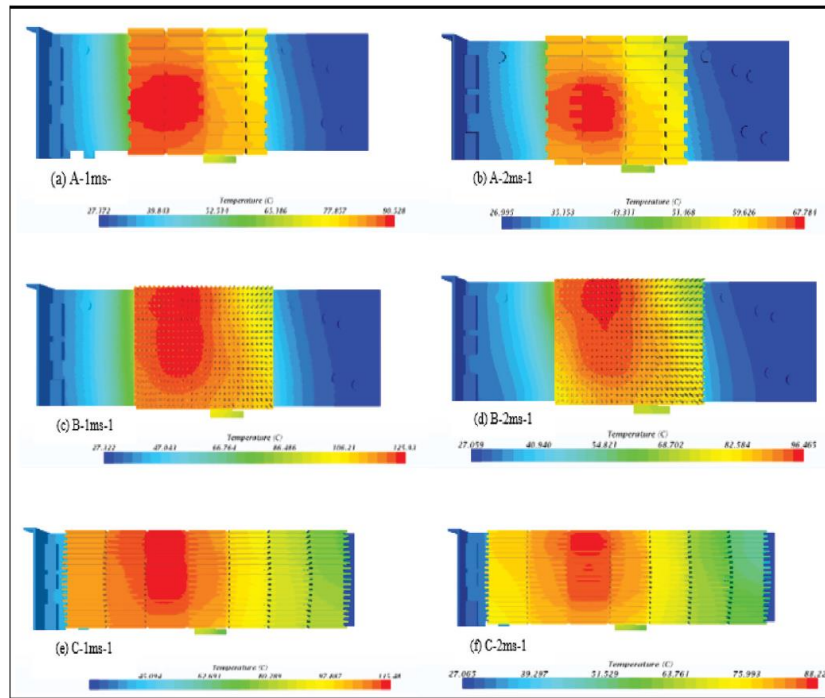


**Figure 2.5** Temperature contours on heat sink (Zambri Harun et al., 2019)

The simulation showed that the heat sink's temperature distribution is highest in its centre and drops away from it. Figure 2.5 shows that the GPU chip and VRAM are the hotspots. The GPU chip-heat sink interface conducts. The GPU chip and other electronics conduct heat to the heat sink. Hot air from the heat sink is transported away by incoming convective air, causing convection. This phenomenon showed why electronic parts should be kept away from, or partially covered by, heat sources to avoid overheating and failure. Heat sink maximum temperature was likewise shown to be inversely proportional to inlet wind speed. Increased air velocity lowers heat sink maximum temperature. The fast breeze speeds up heat dissipation from the heat sink. Bejan (2013) claimed that accelerating convection lowers peak temperature.

Also, out of the three heat sinks tested, the largest surface area and greatest volume belonged to heat sink A, making it the most efficient. Leach (2005) notes that the rate of heat loss increases as volume area increases. Below is a graph depicting the maximum temperature of a heat sink at various velocities:

**Table 2.2** Maximum temperature of heat sink for different velocity (Zambri Harun et al., 2019)

| Heat sink | Velocity inlet ( $\text{ms}^{-1}$ ) | Maximum temperature ( $^{\circ}\text{C}$ ) | Volume area ( $\text{mm}^3$ ) |
|-----------|-------------------------------------|--|-------------------------------|
| A         | 1                                   | 90.52                                      | 6.31                          |
|           | 2                                   | 67.78                                      | 6.31                          |
| B         | 1                                   | 125.94                                     | 4.03                          |
|           | 2                                   | 96.467                                     | 4.03                          |
| C         | 1                                   | 115.48                                     | 4.3                           |
|           | 2                                   | 88.225                                     | 4.3                           |

According to Table 2.2, the maximum temperature of a heat sink decreases as its volume area increases, since a larger volume area results in a higher rate of heat loss via convection. The number of fins on the heat sink is proportional to the volume, and this is how heat is transferred away from the graphics card during the conduction process. Shah (2003) claimed that greater surface area means more fins, which means faster heat transmission and a cooler maximum temperature for the GPU chip.

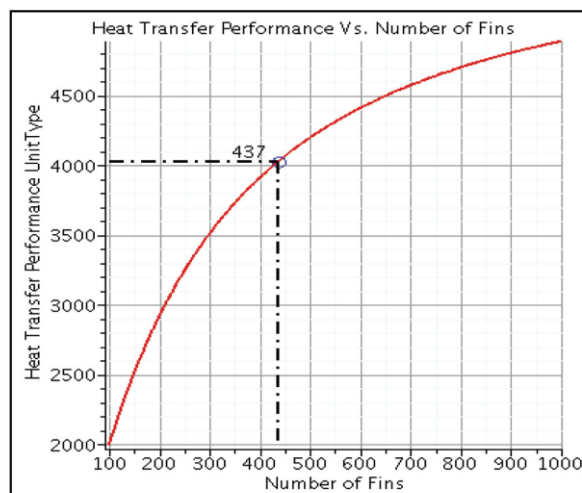


**Figure 2.6** Heat transfer performance against number of fins (Maplesoft et al., 2008)

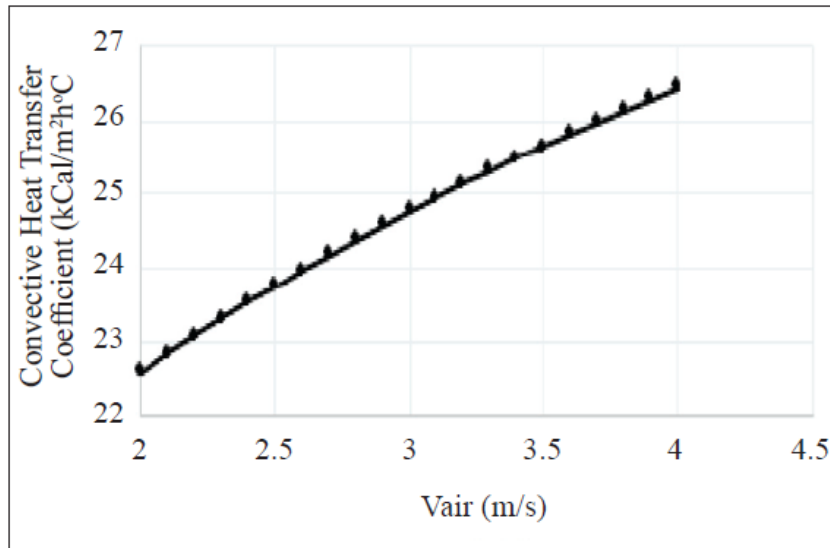


**Figure 2.7** Graph of relationship between convective heat transfer coefficients against air velocity. (Khabari et al., 2014)

The rate of heat transmission via convection is greatly dependent on the air velocity for convection cooling. There is a direct correlation between the speed of the air and the heat convection coefficient. According to Khabari et al. (2014), more heat is transferred at a given rate when the air velocity is greater. The idea presented by Khabari et al. (2014) is applicable to graphic cooling systems as well; the faster the velocity of the wind entering the system, the faster the heat will be transferred from the heat sink.

Zambri Harun et al. (2019) has also looked into the GPU's thermal behaviour in a transitional condition. According to Smith (1975), a system is in a transient state when the process variable is changing but the system has not yet attained steady-state conditions. It can be shown that heat started to spread to the heat sink slowly based on the comparison between the temperature distribution contour of each heat sink for speed at a different time interval ( $t = 100$  s, 200 s, 300 s, 400 s, 500 s). Here is where heat was transferred from the GPU to the heat sink.

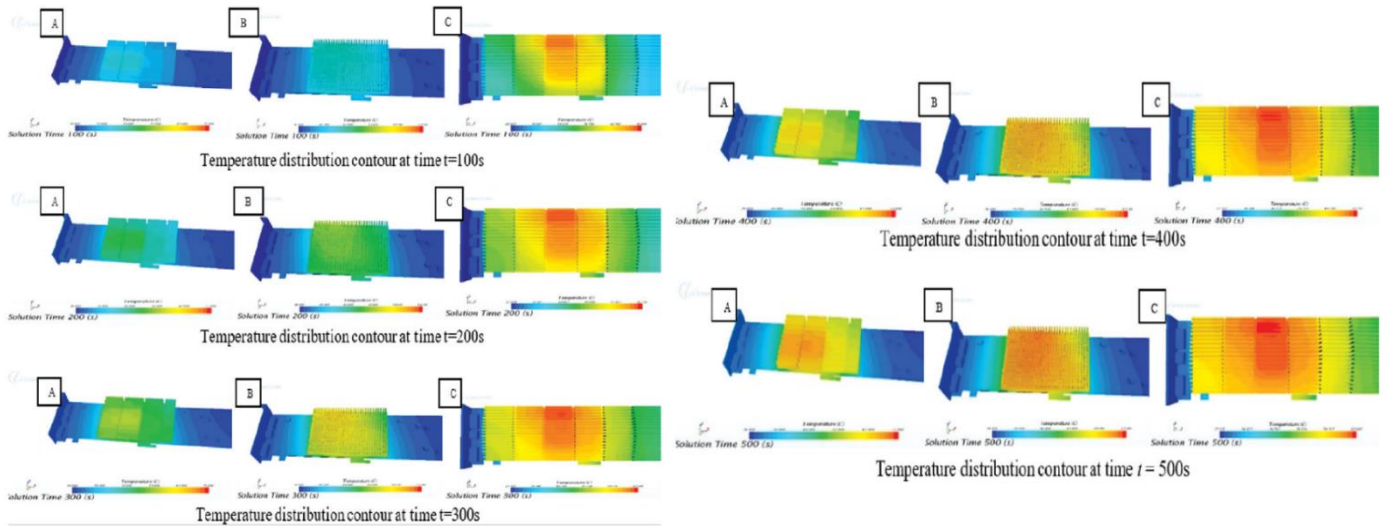


**Figure 2.8** Temperature distribution contour of each heat sink for speed  $1\text{ms}^{-1}$  at different time interval. (Zambri Harun et al., 2019)

Figure 2.8 illustrates that heat sink B has the highest rate of heat exchange, followed by heat sink C and heat sink A. As can be seen in Table 2.2, heat sink B has the smallest volume area. Thermodynamic principles can be used to heat sink B, as the heat transfer rate per unit area is proportional to the square of the area.

**Table 2.3** Initial & final temperatures of each heat sink. (Zambri Harun et al., 2019)

| Heat sink | Initial Temperature (°C) | Final Temperature (°C) | Change in Temperature (°C) |
|-----------|--------------------------|------------------------|----------------------------|
| A         | 26                       | 71                     | 45                         |
| B         | 26                       | 122                    | 96                         |
| C         | 26                       | 81                     | 55                         |

From the data of Table 2.3, it shows that the lower the volume area, the greater the rate of heat transfer, and the higher the temperature will be in the end.

Zambri Harun et al. (2019) also investigated how temperatures changed over time. The findings pointed to the vicinity of the graphics card as the source of the majority of the heat generated by it. Then the convection processes gradually brought the heat up to the top of the CPU case. Due to the decreased density of hot air compared to cold air, this phenomenon took place. Therefore, as the time interval increases, the hot air will continue to concentrate at the top of the CPU case.

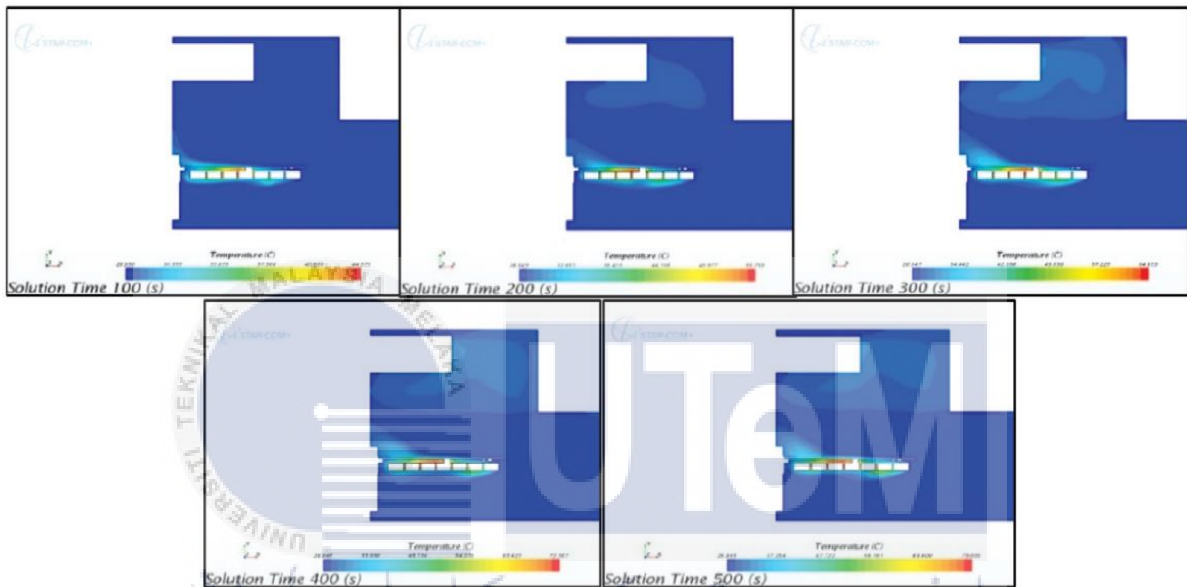


**Figure 2.9** Temperature distribution in CPU case with time interval  $t = 100$  s, 200 s, 300 s, 400 s, 500 s. (Zambri Harun et al., 2019)

Zambri Harun suggested that an increase in the height and number of heat sink fin to allow to enhance the overall surface area can be used to improve the cooling system for the CPU. Some fans also need to be moved to the top of the CPU case in order to better dissipate the heat that builds up there. The CPU's power supply, which is now placed at the top, should be moved down to the case's underside to maximise cooling.

### 2.3 GPU Cooling System

GPU heat management and behaviour were determined in the preceding section. It was found where most CPU case heat was generated and accumulated. Thus, the GPU's cooling system will be extensively explored below. GPU cooling is vital because GPU performance and longevity depend on it. C. Nadjahi et al. (2018) stated that the cooling system regulates air temperature and relative humidity to keep electronic equipment safe. GPU efficiency is temperature-dependent. Thermal throttle lowers GPU speed and compute frequency to lower temperatures when they exceed a threshold. An underpowered GPU will produce lower-quality graphics, making it less performance-efficient.

In short, compromising performance and graphics quality to keep the GPU cool is not the best option. In addition to the aforementioned methods, air-cooling, water-cooling, and a heat sink are all viable options for GPU cooling. Heatsinks are an example of passive cooling, as they cool the GPU by natural convection without using any additional energy, in contrast to active cooling methods like air-cooling and water-cooling. The material, design, and dimensions of these cooling technologies, as they pertain to GPU thermal management, will be addressed at length.

### 2.4 Fan-cooling

GPUs have gotten more durable and space-intensive as the gaming industry grows in computational power and graphics. As GPUs get more powerful, heat sinks fail to remove heat. In 1997, a fan-cooling system was created and is now commonly used to cool electronic components. Active cooling uses fan cooling with a heat sink to force convection and cool the GPU. Kheirabadi and Groulx (2016) found that forced-convection cooling applications,

including server and router cabinets and GPUs, use axial-flow cooling fans. Optimising fan-cooling systems includes material selection, design optimisation, and dimension parameter investigation for axial-flow cooling fans.



**Figure 2.10** Axial Flow Fans

#### **2.4.1 Study of Glass Fibre Reinforced Plastic on Fan Blades**

The use of non-biodegradable materials, such as glass fibre reinforced plastics, in axial flow fan blades has been proven to have an adverse effect on the environment after the blades' lifespans of use have ended. This is supported by research conducted by Venkata Sushma Chinta, et al. (2022). The tension-tension fatigue life of three hybrid composites for axial fan blades was studied by Venkata Sushma Chinta et al. (2022), who tested the 18-foot axial flow fan blade material (GFRP), the 8th layer of GFRP replaced with woven jute (G8J), and the 12th layer of GFRP replaced with woven jute (G12J). Refer to the diagram below to learn about the layering sequence of GFRP blade material:

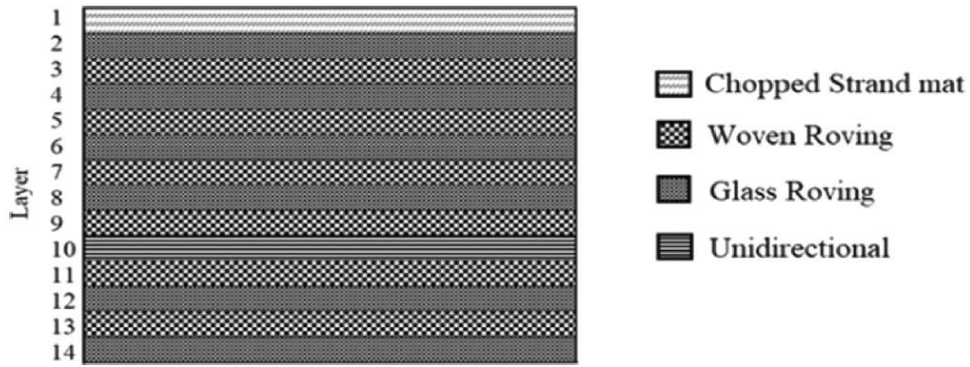


**Figure 2.11** Layer Sequence of GFRP blade material [CSM/(GR/WR)<sub>4</sub>/UD/(WR/GR)<sub>2</sub>]

**Table 2.4** Tensile Properties of composites. (Venkata Sushma Chinta et al., 2022)

| Hybrid composite | Ultimate Tensile strength (Mpa) | Axial Young's Modulus (Gpa) | Failure strain (%) |
|------------------|---------------------------------|-----------------------------|--------------------|
| GFRP             | 395±13                          | 22.8±0.60                   | 3.68±0.34          |
| G8J              | 391±5.5                         | 22.7±0.35                   | 3.47±0.24          |
| G12J             | 391±6.5                         | 22.4±0.20                   | 3.51±0.10          |

They observed that for all three materials, the endurance limit ( $10^6$  cycles) was met at a normalised peak stress ratio of 0.4. Thus, at any given normalised peak stress ratio, GFRP exhibits the longest fatigue life. Hybrid composites made of G8J and G12J have the same fatigue life regardless of the orientation of the woven jute. In addition, this study found that the fatigue life of the woven jute reinforced composite was almost 78% that of GFRP. In order to ensure biodegradability after service life, they suggested using woven jute for partial reinforcement in fan blades at low normalised peak loads. The production of the woven jute blade also costs less than the production of a standard blade.

To make GFRP composites more biodegradable after their useful lives have ended, it is necessary to investigate the extent to which natural fibres can be used as reinforcement without significantly degrading the composites' mechanical qualities. Therefore, Venkata

Sushma Chinta et al. (2023) tested material C<sub>1</sub> with a GFRP axial fan blade measuring 18 feet in length to investigate the shear properties of partial woven jute reinforcement. C<sub>2</sub>–C<sub>6</sub> were produced by replacing one layer of C<sub>1</sub> with woven jute and shifting the jute's position within C<sub>1</sub>. Shear strength tests were conducted on all of the materials in accordance with IS 1998-62.

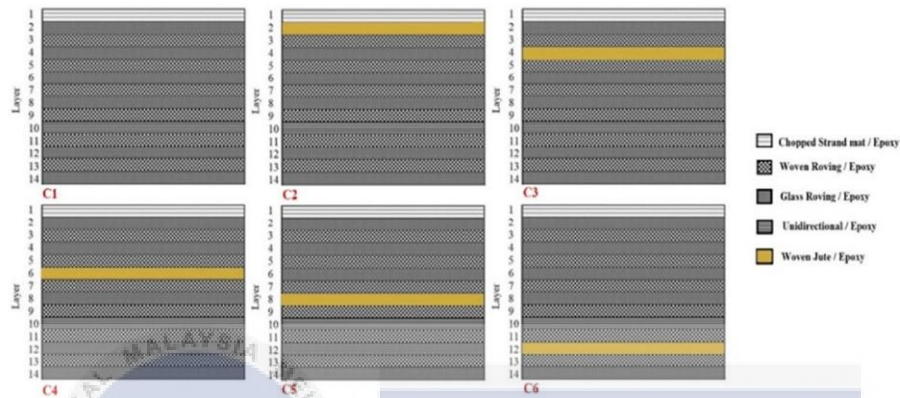


**Figure 2.12** Layout Sequence of blade material with and without woven jute reinforcements [CSM/(GR/WR)<sub>4</sub>/UD/(WR/GR)<sub>2</sub>] (Sushma Chinta et al., 2023)

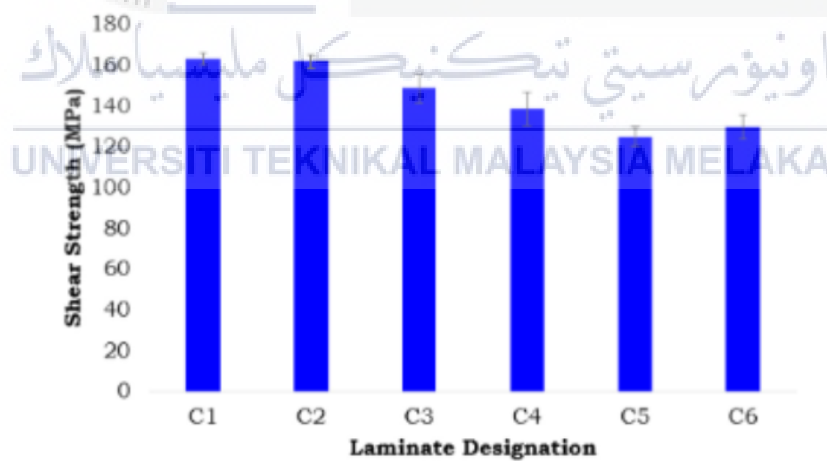


**Figure 2.13** Shear Strength from experiment (Sushma Chinta et al., 2023)

The results showed that when jute was positioned in the second position (C<sub>2</sub>), the woven jute fibre composite exhibited superior shear characteristics. C<sub>2</sub> enhances biodegradability and maintains the shear strength qualities of the GFRP blade material.

Therefore, it was suggested that woven jute be used in place of GFRP in the second layer (C<sub>2</sub>) because its shear properties are comparable to those of the first (C<sub>1</sub>).

The tensile characteristics of GFRP with woven jute were tested in accordance with ASTM D-638 by Venkata Sushma Chinta et al. (2022), who replaced GFRP layer blades with woven jute at different layers. The tensile behaviour was then evaluated by substituting woven jute for GFRP in a number of configurations (2 layers, 3 layers, 4 layers, and 5 layers). Below is a table illustrating the sequence of woven jute in GFRP blade material.

**Table 2.5** Laminate designation for various cases (Sushma Chinta et al, 2022)

|   | Cases | Position of woven Jute in GFRP |  | Cases | Position of woven Jute in GFRP |
|---|-------|--------------------------------|--|-------|--------------------------------|
| GFRP fan blade material   | C1    | No jute                        | Three layers of GR in GFRP replaced with woven jute (Glass to Jute weight ratio = 85:15) | C17   | 2,4,6                          |
| One layer of GR in GFRP replaced with woven jute (Glass to Jute weight ratio = 95:5)    | C2    | 2                              |  | C18   | 2,4,8                          |
|   | C3    | 4                              |  | C19   | 2,4,12                         |
|   | C4    | 6                              |  | C20   | 2,6,8                          |
|   | C5    | 8                              |  | C21   | 2,6,12                         |
|   | C6    | 12                             |  | C22   | 2,8,12                         |
| Two layers of GR in GFRP replaced with woven jute (Glass to Jute weight ratio = 90:10)  | C7    | 2,4                            |  | C23   | 4,6,8                          |
|   | C8    | 2,6                            |  | C24   | 4,6,12                         |
|   | C9    | 2,8                            |  | C25   | 4,8,12                         |
|   | C10   | 2,12                           |  | C26   | 6,8,12                         |
|   | C11   | 4,6                            |  | C27   | 2,4,6,8                        |
|   | C12   | 4,8                            |  | C28   | 2,4,6,12                       |
| Four layers of GR in GFRP replaced with woven jute (Glass to Jute weight ratio = 80:20) | C13   | 4,12                           |  | C29   | 2,4,8,12                       |
|   | C14   | 6,8                            |  | C30   | 2,6,8,12                       |
|   | C15   | 6,12                           |  | C31   | 4,6,8,12                       |
|   | C16   | 8,12                           |  | C32   | 2,4,6,8,12                     |
|   |       |                                | Five layers of GR in GFRP replaced with woven jute (Glass to Jute weight ratio = 75:25)  |       |                                |

ANSYS R19.2 will be used to compare the tensile test results obtained from experimental results in order to estimate the tensile stress created in each material. The table below displays the experimental and ANSYS R19.2 tensile test results:

**Table 2.6** Tensile stress obtained from tension test vs ANSYS R19.2 results (Sushma Chinta et al, 2022)

| Specimen Designation | Average load (N) | Axial Young's modulus (GPa) | Ultimate tensile strength from tension test (MPa) | Tensile stress from ANSYS R19.2 (MPa) | % Deviation |
|----------------------|------------------|-----------------------------|---|---------------------------------------|-------------|
| C1                   | 33,728           | 22.8 0 ± 0.61               | 395 ±13   | 394.06                                | 0.11        |
| C2                   | 31,358           | 21.26 ±0.25                 | 366 ±13   | 362.55                                | 1.17        |
| C3                   | 32,242           | 22.3 0 ± 0.57               | 377 ±11   | 376.31                                | 0.20        |
| C4                   | 31,035           | 22.23 ± 0.21                | 367 ±22   | 360.66                                | 1.73        |
| C5                   | 32,262           | 22.46 ± 0.40                | 391 ±6.5  | 383.67                                | 1.89        |
| C6                   | 32,830           | 22.2 0 ± 0.20               | 391 ±6.5  | 385.69                                | 1.31        |

According to the table above, the conventional fan blade (C1) has the highest axial Young's modulus of all examined materials. The C5 specimen has a 22460 MPa axial Young's modulus, 98.5% higher than the C1. C2 has the lowest axial Young's modulus,

21260 MPa. By moving woven jute, GFRP blade material C5 has 5.3% greater axial Young's modulus than C2. C5 and C6 have the highest ultimate tensile strengths at 391 MPa, or 99% of C1, while C2 has the lowest at 366 MPa. Adding jute at the eighth and twelfth locations improves stress-bearing capacity by 6.4%. Only 1.89% separates experimental and ANSYS R19.2 values. The finite element method was useful for calculating hybrid composite equivalent stress.

By shifting the number of jute layers and the location of jute layers in the GFRP material, it is possible to theoretically analyse the axial Young's modulus for 32 different cases, as shown in Table 2.5. Figure 2.14 below illustrates the axial Young's modulus determined by CLT for all 32 examples:

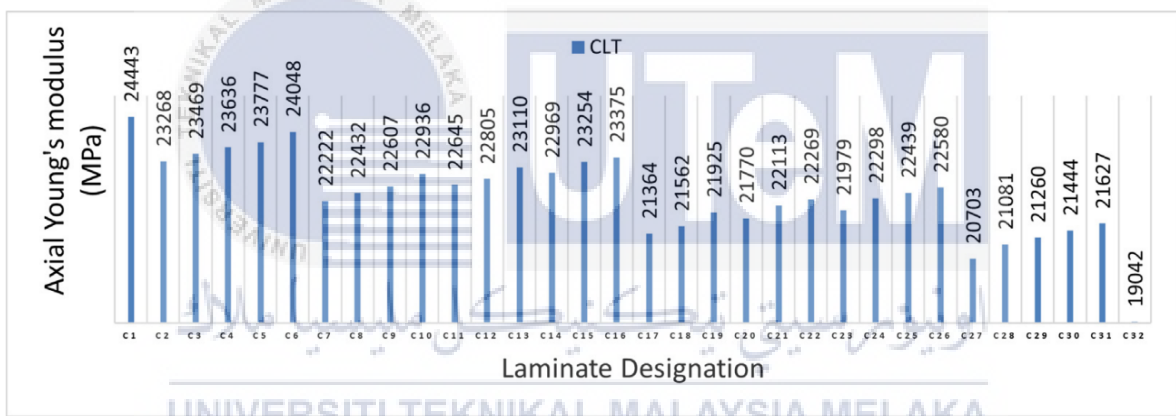


**Figure 2.14** Axial Young's modulus of 32 cases by CLT (Sushma Chinta et al, 2022)

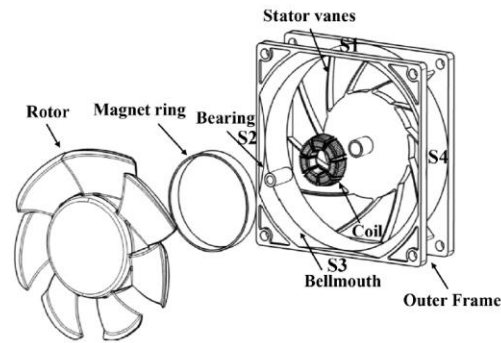
According to CLT's calculations, increasing GFRP's woven jute layers lowers Young's modulus. Shifting woven jute layers changes GFRP's axial Young's modulus. The axial Young's modulus of woven jute-reinforced cases showed that C6 (12th position) had the highest value. C6, C16, C26, and C31 have a higher axial Young's modulus than one, two, three, and four-layer jute-reinforced composites. The lowest axial Young's modulus of all 32 CLT instances is C32, which has 5 layers of woven jute. Stresses created in C5, C6, and C7 were found to be lower than their ultimate tensile strength in GFRP analysis using CLT of laminated woven jute, whereas stresses developed in the remaining materials were

found to exceed their ultimate tensile strength. Thus, Sushma Chinta et al. (2022) found that woven jute orientation greatly affects its tensile properties. The eighth or twelfth position is more important than the second, fourth, or sixth position in reinforcing woven jute for tensile properties, according to their research. Based on experimental and ANSYS R19.2 results, laminates (with a glass-to-jute ratio of 95:5), C5 (with woven jute in the 8th position of GFRP), and C6 (with woven jute in the 12th position) are the first and second recommended layup sequences because they improve biodegradability after service life without affecting stiffness.

#### **2.4.2 Study of short inlet duct cooling fan design on aerodynamic noise reduction**

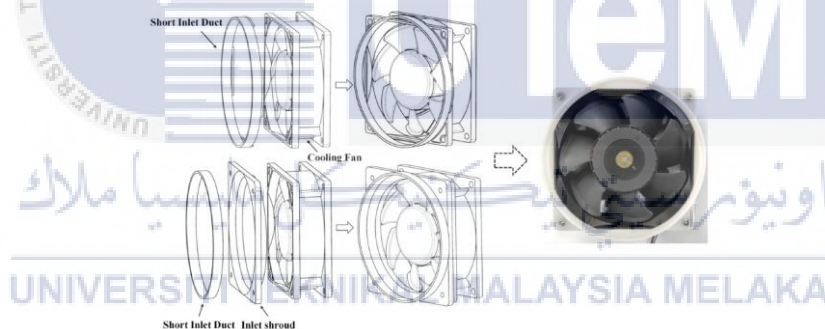
As electronic devices have shrunk in size, the need for quiet operation in confined locations has risen as a design priority for axial flow fans. This is due to the fact that numerous small axial-flow fans are often operated at high speeds in such applications to meet heat-dissipation requirements. However, doing so will produce unacceptable levels of aerodynamic noise. In order to meet a product's noise requirements, it is sometimes necessary to sacrifice equipment performance in order to lower heat generation and hence slow down the cooling fans. The performance of electrical devices is hampered by aerodynamic noise.

Figure 2.15 illustrates the basic components of a cooling fan: rotor blades, stator vanes, and an exterior frame with an asymmetrical bellmouth. Azimuthal acoustic modes, which make up tonal noise at the blade passing frequency (BPF) and its harmonics, are known to be produced by interactions between rotor blades and stator vanes (Tyler and Sofri, 1962). Pure-tone spectral tones are a defining feature of tonal noise, also known as discrete frequency noise.



**Figure 2.15** Typical cooling fan configuration (Tian et al., 2020)

Zhonghan Sun et al. (2023) found that tone noise was the predominant cause of aerodynamic noise while testing three different sized cooling fans with tip Mach numbers of 0.143, 0.156, and 0.174. Short inlet ducts were tested as a means of reducing noise in axial-flow cooling fans. Short inlet ducts, like the one depicted in Figure 2.16, can reduce overall noise by as much as 3.5, 4.8, and 7.1 decibels (dBA) on average.



**Figure 2.16** Picture of installation method for the short inlet duct (Zhonghan Sun et al., 2023)

The parameter  $L/D$  is suggested for studying how ducts of different lengths  $L$  affect fans of different diameters  $D$ .  $L/D$  ranged from 0.08 to 0.16, 0.32 to 0.48, and 0.64 to 0.8. The most noise-efficient duct was  $L/D = 0.08$ . According to Zhonghan Sun et al. (2023),  $L/D = 0.08$  was the optimal duct length ( $L$ ) for all fan types to provide the best tonal, broadband, and overall SPLs. It suggests that  $L/D = 0.08$  may be the optimal parameter option. Computational fluid dynamics (CFD) showed that the duct with  $L/D = 0.08$  did not harm

aerodynamic performance and may even improve it. According to Zhonghan Sun et al. (2023), a short inlet duct with a length-to-diameter ratio ( $L/D$ ) of 0.08 is ideal for installation on a fan with a blade-tip Mach number of less than 0.2, requiring only minor fan structural alterations.

### **2.4.3 Study of fan blade sweep angle on aerodynamic fan noise production rate.**

However, the implementation of a swept blade design remains a highly effective method for acoustically mitigating spinning fan noise. The study conducted by Park et al. (2022) aimed to examine the comprehensive impact of an automotive cooling fan on its acoustic characteristics through both numerical simulations and empirical measurements. In automotive cooling systems, the utilisation of straight, forward, and reverse-swept blades is employed for the purpose of assessing both performance and noise levels. The vehicle cooling fan under consideration has suitable geometric characteristics, including a hub diameter of 154 mm, a configuration consisting of seven rotor blades evenly distributed radially, and connecting bands measuring 390 mm in length. A fan blade with both angled and perpendicular orientations was fabricated in order to investigate the impact of sweeping orientations on fan noise. This paper presents a comparative analysis between straight fan geometry and arrangement, and sweep-angle fan geometry and layout.

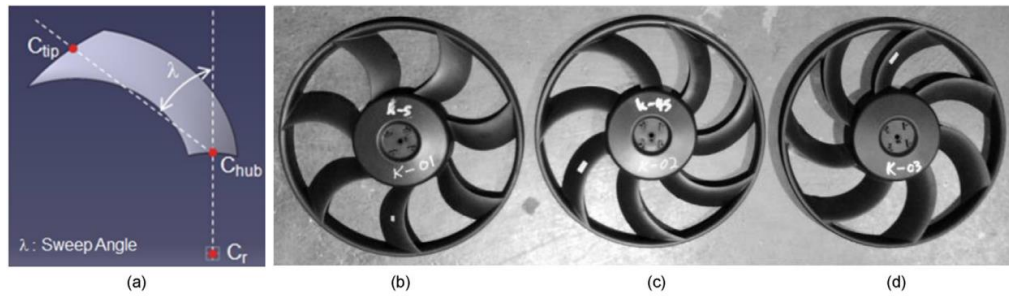


**Figure 2.17** Geometries of automotive cooling fan: (a) definition of sweep angle of fan. (b) straight fan with no sweep angle, (c) swept fan with 45 degrees forward sweep angle, and (d) swept fan with 45 degrees backward sweep angle (Minjun Park et al., 2022)

In order to determine the performance and noise level of the fan, it is necessary to conduct tests under a variety of system resistance situations. The static pressure, measured at the intake and output of the cooling fan, represents the system resistance. The pressure in front of the fan is known as the intake pressure, while the pressure measured after the fan is known as the outlet pressure. The amount of air that can flow through the fan is limited by the system's resistance. Numerical prediction findings were verified using the criteria of fan performance and noise, as reported by Minjun Park et al. (2022). The following table displays the outcomes of a comparison between experimental and numerical data for the mass flow rate of the straight, forward, and backward-swept fans:

**Table 2.7** Comparison of the experimental and numerical results for the mass flow rate (Minjun Park et al., 2022)

| Conditions         |      | Measurements     | Numerical prediction | Error (%) |
|--------------------|------|------------------|----------------------|-----------|
| Fan type           | RPM  | Mass flow (kg/s) | Mass flow (kg/s)     |           |
| Straight fan       | 1807 | 1.07             | 1.09                 | 1.87%     |
| Forward-swept fan  | 1830 | 1.01             | 0.97                 | 3.96%     |
| Backward-swept fan | 1865 | 1.09             | 1.11                 | 1.83%     |

It can be seen from the aforementioned data that the mass flow rate calculated using CFD simulation is in good agreement with the measurements, both in terms of its magnitude and fluctuations depending on the sweep directions. It is demonstrated that forward-swept fans generate a smaller mass flow rate. The noise levels of both straight and swept fans were measured in a semi-anechoic room under free-field conditions to check the accuracy of the

numerical forecasts. The following table summarises the results of studies and numerical simulations about the overall sound pressure levels (OASPL) produced by the three distinct fan designs.

**Table 2.8** Comparison of experimental and numerical results for OASPL (Minjun Park et al., 2022)

| Conditions         |      | Measurements | Numerical prediction | Error (dBA) |
|--------------------|------|--------------|----------------------|-------------|
| Fan type           | RPM  | OASPL (dBA)  | OASPL (dBA)          |             |
| Straight fan       | 1807 | 73.7         | 74.4                 | 0.7         |
| Forward-swept fan  | 1830 | 69.8         | 69.2                 | 0.6         |
| Backward-swept fan | 1865 | 73.5         | 73.1                 | 0.4         |

Then, the fans' sweeping impacts are analysed. The A-weighted sound pressure levels were measured for the straight, forward, and backward-swept fans at various rotating speeds by Minjun Park et al. (2022). Total A-weighted sound pressure levels for straight, forward, and backward-swept fans are indicated in the figure below:

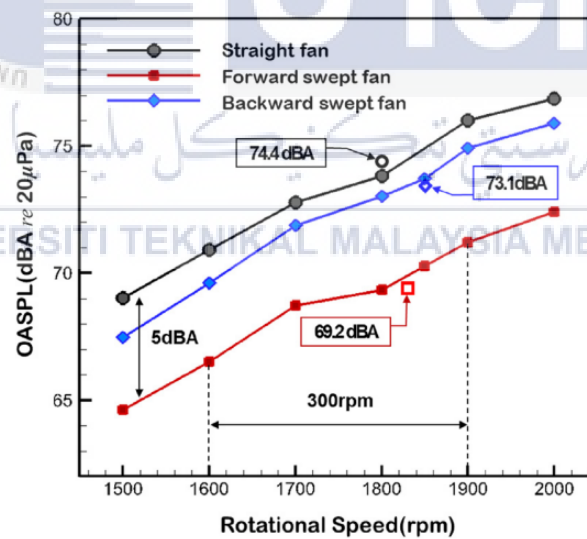


**Figure 2.18** Overall A-weighted sound pressure levels of the straight, forward- and backward-swept fans depending on rotational speeds (filled symbol: experimental results, open symbol: numerical prediction) (Minjun Park et al., 2022)

The data reveals that the straight fan's OASPL is 5 dBA higher than the forward-swept fan's at the same speed. At 1600 rpm, the straight fan's OASPL is comparable to the forward-swept fan's at 1900 rpm. The forward-swept fan has a 4 dBA lower OASPL than the

backward-swept fan. Compared to a straight, backward-swept, and forward-swept fan, the forward-swept fan makes less noise at the same rotational speed. Minjun Park et al. (2022) used velocity, vorticity, the time derivative of pressure contours, and streamlines to identify and study backward and forward-swept fan noise sources and reduction methods. Results are shown in figure:

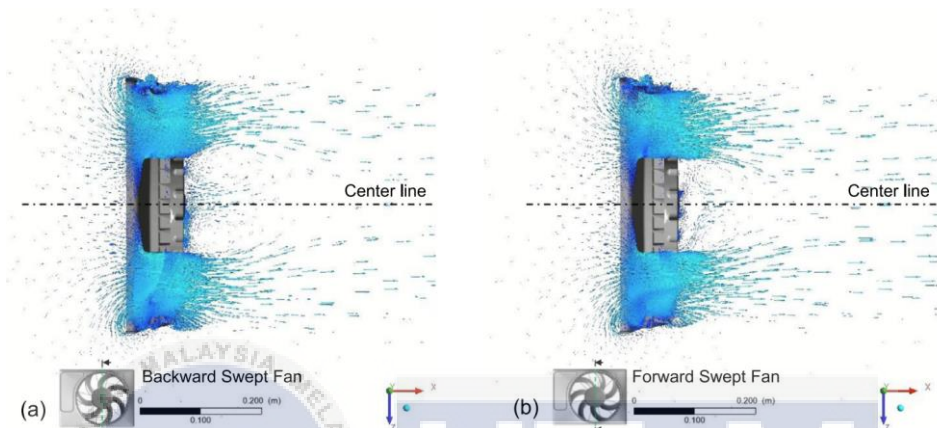


**Figure 2.19** Velocity vector in the xz plane: (a) backward and (b) forward-swept fans. (Minjun Park et al., 2022)

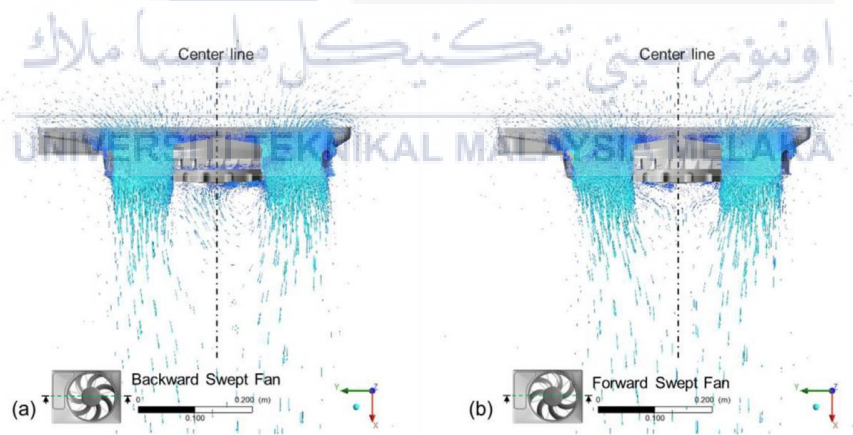


**Figure 2.20** Velocity vector in the xy plane: (a) backward and (b) forward-swept fans.

(Minjun Park et al., 2022)

The forward-swept fan flow is travelling towards the centerline and downstream from the velocity vector in the picture above. Behind a backward-swept fan's shroud, a large recirculation flow stops downstream. Minjun Park et al. (2022) found that the primary noise

sources in an automotive cooling fan system are unsteady flow interaction between rotating blades and shallow shrouds and strong blade vortex interaction (BVI) around the blade tip region. After that, the authors estimated the noise contribution mapping to understand the blade's main noise. Mapping results are shown below.

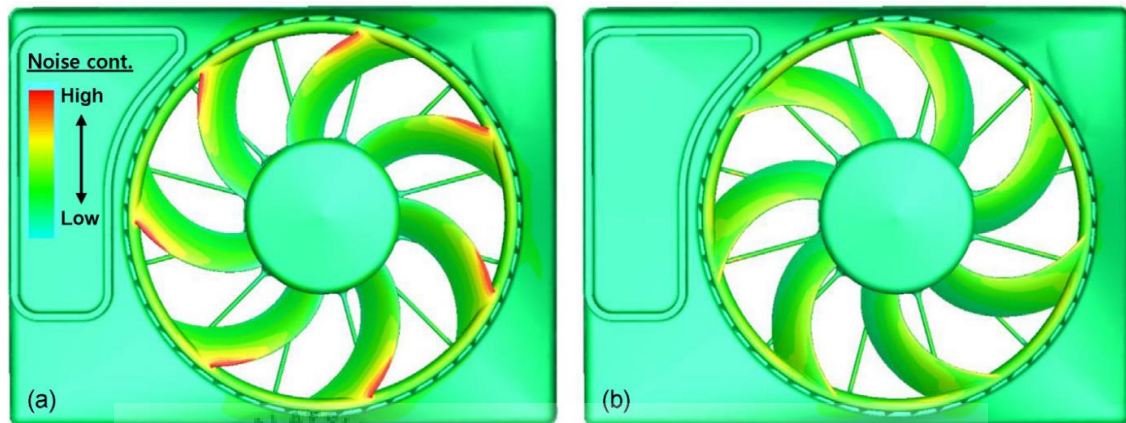


**Figure 2.21** Averaged noise contributions at the observer: (a) backward and (b) forward-swept fans. (Minjun Park et al., 2022)

Backward-swept fans have a louder leading edge than forward-swept fans. The OASPL of backward-swept fans is around 4 dB higher than that of forward-swept fans. According to additional research by Minjun Park et al. (2022), the noise source of backward-swept fans starts on the leading edge of the mid-span of blades, intensifies at the blade tip, and then moves to the trailing edge between the fan band and the tip. A forward-swept fan's noise originates near the blade's leading edge, advances slightly towards the hub, and finally travels towards the trailing edge between the fan band and the tip. The figure below shows that forward and backward-swept fans have different noise source dynamics under identical settings.

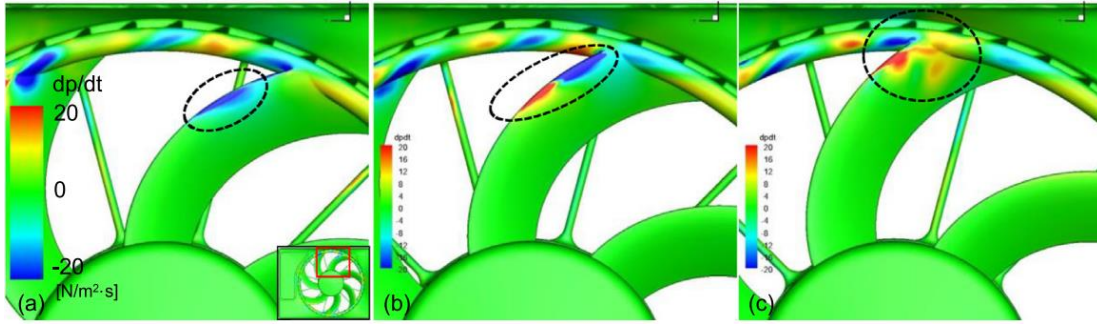


**Figure 2.22** Time derivative of the surface pressure on backward-swept fan depending on the azimuth angles: (a) 0 degree, (b) 10 degrees, and (c) 20 degrees (Minjun Park et al., 2022)

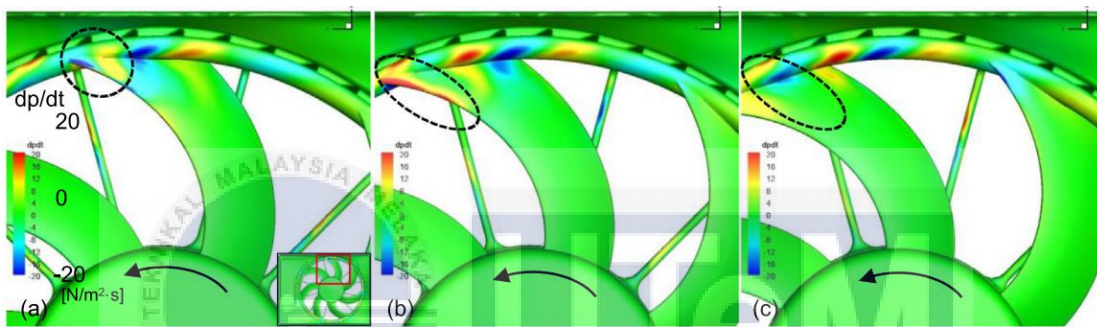


**Figure 2.23** Time derivative of the surface pressure on forward-swept fan depending on the azimuth angles: (a) 0 degree, (b) 10 degrees, and (c) 20 degrees (Minjun Park et al., 2022)

#### 2.4.4 Aerodynamic and structural multidisciplinary optimization of fan rotors towards aerodynamic performance.

The previous section covers axial-flow fan noise suppression. Noise reduction will reduce noise, but it won't improve cooling fan aerodynamics. This section discusses fan rotor aerodynamic and strength multidisciplinary optimisation design research to maximise aerodynamic performance while meeting structural strength requirements. Standard interdisciplinary optimisation approaches can be difficult to implement in engineering practice. Thus, Zhaoyun Song et al. (2023) suggested a multidisciplinary rotor optimisation design technique that accounts for blade curvature. Using the self-organising map (SOM),

the blade curvature constraint value was extracted for optimisation. Replace the time-consuming high-fidelity FEM with the blade curvature constraint value as a penalty function to substantially reduce the computational cost and runtime of the multidisciplinary optimisation. The free-form deformation (FFD) approach is used to deform the three-dimensional blade with the fewest design variables and polynomial chaos.

The main design parameter of the fan stage is shown in Table 2.9 below:

**Table 2.9** The main design parameter of the fan stage (Zhaoyun Song et al., 2023)

| <b>Design parameters</b> | <b>Value</b> |
|--------------------------|--------------|
| Hub/tip radius ratio     | 0.29         |
| Stage pressure ratio     | 1.6          |
| Rotor tip speed          | 504 (m/s)    |
| Tip Mach number          | 1.7          |
| Aspect ratio             | 2.1          |
| Rotor blade count        | 15           |
| Mass flow                | 0.94 (kg/s)  |

During the FEM structural study that was carried out by Zhaoyun Song et al. (2023), the centrifugal stress of the blade was taken into consideration during the static strength simulation. The FEM structural study makes use of an aluminium alloy, which is shown to have the following physical properties in Table 2.10. In the meantime, the grid sensitivity study can be seen in Table 2.11. The researchers discovered that the threshold grid number is somewhere around 0.16 million elements.

**Table 2.10** Physical properties of aluminium alloy

| Property               | Value        |
|------------------------|--------------|
| Young's modulus        | 71 (Gpa)     |
| Density                | 2800 (kg/m3) |
| Poisson's ratio        | 0.33         |
| Tensile yield strength | 420 MPa      |

**Table 2.11** Grid sensitivity analysis of fan rotor stress (Zhaoyun Song et al., 2023)

| Grid number<br>(million) | Maximum stress<br>(Mpa) |
|--------------------------|-------------------------|
| 0.04                     | 318                     |
| 0.1                      | 321                     |
| 0.16                     | 322                     |
| 0.22                     | 322                     |

It was discovered through the FEM analysis of the fan rotor that the maximum stress of the rotor is 321 MPa. This value is lower than the material's yield limit of 420 MPa, which was shown to be the case thanks to the mesh and stress distribution diagram.

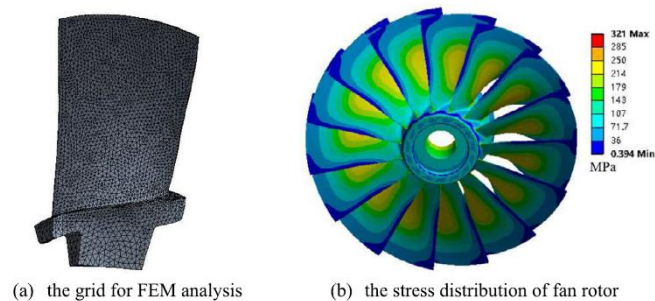


**Figure 2.24** Grid and stress distribution diagram for fan motor FEM analysis (Zhaoyun Song et al., 2023)

Zhaoyun Song et al. (2023) use two optimisation strategies to validate the curvature-constrained aero-structural multi-disciplinary optimisation design method. Optimisation A is based on the aerodynamic PC-Kriging model and the blade curvature constraint function. Alternatively, Optimisation B uses an aerodynamic PC-Kriging model without blade curvature constraints. Optimisation A's objective function is maximum efficiency at the optimisation point, the aerodynamic constraint is the blade's maximum spanwise curvature, and the mass flow and pressure ratio fluctuation is less than 5%. Table 2.12 compares the design point performance of baseline, optimisation A, and B.

**Table 2.12** Comparison of design point performance of Baseline, Optimization A, and Optimization B (Zhaoyun Song et al., 2023)

| Performance    | Baseline | Optimization A | Optimization B |
|----------------|----------|----------------|----------------|
| Mass flow      | 0.937    | 0.937          | 0.939          |
| Pressure ratio | 1.591    | 1.599          | 1.591          |
| Efficiency     | 85.6%    | 87.4%          | 87.7%          |

Figure 2.25 compared the stress levels of the control group with those of the A and B optimisations. Clearly, the maximum stress for Optimisation A is lower than the yield limit of the material (344 MPa), while the maximum stress for Optimisation B is higher than the yield limit of the material (420 MPa). As a result, Optimisation B is inadequate for the materials in question. Results like this prove that the curvature constraint-based interdisciplinary optimisation design method is the way to go.

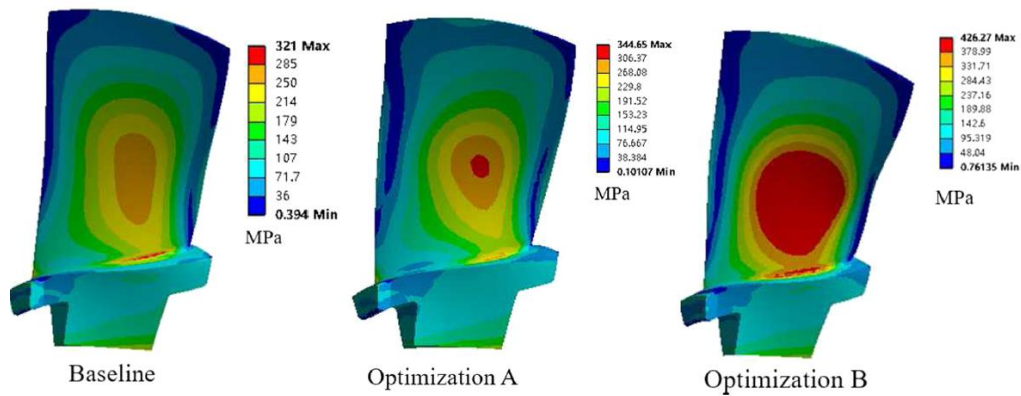


**Figure 2.25** Comparison of the static stress of Baseline, Optimization A, and Optimization B (Zhaoyun Song et al., 2023)

According to the research conducted by Zhaoyun Song et al. (2023), the structural performance will go over the yield limit of aluminium alloy material if aerodynamic optimisation is performed without considering the blade curvature limits. Aerodynamic optimisation without blade curvature limitations and the approach suggested in the research both boost isentropic efficiency by 1.8% and 2.1%, respectively. Therefore, the maximum stress on the blade could be reduced by 19.5% using the proposed method with minimal impact on aerodynamic performance.

UNIVERSITI TEKNIKAL MALAYSIA MELAKA

#### 2.4.5 Experimental study on blade thickness on the overall and local performance of axial-flow fan

After considering blade curvature constraints, axial-flow fan blade thickness affects performance. J. Hurault et al. (2010) stated that blade shape modification may reduce noise or increase operating range and actuator need. For years, aeronautics and automotive engineers have exploited blade thickness to change lift, drag, and boundary layer separation. C. Sarraf et al. (2011) examined how blade thickness affects axial-flow fan performance. Two ISO-5801-compliant axial-flow fans with different blade thicknesses were compared

for aerodynamic performance. Both aluminium fans have the same geometry except for blade thickness. Figure 2.26 shows a thick-bladed fan with hub, mid-span, and tip drawings.

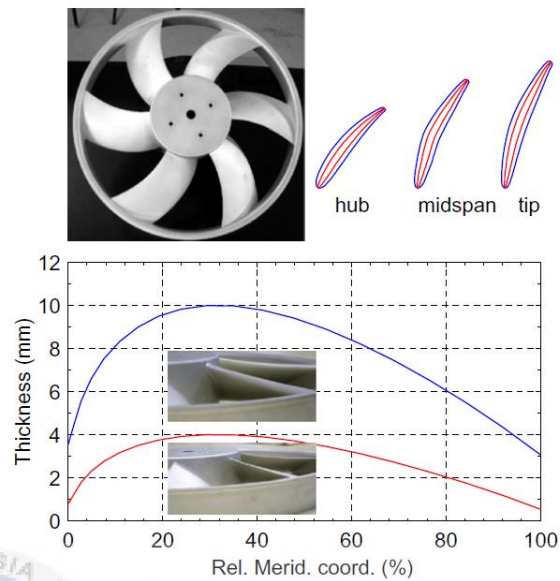


**Figure 2.26** Views of the two fans, Front view, sections of thick and thin profiles at various span locations and thickness distribution law along the meridional coordinate (C. Sarraf et al., 2011)

**Table 2.13** Blade cascade parameters for the reference  $F_A$  (C. Sarraf et al., 2011)

|          | $R$<br>(mm) | $c$<br>(mm) | $\sigma$ | $\gamma$ (°) | Profile          | $D$       |
|----------|-------------|-------------|----------|--------------|------------------|-----------|
| Hub      | 65.4        | 66.6        | 0.97     | 53           | NACA<br>65(07)06 | 0.37<br>2 |
| Mid-span | 122.<br>2   | 74.0        | 0.58     | 66           | NACA<br>65(10)05 |           |
| Tip      | 179         | 81.3        | 0.43     | 70           | NACA<br>65(11)05 | 0.65<br>0 |

Table 2.13 summarises cascade blade properties. The thin blade axial-flow fan  $F_A$  has a maximum blade thickness of 4 mm, or 5.6% of the chord length at mid-span, while  $F_B$  has a maximum of 10 mm, or 13.5%. C. Sarraf et al. (2011) found that thickness affects performance, fan blade pressure, and velocity fluctuations. Performance was comparable, with the thick blades fan dropping 8% of pressure rise at conception flow rate, having a

maximum efficiency 3% lower than the thin blades fan, and shifting towards lower flow rates.

Summary of prior thesis heat management studies: Studies have examined replacing fan blades made of glass fibre-reinforced plastic (GFRP) with jute fibre to improve biodegradability and service life. Researchers examined the mechanical and tensile properties of jute fibre composites with glass fibre-reinforced plastic to determine if they might be improved. Meanwhile, fan-cooling system design has been studied to reduce noise. The research sought to improve the design and quiet the fan at high speeds. This article examines how a small inlet duct on an axial fan's inlet shroud reduces noise. Researchers analysed axial and sweeping blade fans' acoustics to determine which makes more noise. Then, blade curvature and thickness effects on axial fan performance were examined. Instead, these studies are used to cool electrical components and GPUs to improve thermal management.

## 2.5 Liquid Cooling

The growth of high-powered electronic devices and electronic technology is exponentially raising the system's temperature. There are superior cooling strategies that have been investigated. Fan-cooling and liquid cooling are popular for CPU and GPU cooling. According to J. Seymour et al. (1986) and F.Meng et al. (2017), since the 1980s (Cray-2), liquid systems have been employed in large-scale electronics due to their larger heat capacities and thermal conductivities than air. Since commercial liquid cooling systems are more efficient than air cooling for a given size, they are increasingly used in electronic equipment. A conventional liquid cooling system has a heat removal block, pump, radiator, and fan. Often prefilled with liquid and connected by pipes.

Technically, liquid cooling technology pumps water from the reservoir into the water tank through the water pipe, out through another port, and back into the reservoir. Heat from GPUs, CPUs, and motherboards can be removed by the reciprocating cycle. A copper or aluminium water-cooling block can dissipate CPU heat. Thus, water-cooling blocks serve the same purpose as air-cooling blocks. See Figure 2.27 for the only difference: the water cooling block must have a passage for circulating liquid to go through before sealing.

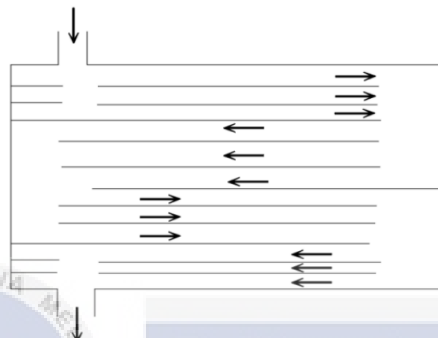


**Figure 2.27** Schematic diagram of water cooling block channel

To avoid electrical short circuits from liquid leaks, this is done. Although liquid cooling uses a different medium than air cooling, its large heat capacity allows it to absorb a lot of heat while raising temperatures somewhat. Water pumps improve system fluid flow. The CPU heat-absorbing liquid flows away from the CPU while the lower-temperature liquid continues to flow. A liquid cooling system uses a pipe to transport water between a pump, a water-cooling block, and a storage tank via a closed channel. This section describes liquid-cooling system optimisation, including choosing working fluids, designing water-cooling blocks, and researching dimension parameters.

Liquid cooling fluid development is being studied to increase electronic device cooling system thermal performance. Water is de-ionised in most liquid cooling systems. Lower cost and higher heat capacity than air cooling. A fluid may be ethylene glycol. Equal ethylene glycol boils higher and freezes lower than water. Nanoparticle-based fluids conduct heat better. The replacement of working fluids by nanofluid is significant. Heat-transferring

nanofluids cool faster. Nanoparticles improve heat transmission by reducing fluid resistance.

Tables by Harun and Cik Sidik (2021) examined hybrid and nanofluid research. The summary table follows.

**Table 2.14** Summary of the application of nanofluid or hybrid nanofluid in the liquid cooling system for CPU (Harun & Cik Sidik, 2021)

| Authors  | Nanofluids   | Findings   |
|--|--|--|
| Zhao <i>et al.</i> , [9]                               | TiO <sub>2</sub> -water  | Nanofluids with 0.3% concentration can improve the cooling performance by 58% at most compared with deionized water under the identical conditions   |
| Hassan <i>et al.</i> , [10]                            | Al <sub>2</sub> O <sub>3</sub> -water, CuO-water, SiO <sub>2</sub> -water, ZnO-water | The SiO <sub>2</sub> nanofluid has the highest Nusselt number value, followed by Al <sub>2</sub> O <sub>3</sub> , ZnO, and CuO. The highest heat transfer enhancement showed by SiO <sub>2</sub> with 14% enhancement.   |
| Gunnasegran <i>et al.</i> , [11]                       | Fe <sub>2</sub> NiO <sub>4</sub> - water   | An average decrease of 5.75°C (14%) was achieved in core temperatures of desktop PC CPU using Fe <sub>2</sub> NiO <sub>4</sub> -H <sub>2</sub> O   |
| Sarafraz <i>et al.</i> , Bahiraei <i>et al.</i> , [13] | Liquid gallium<br>Graphene/Ag-water  | Results demonstrated that both coolants present a higher Nanofluid has better cooling than pure water, reduction of surface temperature due to adding the nanoparticles is more obvious at lower Reynolds numbers. Applying the nanofluid increases the uniform distribution of temperature.                 |
| Sun <i>et al.</i> , [14]                               | Cu-water<br>Al <sub>2</sub> O <sub>3</sub> -water                                    | The convective heat transfer coefficient of nanofluids with a mass fraction of 0.1–0.4% was significantly higher than deionized water, and the convective heat transfer coefficient of Cu-water nanofluids was about 1.1–2 times the heat transfer coefficient of the DI water.                              |
| Al-Rasheed <i>et al.</i> , [15]                        | CuO-water  | The results show 7.7% heat transfer improvement in thermal conductance is observed in the case of nanofluids in comparison to water.   |
| Gunnasegaran [16]                                      | SiO <sub>2</sub> -water  | The optimized nanoparticle mass concentration and heat inputs are 0.48% and 59.97 W, respectively, the minimum R <sub>th</sub> being 2.66 (C/W)  |
| Turgut <i>et al.</i> , [17]                            | Al <sub>2</sub> O <sub>3</sub> -water  | With 1% volume concentration, nanofluid decreases the maximum temperature of the system, almost 2.7°C compared to water  |
| Nazari <i>et al.</i> , [18]                            | Al <sub>2</sub> O <sub>3</sub> -water<br>CNT-water                                   | An increase of 6% is also reported by using a 0.5% volume fraction of Alumina nanofluid. The best heat transfer enhancement (about 13%) is related to CNT nanofluids with the volume fraction of 0.25% for the flow rate of 21 mL/s.   |
| Jajja <i>et al.</i> , [19]                             | MWCNT-water  | The lowest value of heat sinks base temperature recorded was 49.7°C at a heater power of 255W by using a heat sink of 0.2mm fin spacing and MWCNT nanofluid as a coolant.  |
| Yousefi <i>et al.</i> , [20]                           | Al <sub>2</sub> O <sub>3</sub> -water  | Introduction of 0.5 wt% Al <sub>2</sub> O <sub>3</sub> nanoparticles to the water coolant of heat pipe has led to a decrease in thermal resistance. It is shown that at 10 W, the presence of nanofluid has reduced the thermal resistance by 15%, while at 25 W, the thermal resistance has dropped by 22%. |
| Putra <i>et al.</i> , [21]                             | Al <sub>2</sub> O <sub>3</sub> -water  | Application of Al <sub>2</sub> O <sub>3</sub> nanofluid as working fluid would enhance the thermal performance of the vapor chamber by 9% compare with based fluid.  |

Harun and Cik Sidik (2021) conducted a literature review in which the thermal performance of nanofluid was compared to that of base fluid. According to the research conducted, the type of nanofluid, volume concentration, flow rate, and temperature all play a role in the thermal performance of the cooling device. Table 2.14 provides a summary of the nanofluids utilised in liquid CPU cooling systems, along with an examination of their heat transfer coefficients, as presented by Harun & Cik Sidik (2021).

**Table 2.15** Applications of nanofluid or hybrid nanofluid with heat transfer coefficient  
(Harun & Cik Sidik, 2021)

| Cooling device | Nanofluids                            | Vol. concentration (%)                          | Heat transfer coefficient (Maximum Enhancement)                 | Authors                     |
|----------------|---------------------------------------|---|---|-----------------------------|
| Microchannel   | Carboxymethy                          | 0 - 3   | 386.01 W/m <sup>2</sup> K                                       | (Al-Rashed et al., 2019)    |
| Heat sink      | Cellulose/CuO-water                   |   |   |                             |
| Heat sink      | Gallium                               | 0.1 - 0.3                                       | Gallium = 600 W/m <sup>2</sup> K                                | (Gunnasegaran et al., 2017) |
|                | CuO-water                             |   | CuO = 400 W/m <sup>2</sup> K                                    |                             |
| Heat sink      | Cu-water                              | 0.1 - 0.4                                       | Cu-water = 11100 W/m <sup>2</sup> K                             | (Sun & Liu, 2017)           |
|                | Al <sub>2</sub> O <sub>3</sub> water  |   | Al <sub>2</sub> O <sub>3</sub> -water = 8400 W/m <sup>2</sup> K |                             |
| Heat sink      | Al <sub>2</sub> O <sub>3</sub> -water | 0.1 - 0.25                                      | Al <sub>2</sub> O <sub>3</sub> -water = 340 W/ m <sup>2</sup> K | (Nazari et al., 2014)       |
|                | CNT-water                             |   | CNT-water = 365 W/m <sup>2</sup> K                              |                             |
| Heat sink      | SiO <sub>2</sub> -water               | SiO <sub>2</sub> : 0.5, 1.0, 1.5                | SiO <sub>2</sub> -water = 1000 W/m <sup>2</sup> K               | (Hasan et al., 2018)        |
|                | TiO <sub>2</sub> -water               | TiO <sub>2</sub> : 0.1, 0.25, 0.5               | TiO <sub>2</sub> -water = 920 W/m <sup>2</sup> K                |                             |
|                | Al <sub>2</sub> O <sub>3</sub> -water | Al <sub>2</sub> O <sub>3</sub> : 0.5, 0.75, 1.0 | Al <sub>2</sub> O <sub>3</sub> -water = 1250 W/m <sup>2</sup> K |                             |
| Heat Sink      | CuO-water                             | 0.1 and 0.2                                     | 1900 W/m <sup>2</sup> K   | (Bahiraei et al., 2018)     |

It is challenging to compare the best nanofluids using the heat transfer coefficient analysis because of the wide range of concentrations and heat producing methods. The uneven distribution of nanofluid at heat sinks is the subject of additional research. The rate at which various nanofluids improve heat transmission varies. Nanofluids' enhanced heat transmission can be attributed to their high thermal conductivity. The thermal conductivities of several nanoparticles are listed in Table 2.16 below.

**Table 2.16** Thermal conductivity of nanoparticles (Harun & Cik Sidik, 2021)

| Nanoparticles | Thermal Conductivity (W/mK) | Authors                 |
|---------------|-----------------------------|-------------------------|
| Water         | 0.6                         |                         |
| $Al_2O_3$     | 36                          | (Rafati et al., 2012)   |
| $SiO_2$       | 1.2                         |                         |
| ZnO           | 13                          |                         |
| CuO           | 440                         | (Sarafraz et al., 2017) |
| Gallium       | 29.4                        |                         |
| Cu            | 401                         | (Sun & Liu, 2017)       |

A study on nanofluid thermal conductivity discovered that the concentration and temperature of base fluid nanoparticles have a big effect on their thermophysical properties. Liquid cooling heat transfer is hard to examine with thermal conductivity alone. Enhancing thermal performance requires nanofluid concentration. Harun & Cik Sidik (2021) found nanofluid concentration improves heat transfer. Most studies use 5% nanofluid in liquids, limiting results. Mehrali et al. (2014) say concentration destabilises graphene nanoplatelets. Thus, nanofluid concentration enhances heat transmission but decreases stability. Consider the heat sink's micron- or millimetre-wide channel when calculating nanofluid concentration. Clogged nanofluid channels might lower pressure or damage the cooling system if the nanoparticles are numerous. Nanofluid concentration depends on the size of the heat sink.

### 2.5.1 Performance analysis and structural optimization of a finned liquid-cooling radiator for chip heat dissipation

Meanwhile, He et al. (2022) constructed a finned water-cooled radiator and examined its operational performance. This was done as part of an effort to analyse and optimise the radiator's performance for chip heat dissipation. Their research examines how varying the radiator's inlet and outlet locations, fin height, thickness, and spacing affect the radiator's

thermal resistance and flow resistance performance. Liquid cooling system optimisation was the basis for the research done by He et al. (2022). In addition, He et al. (2022) used COMSOL simulation software to test and verify the results by experimental findings, providing a more credible assessment of the finned water-cooled radiator's thermal resistance performance. Water input and exit locations, fin-covered area, and fin sizes were used to optimise the radiator's structure. The optimisation structure's flowchart is depicted in the following figure:

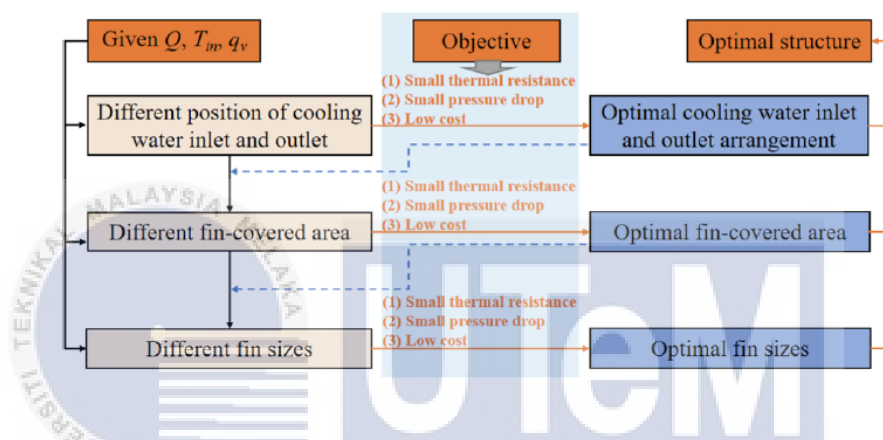


**Figure 2.28** Flow chart of the optimization procedure (He et al, 2022)

He et al. (2022) examined the performance of a diagonal and a central layout for the input and output of cooling water in terms of optimisation. The equipment parameters used in the experimental water cooling system by He et al were shown in table below:

**Table 2.17** Equipment parameters used in the experimental water-cooling system (He et al, 2022)

| Equipment Name               | Specific Parameter Value  |
|------------------------------|---|
| Air cooled chiller           | Rated refrigerating capacity: 5.3 kw  |
| Water Pump                   | Rated flow: $2 \text{ m}^3/\text{h}$ ; rated power: 750 W   |
| Plate heat exchanger         | Heat transfer coefficient: $2025 \text{ WK}^{-1}$ ; heat exchange area: $0.81 \text{ m}^2$ .                                  |
| Finned water-cooled radiator | $L_f = 72.6 \text{ mm}$ , $W_f = 0.8\text{mm}$ , $H_f = 3.5 \text{ mm}$ , $S_f = 0.45 \text{ mm}$ , the number of fins is 38. |

The results showed that the thermal resistances and costs of radiators in a central layout were very similar to those in a diagonal arrangement. However, when the water flow rate was greater than  $0.4 \text{ L min}^{-1}$ , the pressure loss was smaller under the central configuration. The central layout type was advocated by He et al. in 2022.

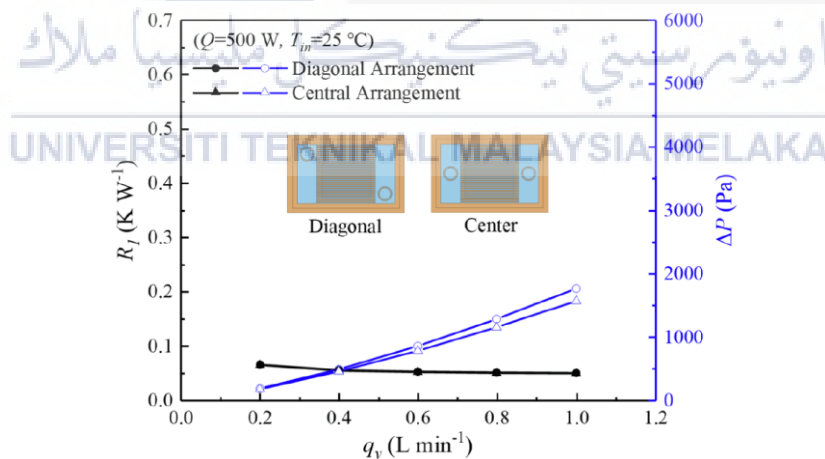


**Figure 2.29** Thermal resistance and pressure drop of the radiator under different inlet and outlet modes (He et al, 2022)

In addition, He et al., who optimised the fin-covered area for water cooling, discovered that the radiator thermal resistance is minimised when the area of the fin-covered plate is in close proximity to the chip region. In addition, the material and running costs of

the radiator can be reduced by adopting a smaller fin area radiator. However, the radiator pressure drop was reduced noticeably when the fin area was progressively increased. Therefore, the fin-covered plate with a 25mm x 25mm area was recommended after taking into account the operational costs, the impacts of heat dissipation, and the pressure drop. He et al. optimised not only the fin-covered area but also other critical parameters, including the fin height ( $H_f$ ), spacing ( $S_f$ ), and thickness ( $W_f$ ) inside a radiator. He and his colleagues discovered that reducing the fin spacing had a dramatic effect on chip temperature. In order to effectively dissipate heat from a chip, its fins should be tall, thin, and closely spaced.

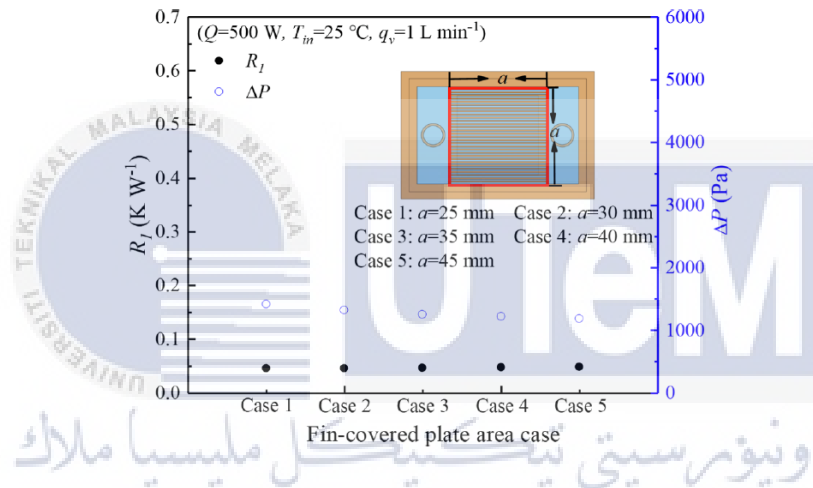


**Figure 2.30** Thermal resistance and pressure drop for different areas of the fin-covered plate for the radiator. (He et al, 2022)

Heat dissipation and pressure drop evaluations demonstrate that bigger fin height and thinner fin thickness are better for both aims. He et al. (2022) recommended a radiator with 0.5 mm fin thickness and 5 mm fin height. This is because high fin height increases radiator area and running costs. He et al. (2022) optimised a liquid-cooled system's structure design using data, including a central arrangement type for water inlet and outflow locations and a fin-covered plate size equal to the chip area. By increasing fin height, decreasing thickness, and increasing distance, a radiator's pressure drop can be reduced, while heat can be better dissipated. Fins with a 5mm height, 0.5mm thickness, and 1mm spacing are best for thermal resistance and pressure drop

## 2.5.2 Evaluation of Water-Cooling Heat Sink Performance and Dynamic Flow Effect

Wang et al. (2019) conducted extensive testing on three water-cooled heat sinks with different pin fins to identify which one had higher heat transfer and flow performance after He et al. (2018) covered the ideal structure of a heat sink. As can be seen in the figure below, the pin fins came in three distinct shapes: square, circular, and drop-shaped.

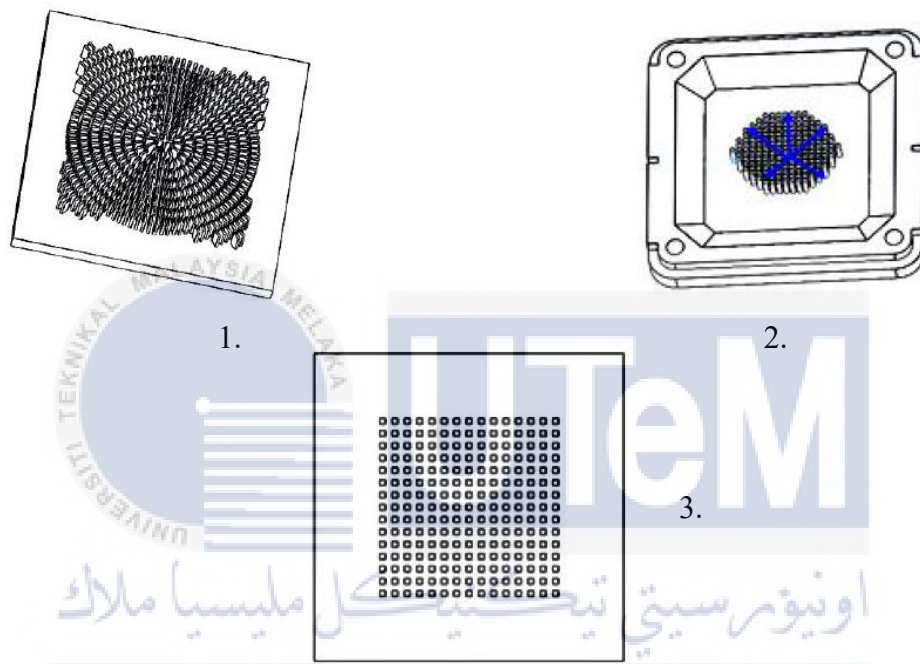


**Figure 2.31** Structure of heat sink (1) Drop-shaped pin fin, (2) Circle pin fin, (3) Square pin fin (Wang et al, 2019)

The main parameter of the heat sinks are shown in table below:

**Table 2.18** Main parameters of heat sink (Wang et al, 2019)

| Radiator size<br>(LxWxH)<br>mm | Pin height<br>mm | Pin<br>diameter<br>mm | Column<br>spacing mm |
|--------------------------------|------------------|-----------------------|----------------------|
| 40*40*40                       | 3.72             | 0.74                  | 0.8                  |

To find out if the flow inside the radiator is laminar or turbulent, the Reynolds number must be calculated. The formula for calculating the Reynolds number (Re) is provided in the following equation:

$$Re = \frac{\rho U_{max} D}{\mu} \quad (2.1)$$

Where  $\mu$  is the dynamic viscosity of the air,  $U_{max}$  is the velocity at the minimal section area.

$$Nu = \frac{h_{av} D}{\lambda_f} \quad (2.2)$$

According to Wang et al. (2019) findings, the Nu number is highest for a heat sink with a square pin fin and lowest for one with a circular pin fin. When compared to other pin fins, the drop-shaped fin had superior flow performance and was closer to the streamlined structure, resulting in lower flow resistance. Heat sinks with square pin fins provide the best all-around results in terms of energy savings during careful control of coolant flow, and they use the least energy in terms of pump power. Based on their findings, Wang et al. conclude that a heat sink's overall performance is a more significant factor in determining cooling energy use.

UNIVERSITI TEKNIKAL MALAYSIA MELAKA

### **2.5.3 Study of an adjustable closed-loop liquid-based thermoelectric electronic cooling system (LTEEC) for variable load thermal management.**

Internal heat from tiny electronic components has increased rapidly due to higher power densities. To remove excess heat and extend the lives of these electrical components, a high-performance, cost-effective cooling system is needed. Siddique et al. (2019) used a closed-loop liquid-based thermoelectric electronic cooling (LTEEC) system with variable thermal load in order to devise an energy-efficient and environmentally friendly closed-loop liquid-based thermoelectric cooling (LTEEC) system that can be adjusted to meet thermal loads. Siddique et al. (2019) evaluated LTEEC and commercial system coefficients of

performance (COP). The suggested LTEEC system was tested in two scenarios. The system received 8.8 W to 16.7 W in the first scenario. Next, the system was heated to 70–80 degrees Celsius. An air conditioner was activated at 70 degrees Celsius. In comparison, the second scenario required the same operational power input and cooling system activation.

Siddique et al. (2019) found that the radiator in the commercial system led to a heating plateau. Both cooling systems were set to kick on between 70 and 80 degrees Celsius. The LTEEC system required 5.4 W of cooling power to get to about 32°C, while the commercial system only got to around 30°C. The LTEEC system has been shown to be more effective at reducing temperatures than the commercial system when subjected to the same cooling load. The figure below shows a comparison between the LTEEC system and a commercial system in terms of temperature trends over time.

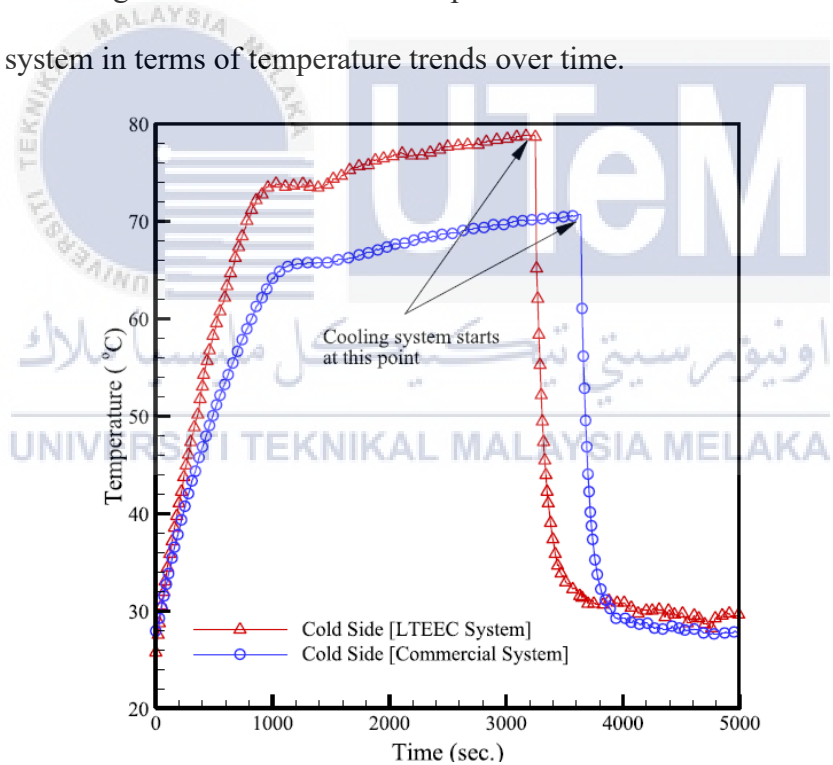


**Figure 2.32** Comparison between the commercial and the proposed LTEEC system for heater input power of 16.7W and the cooling system power of 5.4W (Siddique et al., 2019)

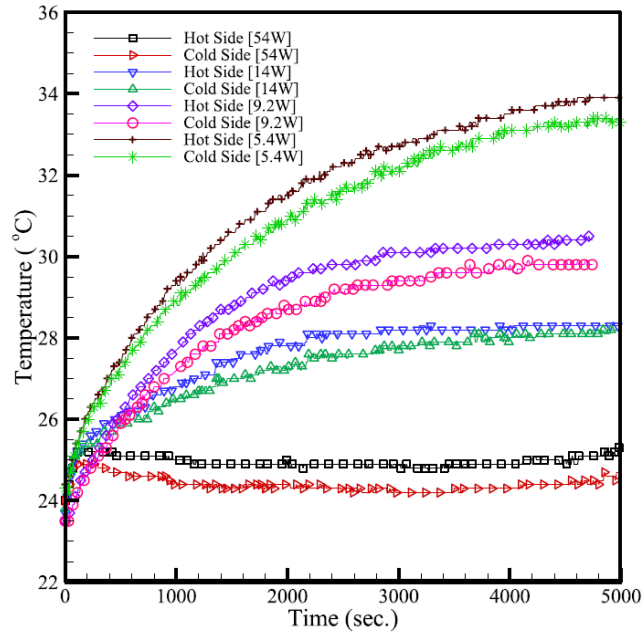


**Figure 2.33** Comparison between different power inputs to proposed LTEEC system  
(Siddique et al., 2019)

Comparing the proposed LTEEC system's performance for power inputs from 5.4W to 54W shows that the temperature rises progressively in all experimental tests except Test 1. This likely happened because the mechanism removed more heat quickly than the heater could. Other systems must reach equilibrium before dispersing heat. The mass flow rate ( $\dot{m}$ ), cold water (TCW) entering the heat exchanger, and hot water (THW) exiting the heat exchanger are needed to calculate the coefficients of performance (COPs) of LTEEC and commercial cooling systems. COP analysis showed that the proposed LTEEC system has a COP of 3.21, whereas the commercial system had a COP of 2.81. Siddique et al. (2019) proposed adding a TE module to the liquid cooling system to improve it, and the LTEEC system had a higher COP than commercial systems. To improve the LTEEC system, the author suggested changing the radiator, cooling fan, fins, insulation, etc.

## 2.6 Heat Sink

Active and passive heat are both produced by many electronic devices. In order to maintain a comfortable body temperature, a lot of individuals rely on high-powered thermal cooling systems. Many studies have looked into different approaches to cooling components. Heat sinks are commonly used to passively cool electronics. The effect of heat sink design, fin width, fin height, and heat sink variety on thermal dissipation resistance has been studied by scientists. Then, Naphon et al. (n.d.) commonly used mini-channel and micro-channel heat sinks to examine the efficacy of nanofluid jet impingement on heat transfer and flow. Heat pipes, because of their capacity for heat transmission, are the most dependable and structurally simple means of heat dissipation among heat sink components. A heat pipe is referred to as a "thermal super conductor" due to its extremely high thermal conductivity compared to other materials. In a closed system, heat is transferred through the evaporation and condensation of the working fluid. The working fluid's frequent evaporation and condensation cycles allow the heat pipe to transfer more heat than regular conductors.

Significant advancements have been made over the past decade in the areas of material utilisation, design, optimisation, miniaturisation, and weight reduction while attaining increased heat flux capacity. The heat sinks are employed to allow the heat pipe to go through forced convection cycles of evaporation and condensation. It will discuss the materials that have been used in previous heat sink literature reviews. This is mostly attributable to the improvement of materials and working fluids that can dissipate heat more effectively. Electrical, electronic, aircraft, spacecraft, and other uses have found heat pipes indispensable. Due to this, flexibility in terms of operating temperature and geometrical form has resulted. Heat pipes have been the subject of extensive research, with factors like thermal conductivity and fluid compatibility taken into account.

### 2.6.1 Studies of material used in Heat Pipe

Identifying a container, wick, and welding materials that are compatible with one another and with the working fluid of interest determines the material of the heat pipe used to improve quality of life. If one of the heat pipe's components doesn't work well with the others, the whole thing can lose efficiency. Within the heat pipe, the components may undergo chemical reactions or set up a galvanic cell. To that purpose, Narendra Babu and Kamath (2015) have developed a table showing the most recent data on the compatibility of metals with working fluids for heat pipes.



**Table 2.19** Compatible and Incompatible materials suitable for different working fluids (Narendra Babu & Kamath, 2015)

| Working Fluid | Compatible Material   | Incompatible Material | Working Fluid | Compatible Material  | Incompatible Material                                    |
|---------------|---|-----------------------|---------------|--|--|
| Water         | Stainless Steel, Copper, Silica, Nickel, Titanium           | Aluminium, Inconel    | Lithium       | Tungsten, Tantalum, Molybdenum, Niobium                      | Stainless Steel, Nickel, Inconel,                        |
| Ammonia       | Aluminium, Stainless Steel, Cold Rolled Steel, Iron, Nickel |                       | Sodium        | Stainless Steel, Nickel, Inconel, Niobium                    | Titanium   |
| Methanol      | Stainless Steel, Iron, Copper, Brass, Silica, Nickel        | Aluminium             | Cesium        | Titanium, Niobium, Stainless Steel, Nickel-based superalloys |  |
| Acetone       | Aluminium, Stainless Steel, Copper, Brass, Silica           |                       | Mercury       | Stainless Steel  | Molybdenum, Nickel, Tantalum, Inconel, Titanium, Niobium |
| Freon-11      | Aluminium   |                       | Lead          | Tungsten, Tantalum   | Stainless Steel, Nickel, Inconel, Titanium, Niobium      |
| Freon-21      | Aluminium, Iron   |                       | Silver        | Tungsten, Tantalum   | Rhenium  |
| Freon-113     | Aluminium   |                       |               |  |  |
| Heptane       | Aluminium   |                       |               |  |  |
| Dowtherm      | Stainless Steel, Copper,                                    |                       |               |  |  |

The working fluids of a heat pipe can be split into four groups based on their boiling points, such as cryogenic, low, medium, and high. The table below provides examples of operating temperatures and fluids:

**Table 2.20** Heat Pipe Temperature Range (Narendra Babu & Kamath, 2015)

| Heat pipe categories | Operating Temperature (K) | Working fluids  |
|----------------------|---------------------------|---|
| Cryogenic            | 4 ~ 200                   | Helium, argon, oxygen and krypton                                     |
| Low temperature      | 200 ~ 550                 | Ammonia, acetone, Freon compounds and water                           |
| Medium temperature   | 450 ~ 750                 | Mercury, sulphur and Thermax  |
| High temperature     | 750 and above             | Sodium, lithium, cesium, silver and a sodium-potassium compound (NaK) |

Every heat pipe possesses specific temperature requirements. The effective pressure range spans from 0.1 to 20 atm, including a wide range of pressures. The upper limit of the heat pipe's temperature can only be elevated until the thermal resistance of the container reaches its maximum thickness at pressures exceeding 20 atm, whereas the vapour pressure limit must be approached below 0.1 atm. Therefore, it is imperative that the working fluids exhibit thermal stability within the designated range of operating temperatures. The design of heat pipes necessitates consideration of the working fluid in order to achieve the desired temperature range. The following table presents a compilation of prevalent working fluids, including their respective atmospheric melting and boiling temperatures, as well as their applicable temperature ranges, as reported by Narendra Babu and Kamath (2015).

**Table 2.21** Working fluids used in heat pipe (Narendra Babu & Kamath, 2015)

| Working Fluid | Melting Point, K<br>at 1 atm | Boiling Point,<br>K at 1 atm | Useful<br>Range, K | Working Fluid | Melting Point, K<br>at 1 atm | Boiling Point,<br>K at 1 atm | Useful<br>Range, K |
|---------------|------------------------------|------------------------------|--------------------|---------------|------------------------------|------------------------------|--------------------|
| Helium        | 1.0                          | 4.21                         | 2-4                | Methanol      | 175.1                        | 337.8                        | 283-403            |
| Hydrogen      | 13.8                         | 20.38                        | 14-31              | Flutec PP2    | 223.1                        | 349.1                        | 283-433            |
| Neon          | 24.4                         | 27.09                        | 27-37              | Ethanol       | 158.7                        | 351.5                        | 273-403            |
| Nitrogen      | 63.1                         | 77.35                        | 70-103             | Heptane       | 182.5                        | 371.5                        | 273-423            |
| Argon         | 83.9                         | 87.29                        | 84-116             | Water         | 273.1                        | 373.1                        | 303-550            |
| Oxygen        | 54.7                         | 90.18                        | 73-119             | Toluene       | 178.1                        | 383.7                        | 323-473            |
| Methane       | 90.6                         | 111.4                        | 91-150             | Flutec PP9    | 203.1                        | 433.1                        | 273-498            |
| Krypton       | 115.8                        | 119.7                        | 116-160            | Naphthalene   | 353.4                        | 490                          | 408-623            |
| Ethane        | 89.9                         | 184.6                        | 150-240            | Dowtherm      | 285.1                        | 527                          | 423-668            |
| Freon 22      | 113.1                        | 232.2                        | 193-297            | Mercury       | 234.2                        | 630.1                        | 523-923            |
| Ammonia       | 195.5                        | 239.9                        | 213-373            | Sulphur       | 385.9                        | 717.8                        | 530-947            |
| Freon 21      | 138.1                        | 282                          | 233-360            | Cesium        | 301.6                        | 943                          | 723-1173           |
| Freon 11      | 162.1                        | 296.8                        | 233-393            | Rubidium      | 312.7                        | 959.2                        | 800-1275           |
| Pentane       | 143.1                        | 309.2                        | 253-393            | Potassium     | 336.4                        | 1032                         | 773-1273           |
| Freon 113     | 236.5                        | 320.8                        | 263-373            | Sodium        | 371                          | 1151                         | 873-1473           |
| Acetone       | 180                          | 329.4                        | 273-393            | Lithium       | 453.7                        | 1615                         | 1273-2073          |
|               |                              |                              |                    | Calcium       | 1112                         | 1762                         | 1400-2100          |
|               |                              |                              |                    | Lead          | 600.6                        | 2013                         | 1670-2200          |
|               |                              |                              |                    | Indium        | 429.7                        | 2353                         | 2000-3000          |
|               |                              |                              |                    | Silver        | 1234                         | 2485                         | 2073-2573          |

The following table summarises some of the research conducted by various researchers to enhance the thermal performance of heat pipes by employing various materials for container, wick structure, and working fluid combinations.

**Table 2.22** Summarization of research done on material for container, wick structure and working fluid combinations (Narendra Babu & Kamath, 2015)

| Sl. No. | Type of Heat Pipe                   | Type of wick  | Type of working fluid                                    | Heat load/Thermal Resistance   | Comments  | Reference                            |
|---------|-------------------------------------|---|--|--|---|--------------------------------------|
| 1.      | Loop heat pipe                      | Sintered wick (porosity>65%)  | water  | 500 W  | Thermal resistance of 0.15°C/W for max. heat load of 500W   | Singh R <i>et.al.</i> (2014)         |
| 2.      | Loop heat pipe                      | Biomaterial<br>Sintered Powder copper   | Nano-fluid Al <sub>2</sub> O <sub>3</sub>                | 0.68°C/W<br>1.47°C/W   | The biomaterial wick decreases thermal resistance by 56.3%  | Nandy Putra <i>et.al.</i> (2014)     |
| 3.      | Sintered wick heat pipe             | Copper sintered heat pipe   | Surfactants free Cu nano particles dispersed in DI water | Heat input initially 10W & increased in steps of 10W upto 160W   | For 1Wt% Cu nano fluid heat transport capacity of heat pipe increased by 31.2%  | G Kumaresan <i>et.al.</i> (2014)     |
| 4.      | Loop heat pipe                      | Glass fibre 2.6µm pore size, Stainless steel metal wick of 10µm pore size         | DI water   | Heat input 20W to 140W in steps of 20W   | The results have shown non-metal wicks can have much greater temperature difference between heater surface and wick and the use of non-metal wick reduces thickness of evaporator | Alexander <i>et.al.</i> (2013)       |
| 5.      | Cryogenic heat pipe                 | Porous wick sintered with stainless steel   | Liquid nitrogen  | Heat load of 41W   | On primary evaporator low thermal resistance of 0.146K/W obtained   | Ya nan Zhao <i>et.al.</i> (2011)     |
| 6.      | Loop heat pipe                      | Monoporous & Bidisperse sintered porous wick of nickel particles                  | Ammonia  | Maximum tolerable heat load of 400W for monoporous wick and 575W for bidisperse wick   | Thermal resistance of the system was 0.12°C/W & of the evaporator 0.1°C/W.  | Fang-Chou Lin <i>et. al.</i> (2011)  |
| 7.      | Loop heat pipe with flat evaporator | Biporous wick of nickel powder  | Ammonia  | Heat load of 10W to 130w   | Thermal resistance varies between 1.42 and 0.33 C/W.  | Chen <i>et.al</i> (2012)             |
| 8.      | Loop heat pipe with flat evaporator | Biporous wick of nickel powder  | Methanol   | Heat load of 40W to 100W   | Loop heat pipe found to have good start up characteristics and run stably   | Huan Li <i>et.al.</i> (2012)         |
| 9.      | Loop Heat pipe                      | wick made of Nickel & Titanium particles pressed on soft matrix(Polymer envelope) | Water & Acetone  | With Ti wick and water as working fluid can transport heat load of 900W & Ni wick and Acetone as working fluid transport 300W of heat load | An advanced method of LHP wick manufacturing was proposed for high power dissipation in electronic cooling  | Leonid Vasiliev <i>et.al.</i> (2009) |

## 2.6.2 Study on the thermal dissipation performance of GPU cooling system with nanofluid as coolant

Research on the base fluid utilised within the heat pipe is being done in conjunction with the use of heat sinks. Researchers observed that the thermal properties of the base fluid used in heat pipes may be further strengthened by employing nanofluid; hence, this has led to a steady improvement in thermal flow qualities. Many studies have shown that including nanoparticles in the base fluid improves heat transfer in mini- and micro-channels of varying designs. The thermal dissipation performance of a cooling system with nanofluid applied was measured in an experiment by Siricharoenpanich et al. (2021), who employed a 0.015% by volume concentration of Ag nanofluid and de-ionised water as coolants running in the cooling system.

Nanoparticles suspended in the base fluid increased heat removal and decreased thermal resistance. Thus, this study compares GPU cooling thermal efficiency utilising de-ionised and Ag nanofluid. Siricharoenpanich et al. (2021) studied three heat sink designs. Before running the research, they considered how coolant types and flow rates might affect GPU cooling module thermal dissipation resistance. GPUs of different widths had lower temperatures as the coolant flow rate rose. Cooling capacity increases with coolant flow. However, cooling capacity expands slower than flow. Thus, increasing coolant flow speed significantly lowers GPU temperature. Experimental results are shown in Figures 2.34 and 2.35.

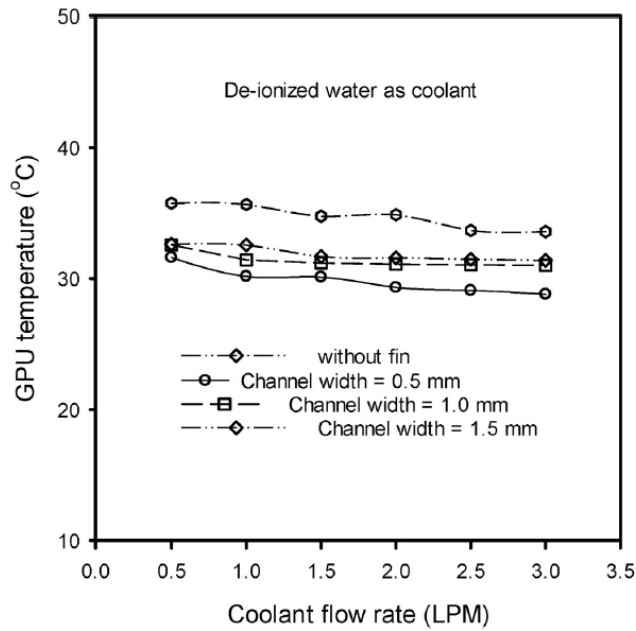


**Figure 2.34** Variation of GPU temperature for de-ionized water as coolant. (Siricharoenpanich et al. ,2021)

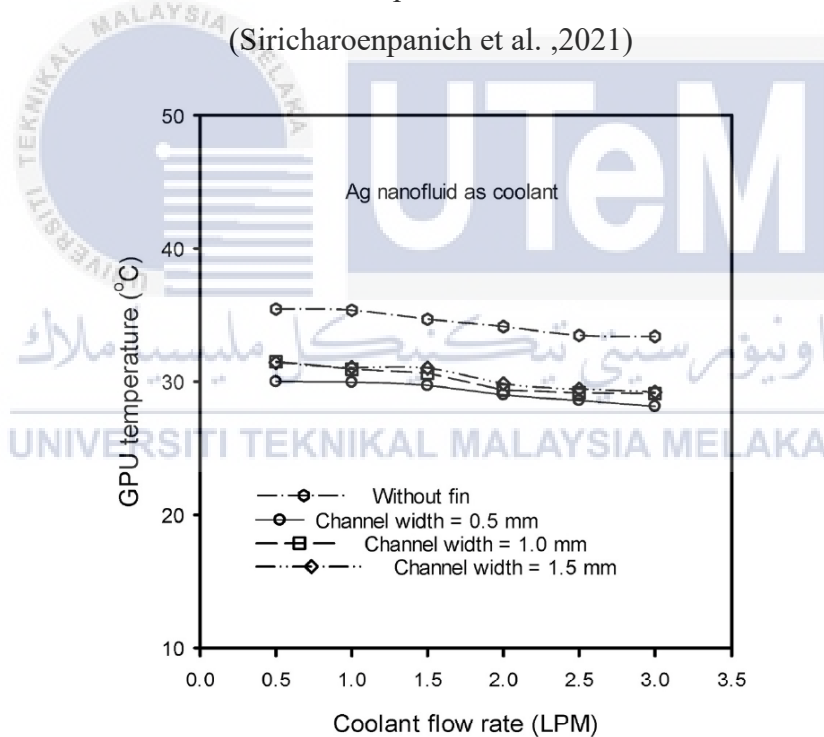


**Figure 2.35** Variation of GPU temperature for Ag nanofluid as coolant. (Siricharoenpanich et al. ,2021)

Narrower channels would increase heat transfer surface area and turbulent flow across the fin array. The heat sink with a 0.5-mm channel width keeps GPU temperatures lower than higher ones across all coolant flow rates. Nanoparticles suspended in a base fluid

result in Figure 2.36. The graph illustrates that cooling capacity increases slower than flow, resulting in GPU coolant temperature trends similar to those of de-ionised water. As fluid flows through the fin array, nanoparticles suspended in the base fluid cause Brownian motion and increased turbulent flow. Nanoparticles also change nanofluids' thermophysical properties. GPUs cooled by Ag nanofluid are cooler than those cooled by de-ionised water.

For both de-ionised water and Ag nanofluid, data for thermal resistance variations with coolant flow rate show that greater cooling capacity is achieved at higher coolant flow rates. This results in a reduction in heat resistance. The following figure illustrates the outcomes of the variations in thermal resistance with coolant flow rate for de-ionised water and Ag nanofluid as coolants.

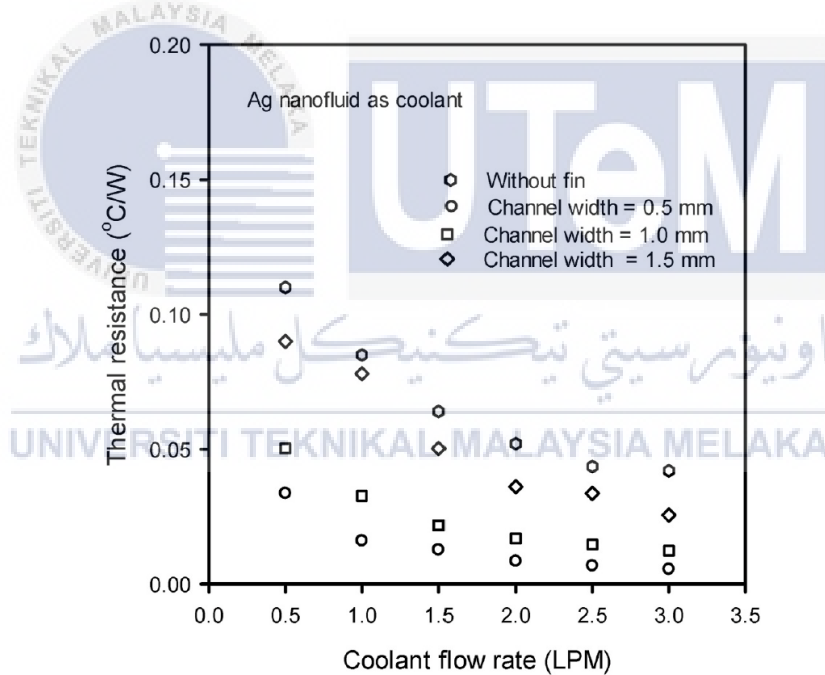


**Figure 2.36** Variation of thermal resistance for de-ionized water as coolant.  
(Siricharoenpanich et al. ,2021)

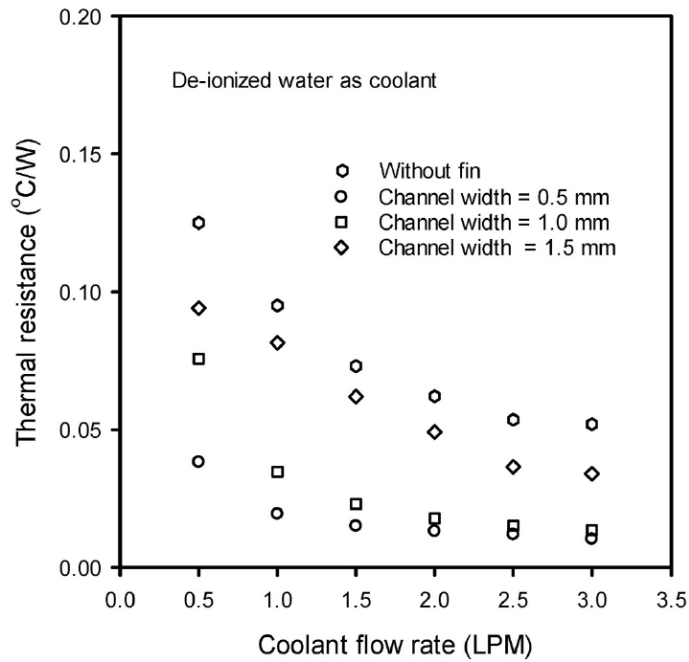


**Figure 2.37** Variation of thermal resistance for Ag nanofluid as coolant. (Siricharoenpanich et al. ,2021)

Both figure of 2.36 and 2.37 shown that coolant flow dramatically reduces thermal resistance. Flow rates exceeding 2.0 LPM steadily lower thermal resistance. A flow rate below 2.0 LPM may provide the optimum thermal resistance. Channel width greatly reduces thermal resistance in the low coolant flow rate zone. Siricharoenpanich et al. (2021) found that thermal resistance decreases with a channel width of 0.5mm. Ag nanofluid has higher heat resistance than de-ionised water as a coolant. Due to its high cooling capacity, Ag nanofluid has low thermal resistance.

### 2.6.3 Study of heat transport behaviour of micro channel heat sink with graphene based nanofluids

Nanofluid research has previously looked into the convective heat transfer properties of f-GnP (functionalized graphene nanoplatelets) suspended in distilled water. Balaji et al. (2020) conducted a study in which they measured the convective heat transfer coefficient,

temperature drop, Nusselt number, and pressure drop as a function of the mass flow rate (from 5 g/s to 30 g/s) and the concentrations of GnP (from 0% to 2.0%). Experimental measurements of the various thermophysical parameters and zeta potential analysis have been used to find out about the stability features of GnP nanofluids. Thermophysical properties were investigated to see how temperature and GnP addition affected them. The effects of changing heat loads and GnP inclusion on heat transfer performance were investigated experimentally, along with the effects of changing flow rates. Balaji et al. (2020) characterised the stability of treated GnP using a zeta potential measurement technique based on their research on the stability of nanofluids. Balaji et al.'s (2020) analysis of the literature suggests that an indicator of higher stability is a potential value that is either greater than +30 mV or less than -30 mV on average. For 0.2% vol% concentrations of GnP, the average potential values obtained following immediate preparation were -44.40 mV. Similarly, after ten and twenty days of nanofluid synthesis, the zeta potential values were -38.2 mV and -36.8 mV, respectively. According to the data, a GnP concentration of 0.2% vol. was reasonably steady. For GnP, the greatest improvement in thermal conductivity was determined to be 11% greater for 0.2% vol percentage as compared with the water at 50 °C, respectively. Figure 2.38 below shows the outcomes of thermal conductivity variations for different GnP concentrations:

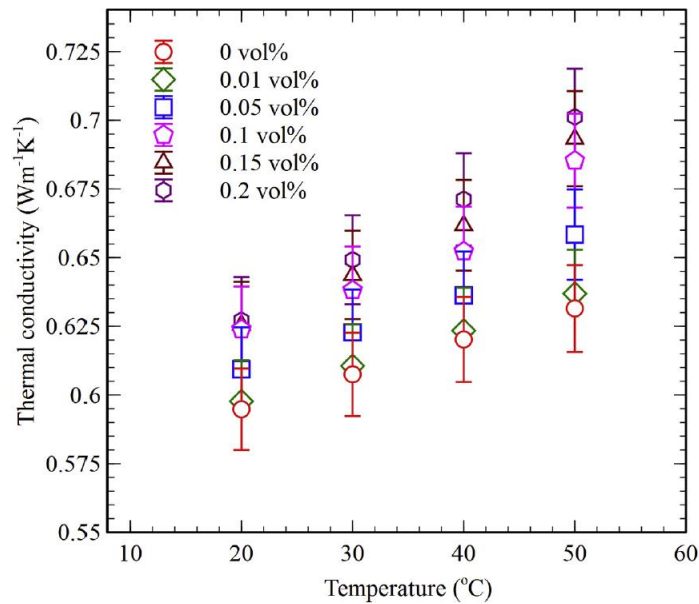


**Figure 2.38** Thermal conductivity variation for GnP (Balaji et al. ,2020)

With increased mass flow rates, the temperature difference between the nanofluid entrance and heat sink base was reduced. The heat sink's basal temperature lowers as the flow rate increases because the fluid absorbs more heat. Due to its increased thermal conductivity, GnP concentration lowers heat sink basal temperature. Balaji et al. (2020) observed that graphene-based nanofluids cooled the heat sink base to 3.12 °C better than water at 50 W. At a 200 W heat load, the highest temperature differential was 10.2 degrees Celsius lower than that of pure water. It was also shown that GnP concentration had no effect on heat sink base temperature at a lower mass flow rate. At a steady flow rate, adding 0.2 vol% GnP to a heat sink drops its base temperature by over 3°C.

The Nusselt number increases with both the mass flow rate and the GnP loading, according to a study that analysed the correlation between the two. With the addition of GnP, thermal conductivity and HTC both increase, leading to a significant increase in the Nusselt number. It was found that a difference of 7.7 percentage points existed between the experimentally obtained Nusselt number and the predicted value. When the flow rate is high, the Nusselt number rises more quickly than when the flow rate is low. This is because the

Nusselt number for convective heat transfer rises with the increasing velocity of the nanofluids because the thermal boundary layer thins. When comparing water under a heat load of 50 W and GnP loading, the latter can boost the former by as much as 20%. The progress is more obvious as the flow rates rise. The figure below shows the variation of the Nusselt number with respect to the volume fraction.

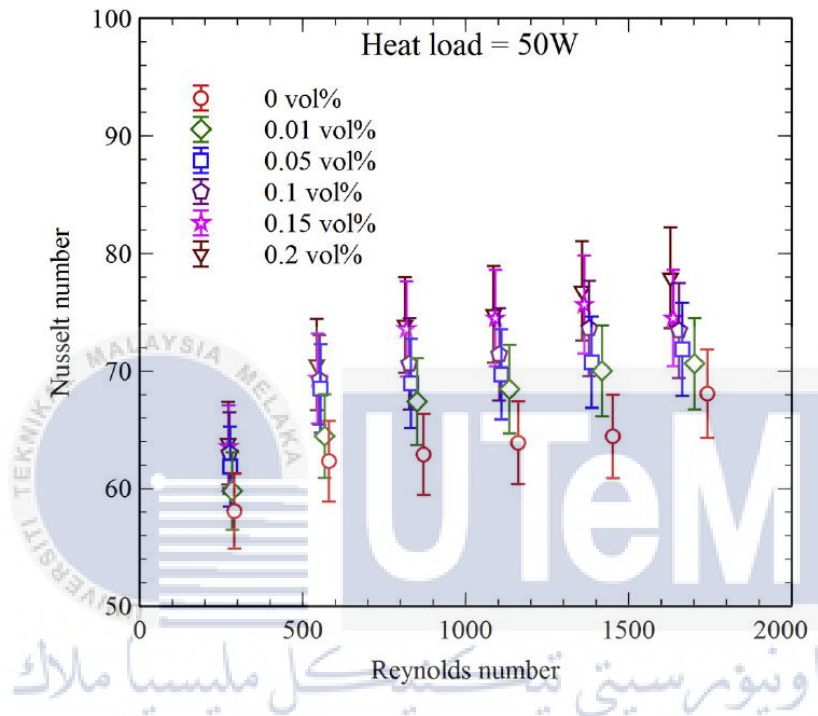


**Figure 2.39** Variation of Nusselt number at different vol% (Balaji et al. ,2020)

The nanofluids based on graphene and nanoparticles (GNP) exhibit a minimal increase in pressure drop across the microchannel heat sink, despite their exceptional heat transfer capabilities. The graph presented in Figure 2.3.3.7 illustrates the relationship between pressure decreases and both GnP concentration and mass flow rate.

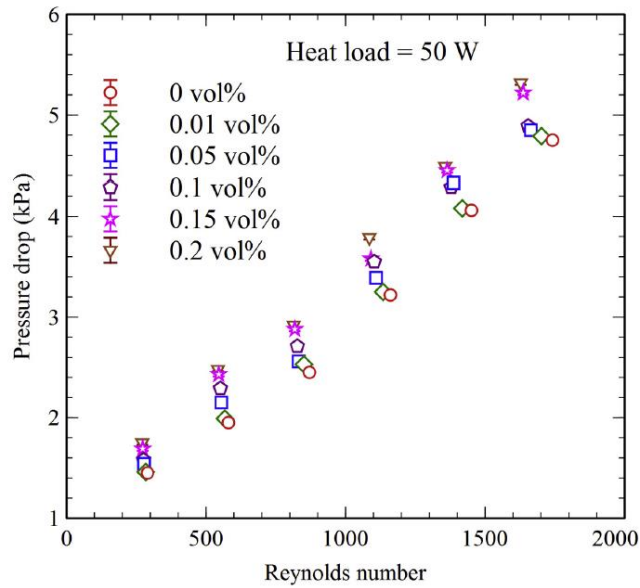


**Figure 2.40** Variation of pressure drop at different vol % (Balaji et al. ,2020)

As the mass flow rate increased, it was found that the pressure drops also increased. The addition of GnP to water raises the pressure drop. The increased pressure drop of nanofluids is mostly due to the rise in density of the nanofluids with the introduction of GnP. The highest increase in pressure drop over the base fluid with a heat load of 50 W is determined to be 12% when using a fluid with 0.2 vol% of volatile organic compounds as opposed to 0 vol%. Figure 2.41 shows how pressure drop varies as a function of mass flow rate and heat loads.

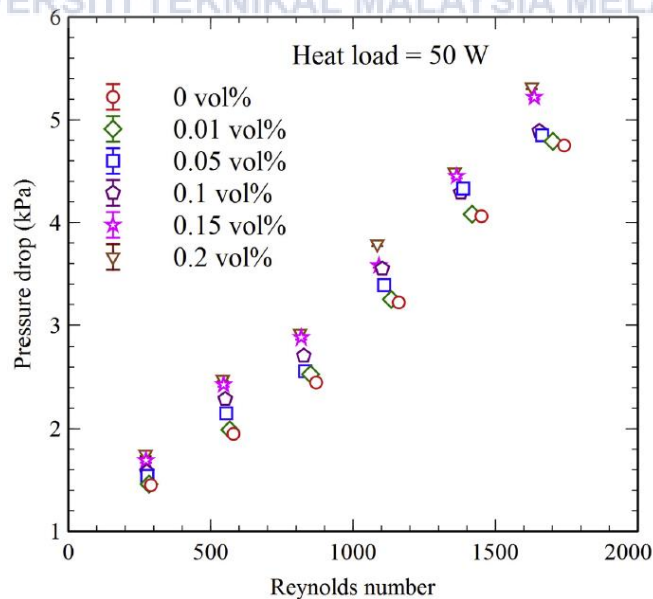


**Figure 2.41** Variations of pressure drop at different vol% (Balaji et al. ,2020)

A decrease in thermal entropy generation for GnP incorporation into pure water has been observed. Additionally, thermal entropy generation decreases as the nanofluid flow rate increases. Because nanofluids conduct heat better than water, Thus, adding GnP improves heat transfer by reducing thermal entropy formation. Balaji et al. (2020) found that thermal entropy formation decreased by 41.49% at higher volume fractions than in pure water. The diagram below shows that thermal entropy formation varies with mass flow rate for different heat loads, pure water concentrations, and 0.2 vol%.

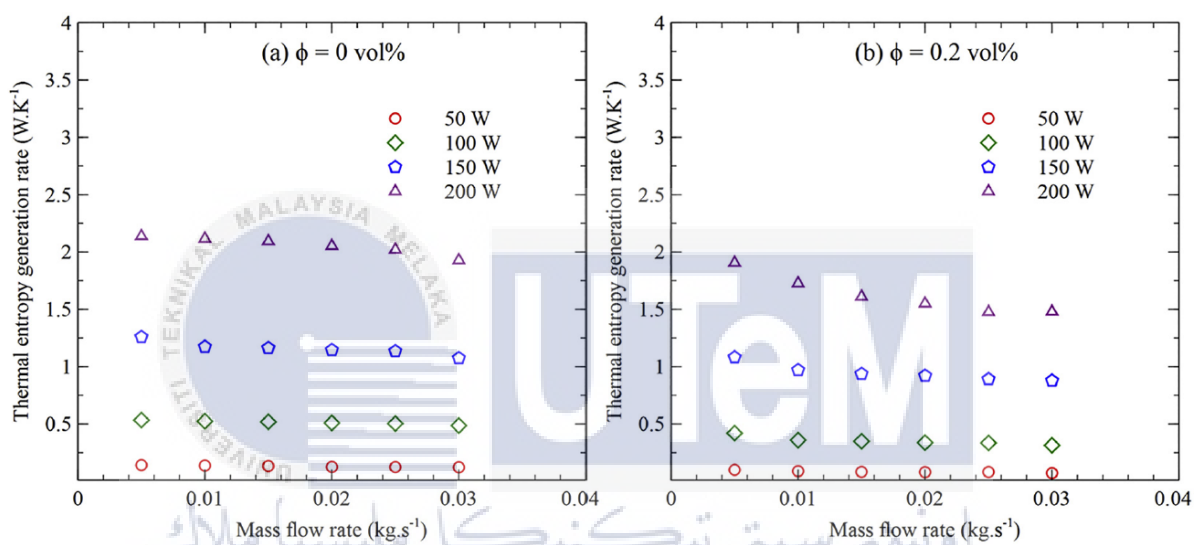


**Figure 2.42** Variation of thermal entropy generation rate. (left) Varying heat load at 0 vol%, (Right) Varying heat load at 0.2 vol% (Balaji et al. ,2020)

The zeta potential results show that GnP-based nanofluids have better convective heat transmission than water and survive longer without settling. It has 11% higher maximal heat conductivity than water. GnP's CHTC and Nusselt numbers improved 71% and 60% at 50 degrees Celsius, respectively. The functionalized GnP-based nanofluid's pressure drop increment was slightly limited by the dispersion of highly thermally conductive GnP. This can be rectified by increasing pumping capacity. Thus, functionalized GnP can replace liquid coolants in electronic systems due to its stability and heat transfer capability.

A flat heat-pipe-thermal module application in a high-end VGA card cooling system was compared to a copper-based plate embedded with three 6mm-diameter modules at 0 degrees, 90 degrees, and 180 degrees of inclination to determine its optimal thermal performance. Wang (2012) tested fin material, thickness, and spacing by optimising thermal modules. Wang (2012)'s flat heat pipe-thermal module was simulated with 165 W of input power and found that the optimal total thermal resistance is  $0.273\text{ }^{\circ}\text{C}/\text{W}$  at a 1.7 mm gap and 42 counts, with the heat source's lowest temperature being  $88.4^{\circ}\text{C}$ . Wang (2012) recommended 0.3 mm Al fins, 37 pieces of fin counts, and 1.9 mm fin spacing for a flat heat pipe-thermal module for cost and performance. When inclined horizontally, a copper-based plate with an incorporated three-heat pipe-thermal module has the best overall thermal resistance of  $0.277\text{ }^{\circ}\text{C}/\text{W}$  at a 1.7 mm gap and 42 count.

#### **2.6.4 Numerical and experimental models study on flat and embedded heat pipes applied in high-end VGA card cooling system**

In accordance with Wang (2012), the large heat flow from the GPU is quickly and uniformly dissipated by the flat heat pipe, which then conducts to the Al fins, where the heat capacity is dissipated to the ambient atmosphere, leading to a temperature difference of 2.4 degrees Celsius. It was also deduced by Wang (2012) that a flat heat pipe-thermal module with a fin gap of 1.7mm would have a total thermal resistance of no more than  $0.263^{\circ}\text{C}/\text{W}$  at low heat source temperatures. The reason for this is that with 42 fins, the fan can reach its maximum fin/cooling efficiency and quickly dissipate heat capacity, while with less than 1.5mm between them, flow resistance is excessively high, weakening fin efficiency to the point where it can't dissipate heat capacity from 46 or 52 fins and causing total thermal resistance to rise slightly. Wang (2012) conducted a thorough analysis of the results and concluded that for a high power of 180W and an inclination angle of  $180^{\circ}$ , the optimal design

for flat heat pipe and embedded heat-pipe thermal modules is 0.3 mm thickness, 1.7 mm gap, and 42 counts of aluminium fins, with a total thermal resistance of 0.232°C/W and 0.259°C/W, respectively.

Wang (2012) found that the overall thermal resistance of a flat heat pipe-thermal module is 0.232°C/W when the Al fins are 29 mm in height, 0.3 mm in thickness, 37 in number, and spaced 1.9 mm apart. Wang (2012) presented his experimental findings in the Table 2.23 below.

**Table 2.23** Experimental results for the embedded heat pipe thermal module (Wang, 2012)

| Power (W) | Inclination angles |              |              |
|-----------|--------------------|--------------|--------------|
|           | 0°                 | 90°          | 180°         |
| 180       | 0.277 (°C/W)       | 0.273 (°C/W) | 0.259 (°C/W) |
| 165       | 0.279 (°C/W)       | 0.276 (°C/W) | 0.262 (°C/W) |
| 150       | 0.281 (°C/W)       | 0.277 (°C/W) | 0.263 (°C/W) |

## 2.7 Mode of Heat Transfer

Energy can be transferred in two distinct ways: through work and through heat. Heat is the movement of thermal energy from a hotter to a colder area. A large pan of lukewarm water, on the other hand, will receive heat from a lighted match, which is a higher-temperature object. Heat transfer requires a temperature difference between the objects involved. Heat transfer cannot occur in the absence of a temperature gradient. Understanding heat transport at its most fundamental level is the primary goal of this research. Heat transfer involves both a change in temperature and the transmission of thermal energy; the latter can be calculated using the specific heat formula, which is:

$$Q = mC_p\Delta T \quad (2.1)$$

Where:

$Q$  = heat capacity (Joules, J)

$m$  = mass of substance (kg)

$C_p$  = specific heat (J/Kg.K)

$\Delta T$  = temperature difference ( $^{\circ}\text{C}$ )

There are three modes in which heat can be transferred: conduction, convection, and radiation. Without the actual motion of the molecules in the body, heat can be transmitted from a warmer region to a cooler region by a process known as "conduction." The vibrational motion of molecules is responsible for the transfer of heat from one to another. Conduction relies on physical touch to transfer thermal energy. The most effective materials for conduction are those with close-packed, simple molecules, whether they be solids, liquids, or gases. Metal, for instance, is superior to wood or plastic as a conductor. Below is an equation that can be used to determine the rate of heat conduction:

$$Q_{cond} = KA \frac{\Delta T}{\Delta x} \quad (2.2)$$

Where:

$Q_{cond}$  = rate of heat conduction, Watt/s

$k$  = thermal conductivity, W/Mk

$A$  = cross sectional area,  $m^2$

$\Delta T$  = temperature difference, L

$\Delta x$  = thickness, m

Convection heat transfer, on the other hand, involves the transport of heat through a fluid, such as water or air. Through the medium of liquids and gases, heat is transferred from hotter to colder areas. A current is the term used to describe the flow of a large body of hot air or water. The mass transfer or molecular motion that contributes to convection heat

transmission Natural convection occurs when density changes due to temperature alone generate currents in the fluid. When the convection currents are caused by an external component such as a pump or fan, the process is referred to as forced convection. Convection heat transfer can be seen in action when milk is heated in a pan. The formula for determining the convective heat transfer rate is:

$$Q_{conv} = hA (T_S - T_{\infty}) \quad (2.3)$$

Where:

$Q_{conv}$  = rate of heat convection, Watt/s

$h$  = convection heat transfer coefficient,  $W/m^2, ^\circ C$

$A_S$  = surface area where heat transfer takes place,  $m^2$

$T_S$  = surface temperature, K

$T_{\infty}$  = ambient temperature, K

Both conduction and convection involve the movement of heat via a medium, which can be solid or fluid, respectively. However, this does not hold true for radiative heat transfer. Heat can be transported from one body to another through radiation without the medium's molecules being involved. One real-world example of the effect of electromagnetic waves, particularly infrared radiation, is the warming sensation one has when standing in the sun. For instance, microwaves heat their contents immediately without using any kind of heating medium. To determine the thermal energy released as radiation, use the following formula:

$$Q_{rad} = \varepsilon \sigma A S (T_S^4 - T_{surr}^4) \quad (2.4)$$

Where:

$Q_{rad}$  = rate of heat radiation, Watt/s

$\varepsilon$  = emissivity

$\sigma$  = Stefan-Boltzmann constant,  $5.67 \times 10^{-8} W/m^2 K^4$

$T_S$  = absolute temperature of surroundings, K

$T_{surr}$  = absolute temperature of surrounding, K

## 2.8 Basic of thermal resistance and heat dissipation

Thermal resistance is a quantification of how difficult it is for heat to be conducted. Thermal resistance is represented as the quotient of the temperature difference between two given points by the heat flow between the two points (amount of heat flow per unit time). It is defined as the ratio of the temperature difference between the two faces of a material to the rate of heat flow per unit area. Thermal resistance determines the heat insulation property of a textile material. The higher the thermal resistance, the lower is the heat loss. This indicated that the higher the thermal resistance, the more difficult it is for heat to be conducted, and vice versa. The thermal resistance,  $R$ , is connected with the temperature difference,  $\Delta T$ , and the heat flow,  $P$ , as follows:

$$\begin{aligned} \text{Thermal resistance, } R_{th} &= \frac{T_1 - T_2}{\text{Heat flow } P} \\ &= \frac{\text{Temperature different } \Delta T}{\text{Heat flow } P} \quad [^{\circ}\text{C/W}] \end{aligned} \quad (2.5)$$

$R$  is used as the symbol for the electric resistance, while  $\theta$  is used for the thermal resistance.

Thermal conductivity is used to quantify a material's heat conduction properties in place of thermal resistance;  $R$ . "k" is the most common symbol for it, but " $\lambda$ " and " $\kappa$ " are also acceptable. That quantity's inverse is known as thermal resistivity. It is common practise to use heat sink materials with high values of thermal conductivity, while thermal insulators have low values. According to Fourier's law of thermal conduction (also known as the law of heat conduction), the rate at which heat is transported through a medium is related to the area through which the heat flows and the negative of the temperature gradient. The following equation represents this law in its differential form:

$$q = -k \cdot \nabla T \quad (2.6)$$

Where:

$\nabla T$  refers to the temperature gradient,

q denotes as the thermal flux or heat flux

k refers to the thermal conductivity of the material

Every substance has its own capacity to conduct heat. The thermal conductivity of a material is described by the following formula:

$$K = \frac{(QL)}{(A\Delta T)} \quad (2.7)$$

Where:

K is the thermal conductivity in W/m.k

Q is the amount of heat transferred through the material in Joules/second or Watts

L is the distance between the two isothermal planes

A is the area of the surface in square meters.

$\Delta T$  is the difference in temperature in Kelvin

## 2.9 Crypto Mining

A distributed network of computers running crypto code verifies and adds cryptocurrency transactions to the blockchain through "crypto mining". The legitimacy of blockchain transactions is established by bitcoin mining. Crypto mining uses hardware and software to generate a cryptographic number that matches criteria. "Bitcoin mining secures the network," says Stefan Ristic. Satoshi Nakamoto says Bitcoin mining revenues double every four years. On October 18, 2023, one bitcoin cost over \$177,500. You may just make a few pennies a day racing to get your powerful computer into the Bitcoin mining pool first. This is because Bitcoin mining is unpredictable.

Mining requires a high-quality GPU. Before adding a block of transactions to the blockchain, the GPU validates it. Mining involves powerful computers running algorithms to solve mathematical problems and earn crypto blocks for their owners. Complex algorithms are needed to validate and record cryptographic transactions on the blockchain. Cryptography uses proof-of-work consensus to add a block every 10 minutes. A stronger computational infrastructure increases the likelihood of winning blocks, which increases revenue. The network validates transactions using a computer's hash rate, which determines its Bitcoin mining potential.

Mining includes adding transactions to blockchain blocks in a complex process. All data in the block is hashed after being allocated. Miners must find a 64-digit hexadecimal. Miners conjecture a number smaller than the desired hash on their mining machines. The target hash is a hexadecimal number higher than the solved hashes. Mining operations have financial and regulatory constraints. Bitcoin mining is risky since people may spend a lot of money on GPUs and ASICs and not make a profit. The environmental impact and carbon footprint of bitcoin mining are another concern. For those running one or more application-specific integrated circuits (ASICs) 24/7, mining equipment generates a lot of thermal energy, which may raise electricity usage and utility expenses.

### **2.9.1 Crypto Exchange Platform**

The term "cryptocurrency exchange" refers to platforms that allow investors to purchase and trade Bitcoin, Ethereum, and Tether. These platforms act as e-brokerages in digital marketplaces, like mobile apps or desktop interfaces. Their clients can also choose from a variety of trading and investing tools. Crypto exchanges offer margin, loan, futures, and options trading for numerous cryptocurrencies. Crypto exchanges charge consumers

based on transaction volume or kind to meet their needs. Unlike stock or commodity markets, bitcoin trading is more expensive. To facilitate operations, cryptocurrency exchanges might be centralised, decentralised, or hybrid.

## 2.9.2 Introduction to NiceHash

NiceHash is a prominent marketplace that facilitates the connection between sellers or miners of hash power and purchasers of hash power. Hash power refers to the computing capacity of a computer or hardware device, which is utilised to execute and resolve various Proof-of-Work hashing algorithms associated with cryptocurrencies. NiceHash distinguishes itself by abstaining from providing cloud mining services to its users, thereby implying that the company does not possess or lease any mining hardware. This pertains solely to the interconnection of disparate end-users.



**Figure 2.43** Operation and services provided by NiceHash.

NiceHash provides a transparent marketplace for hashing power buyers. In this marketplace, purchasers can choose a cryptocurrency to mine, a mining pool, a price, and submit their order. The pool will send the cryptocurrency to buyers after NiceHash Miner Legacy miners finish the order. This implies that buyers do not need to conduct complex

mining operations or buy mining hardware. Miners, the sellers, are the opposite of buyers. Sellers or miners can use NiceHash Miner software or connect their mining hardware, such as ASICs or PCs, to NiceHash stratum servers to fulfil buyer orders. People's hashing power depends on their computer hardware and is directed to the mining pool they choose. The current weighted average, updated every minute, determines the Bitcoin payment for each valid share submitted. The entire process is automated and requires no technical expertise.

### **2.9.2.1 NiceHash Miner**

The NiceHash Miner (NHM) is open-source software that connects a user's local machine or mining setup to the NiceHash hash-power exchange. Users are able to rent out the platform's computational power. Bitcoins, a form of digital currency, will be exchanged as payment for the computing power provided. NiceHash Miner is a piece of mining software that combines miners developed by parties unaffiliated with NiceHash. As a result, NiceHash cannot guarantee the quality of every single piece of code in every single release. Given that NiceHash has not officially endorsed NiceHash Miner, users should proceed with caution before committing to its use. NiceHash Miner now supports the DaggerHashimoto, ETCHash, Autolykos, Ergo, KawPow, Ravencoin, Neoscrypt, KHeavyHash, Kaspa, and IronFish mining algorithms, among others.

### **2.9.2.2 Crypto Mining Algorithms**

As described in my undergraduate thesis, I need to have a deep understanding of mining algorithms in order to carry out the experiment on the heat dissipation efficiency of GPUs successfully. These algorithms serve as the foundational framework for the mining

process, enabling programmers to customise their work to accommodate specific requirements. In order to successfully mine a block on the blockchain, miners are required to solve a hash function that possesses a difficulty level that is either equal to or greater than the minimum difficulty level set by the network. Within the realm of proof-of-work cryptocurrencies, a mining algorithm refers to a prescribed set of regulations and mathematical procedures employed by miners in the course of executing the hashing process. In order to accomplish this task, miners iteratively input distinct numerical values, known as nonces, into the hash function with the objective of producing a viable solution. The possibility of achieving a mining rate of trillions of solutions (hashes) per second, sometimes represented as TH/s, is evident. However, it should be noted that this capability varies significantly depending on the specific mining algorithm employed.

Those interested in mining with software like NiceHash Miner should be aware that they can choose from several different mining algorithms. The truth is that there are a wide variety of algorithms, each with its own set of advantages. Many factors, including hardware compatibility, project security, customization, and others, contribute to the wide range of mining algorithms available. Some mining methods, for instance, are optimised for specific processors, graphics processing units, or application-specific integrated circuits. Developers can manage the network's decentralisation and security by carefully crafting mining algorithms. For instance, decentralisation is bolstered by ASIC-resistant algorithms, which stop specialised gear from taking over the mining process. Some mining algorithms are built with security in mind so that their competitors can't gain an edge over them.

However, sharing an algorithm with another project may open up new possibilities, such as merged mining. By using this method, miners on a single blockchain can efficiently mine on another network without sacrificing hashrate or efficiency. For instance, the Script algorithm is used by both Litecoin and Dogecoin. When the mining rewards are low, this is

a huge plus for the safety of both networks. The inventor of a mining algorithm can adjust it for a number of factors, including the hardware the coin will be mined with. Memory and power consumption are two aspects of mining algorithms that are frequently modified. One goal of software engineers may be to design algorithms with lower energy consumption or larger memory footprints.

### 2.9.2.3 DaggerHashimoto Mining Algorithm

Dagger-Hashimoto is the predecessor to Ethash and the Ethereum 1.0 mining algorithm. 'Ethereum 1.0' uses Proof of Work (PoW) consensus. To append blocks to the blockchain, the Proof of Work algorithm uses miners and electrical energy as labour. Ethereum 2.0, which uses Proof of Stake (PoS), is an improved version of Ethereum 1.0. This upgrade improves security, scalability, and energy efficiency. Ethereum 2.0 uses validators and Ethereum depots instead of miners and power. In contrast, the Ethash algorithm was meant to reduce computing overhead by improving Dagger-Hashimoto.

The Dagger-Hashimoto method must resist ASIC mining and verify transactions utilising lightweight client implementations. DaggerHashimoto wants to create an algorithm that distributes earnings throughout the spectrum of technology, from ASIC miners to CPUs and GPUs. Combining the Hashimoto and Dagger frameworks yields the Dagger-Hashimoto algorithm. Thaddeus Dryja's Hashimoto technique prioritises memory reads as a mining constraint. Random-access memory (RAM) is more broad than computation, making it a better alternative for method evaluation, according to Hashimoto. Computer scientist Vitalik Buterin created Dagger, a cryptography method. DAGs allow Dagger to perform memory-intensive computations and efficient validations. It is meant to replace Scrypt, although shared memory hardware acceleration has been shown to affect it.

#### **2.9.2.4 ETCHash Mining Algorithm**

Ethereum Classic uses ETCHash, a sophisticated proof-of-work algorithm. This method is distinguished by the DAG file loaded into GPU memory when a miner is begun. Every 60000 blocks, the epoch changes, increasing the DAG file by 8 MB. GPUs from Nvidia and AMD can mine Ethereum Classics. On November 28, 2020, Ethereum Classic hardforked to reduce its DAG file by two times to allow weaker GPUs to mine this technique. Ethereum Classics is an open-source, distributed cryptocurrency network based on Ethereum and smart contracts. Vitalik Buterin created Ethereum and the Ethereum Foundation in 2015. After the DAO breach split the blockchain in two in 2016, most users established Ethereum Classic to rectify the robbery and recover their money.

#### **2.9.2.5 Autolykos Mining Algorithm**

While similar to Bitcoin's Proof of Work (PoW), Autolykos differs in numerous significant ways. It's made specifically for GPU mining and is immune to ASICs and mining pools. It is memory-hard, levelling the playing field between specialised hardware (ASICs) and commodity GPUs, enabling regular people to participate in mining safely for a reward.

#### **2.9.2.6 KAWPOW Mining Algorithm**

In recognition of Ravencoin, the KAWPOW mining algorithm became widely known. In addition to Bitcoin and Ethereum, it also works with a wide variety of other cryptocurrencies and blockchain projects. KAWPOW is safe against ASICs and possible centralization. In order to prevent centralization and ASICs, the KAWPOW algorithm's developers switch between the X15 and SHA51 algorithms. When it comes to mining with

the KAWPOW algorithm, Nvidia graphics cards far outperform AMD graphics cards. For example, the hash rates of the GTX 1080Ti and RTX 2080Ti are 1.5 times greater than those of the Vega and Radeon VII.

### **2.9.2.7 Neoscript Mining Algorithm**

The Script Proof-of-Work algorithm, first revealed in June 2014, is ASIC-resistant, although its predecessor, NeoScript, was not. The Script algorithm and the password-based derivation function (KDF) were upgraded with this newer version. NeoScript was developed to enhance the Script algorithm's safety, efficiency, and cost-effectiveness. It is possible to mine NeoScript with ccMiner, NeoScript OpenCL GPU Miner, and Claymore's NeoScript AMD GPU Miner. The first three cryptocurrencies to begin using NeoScript were UFO, Feathercoin, and VIVO. To further develop the Script-based DASH cryptocurrency, VIVO implemented the NeoScript algorithm.

### **2.10 Introduction to Design Expert**

Design Expert is a software application specifically developed to facilitate the process of designing and interpreting multi-factor experiments. The act of making significant advancements to both one's product and procedure is beneficial. The objective is to conduct a comprehensive analysis of essential aspects and components, examine their interactions, and eventually determine the most favourable process settings and product recipes. An instance where Design Expert can be applied is in the field of polymer processing. In this context, the software can be utilised to facilitate the design of an experiment aimed at investigating the relationship between processing factors, such as rotor speed or ram pressure,

and the resulting variations in tensile strength. The software provides a diverse selection of designs, encompassing factorials, fractional factorials, and composite designs. The system exhibits the ability to effectively manage various process variables, such as rotor speed, as well as mixing variables, such as the resin proportion in a plastic compound.

The Design Expert software provides computer-generated D-optimal designs as an alternative when standard designs are not suitable. The software application facilitates the placement of markers and the examination of the shape of interactive two-dimensional graphs. Additionally, it enables the visualisation of the response surface from various perspectives through the utilisation of rotatable three-dimensional plots. Design Expert offers robust tools for designing experiments that are intended for research purposes. These tools are particularly useful for planning experiments involving processes, mixtures, or combinations of elements and components. In addition to enhancing data visibility, the implementation of this approach facilitates the identification of statistical significance and enables more detailed modelling of the experimental results. Additionally, it offers a means of visualising the trial outcomes, aiding in the identification of noteworthy effects. The following subtopic will go into detail on the numerous mathematical models available inside Design Expert and how they can be selected in accordance with the requirements of the experiment variables.

### **2.10.1 Introduction to Response Surface Methodology (RSM)**

Several studies lack a theoretical model for their manipulated variables or response components. Here, an empirical investigation into the connection between cause and effect is necessary. Response Surface Methodology (RSM) was created by Box and Wilson. It takes situations like the one given and empirically represents them using mathematical and

statistical methods. Specifically, the goals of RSM are the expansion of experimental knowledge and the measurement of experimental variability (pure error). The mismatch between the proposed model and the experimental data was also identified with the aid of RSM. In areas of the experimental domain where no experiments were conducted, it is also able to detect a response and make an accurate prediction. Methods for systematically testing potential solutions are proposed by RSM. By reducing ambiguity based on experimental data, RSM facilitates outlier identification and decision-making under uncertainty.

RSM utilises a diverse array of mathematical and statistical techniques to construct and employ empirical models. The objective of Response Surface Methodology (RSM) is to employ experimental design and analysis techniques in order to ascertain the correlation between a response variable and the concentrations of multiple input variables or factors that influence it. The linear modelling of two-level factorial designs results in the formation of either flat planes or twisted planes when examining interaction responses within a three-dimensional space. Two-level factorial designs can be considered a sequence of repeated screening procedures that aim to identify the most significant inputs for a given project.

Nevertheless, it is not uncommon to encounter response surfaces that exhibit a significant degree of curvature. In these instances, the use of Response Surface Methodology (RSM) may be deemed the most suitable course of action. The Response Surface Methodology (RSM) incorporates the consideration of a response that fulfils a bounding condition of either a maximum or minimum value. Factorial designs and analysis of variance (ANOVA) are commonly employed in statistical modelling to effectively capture the response. However, it is important to note that these methods do not provide the means to incorporate additional modelling of the effects. RSM primarily emphasises the utilisation of screening and three-level factorial studies as prominent types of factorial studies. Additional

treatments are incorporated to specifically target the desired outcomes and enhance the accuracy of the model as a predictor.

### **2.10.2 Introduction to Factorial Design**

There is a type of statistical experiment design called the factorial design that allows someone to look at how different independent variables (also called factors) affect a dependent variable. This methodology enables researchers to examine the primary and interactive effects of multiple independent variables on a single dependent variable. Factorial designs are types of experiments that look at all the possible levels that can be combined across multiple independent variables. This creates all the possible permutations. Through the manipulation of various characteristics and the measurement of the dependent variable, researchers are able to enhance their understanding of the individual contributions of each factor as well as their combined or interactive effects.

According to the study conducted by Kerlinger and Lee (2000), there was a significant shift in the approach of social scientists towards formulating research questions and generating objective results when employing factorial designs in behavioural research. The utilisation of factorial design in experimental design enables the examination of multiple variables simultaneously. These mechanisms facilitate the establishment of relationships between various factors. This instrument can be used by researchers to examine potential associations between the influences of factors and concentrations. This may potentially unveil captivating mechanisms. This phenomenon enhances the observed effects and facilitates the identification of moderators or mediators in associations between variables.

Experiments employing factorial designs are widely used and renowned for their reliability. The application of analysis of variance (ANOVA) and the seminal research

conducted by Ronald A. Fisher have proven to be influential in the field. This tool enables researchers to conduct experiments in a controlled setting, allowing them to examine the impact of various variables on the final outcome without any potential risks or hazards. Modifying the levels of elements enables researchers to observe the individual contributions of each component as well as any potential interactive effects. By utilising this knowledge, it becomes possible to customise treatments and interventions for a specific population.

A 2x2 factorial design examines the effects of two factors, each with two levels. Similarly, a 3x3 factorial design investigates the effects of three independent variables, each with three levels. Likewise, a 4x4 factorial design explores the effects of four factors, each with four levels, and so forth. The utilisation of a  $2 \times 2$  factorial design is a prevalent approach in psychological research for investigating the impact of two factors on behaviour or outcomes. Medical research frequently necessitates the exploration of numerous variables, thus rendering a 3x3 factorial design a valuable tool.

### 2.10.3 Introduction to Mixture Design

In the context of experimental design, a mixture is operationally defined as a substance resulting from the combination of two or more constituents. Mixture designs, a type of response surface experiments, depend on many factors and how much of each one there is. The proportions of all components from each experiment are aggregated. In the majority of experiments, the sum of the component proportions is equal to 1. The increased complexity resulting from this has rendered mixture experiment design and analysis more intricate; however, it enables a more precise estimation of the effects of components on the response variable. Mixture design is a methodology used to ascertain the optimal proportions of ingredients in order to attain a desired outcome.

Researchers have the ability to examine the impact of various combinations of components on a response variable through the use of a mixture design. Researchers have the capacity to investigate the primary impacts, interactions, and non-linear effects of the mixture across various concentrations. The simplex lattice, centroid, axial, and extreme vertex are the four most frequently encountered mixture designs. The simplex lattice design is capable of characterising the response surfaces of multiple components through the use of a polynomial equation of order 2 or greater. The design criteria exhibit uniformity across the simplex. In addition, the simplex centroid design can be employed to accomplish the same objective as the simplex lattice design or to discern the numerous constituents of larger ones. The simplex centroid design exclusively incorporates centroid points.

In different situations, the simplex axial design is used to selectively remove important parts from complex mixtures. The simplex axial design is characterised by the presence of points located within the simplex, in contrast to the simplex lattice and centroid designs, where all points, except for the centroid, are situated on the boundaries of the simplex. Extreme vertex design is a methodology employed for the purpose of handling constrained mixture components or linearly constrained components. The feasible region of the factor space is determined by the strict constraints imposed on vertex design, with the initialization parameters serving as the boundary points.

There is a common confusion among Design of Experiment (DOE) experts regarding the distinction between a mixture DOE and a factorial or response surface methodology (RSM) DOE during the formulation process. This phenomenon has the potential to yield inaccurate outcomes. The design of experiments (DOEs) involving response surface methodology (RSM) and factorial designs is characterised by their independence, whereas DOEs related to formulation and mixture designs incorporate the consideration of

ingredients. The factorial levels in the design of experiments (DOE) will be replaced with ratios of ingredients in the mixture.

#### **2.10.4 Introduction to Combined Design**

The Design Expert provided designs that incorporated both mixture components and process factors. Combination and split designs are commonly employed in experimental design to investigate multiple independent variables concurrently. The researcher observes a range of distinct levels for the independent variable, although they are not identical. The researchers systematically analyse all potential combinations of factors. This method can be employed by researchers to examine the individual and collective impacts of each permutation.

In order to assess individuals' preferences for colour and shape, a combination design would be employed wherein all conceivable combinations of colours and shapes would be presented (e.g., red circles, blue squares, green triangles, etc.). In a combination design study, participants serve as their own controls across all conditions, thereby obviating the necessity for a control group and yielding direct insights into interactions among independent variables. The integration of design elements has the potential to extend the duration of a project and impose additional strain on individuals involved in its execution. Furthermore, the presence of numerous permutations may render the task infeasible.

The primary objective of this project is to address the existing knowledge gaps pertaining to contemporary thermal management systems employed in Graphics Processing Units (GPUs). In this study, we aim to evaluate the efficacy of the ASUS TUF Gaming 3060 OC Edition GPU through the manipulation of fan speed. Our analysis will involve a

comparison of the obtained results with the default power limit, clock setting, and memory clock frequency of the mining chamber. The literature review examined deficiencies in the field of mining, including mining practices, mining software, mining algorithms, and the utilisation of design expert software for optimal model selection. The objective of this study is to examine the optimality of fan speed through the application of response surface methodology (RSM). In the subsequent analysis, a comparative assessment is conducted between nickel and copper memory heatsinks in order to ascertain the influence of material composition on the thermal dissipation of GPU memory. By pursuing these objectives, the investigation of thermal resistance, conductivity, and dissipation can be conducted in order to empirically ascertain thermal dissipation.



## CHAPTER 3

### METHODOLOGY

#### 3.0 Introduction

This chapter covers the steps taken throughout the project to obtain and validate the optimised fan speed for GPU mining proposed via Response Surface Methodology (RSM) by means of the Design Expert programme. The ASUS TUF Gaming 3060 OC Edition was the GPU of choice for this mining rig. The effectiveness of a nickel and copper heatsink radiator in decreasing the temperature of the GPU memory was tested as part of an ongoing research investigation on thermal management for mining GPUs. There is little room for error and no need to start over because everything has been meticulously planned. This is a crucial stage because it describes the workflow and project routines that were used to carry out the experimental part of the project. A condensed version of the methodology used throughout the study is shown in Figure 3.2.

#### 3.1 Literature Review

The first step is to conduct a literature review. Learning the fundamentals of how GPUs work and the criteria for achieving optimal thermal performance and thermal dissipation rate is the first step in building a library. Thermoelectric cooler (TEC), water-cooled heat sink, finned water-cooled radiator, and heat transfer mode are all relevant search terms for a literature review on axial fans. In order to determine the best fan speed to use in

order to achieve the most desirable GPU core and memory temperatures, the relevant literature is reviewed. Various methods, including response surface modelling (RSM), factorial design, mixture design, and combined design, have been studied in order to establish which is best for determining the optimal fan speed. Copper and nickel were used in these studies to better understand how different material properties affect the thermal performance of GPU miners.

This preliminary step is very helpful for the experimental stage of this project. PSM II's experimental components required extensive background reading from a wide range of sources in order to be carried out successfully. The data collected emphasises the significance of understanding the concept of heat transfer, including the modes of heat transfer and thermal properties, as well as the GPU's components, the most heat-generating components within a GPU, and the methods for optimising a GPU's cooling system to achieve lower temperatures in a working GPU system without compromising GPU computing performance. Having a solid understanding of the fundamentals and context will make the experimentation part of the research a breeze.

UNIVERSITI TEKNIKAL MALAYSIA MELAKA

### 3.2 General Methodology of PSM

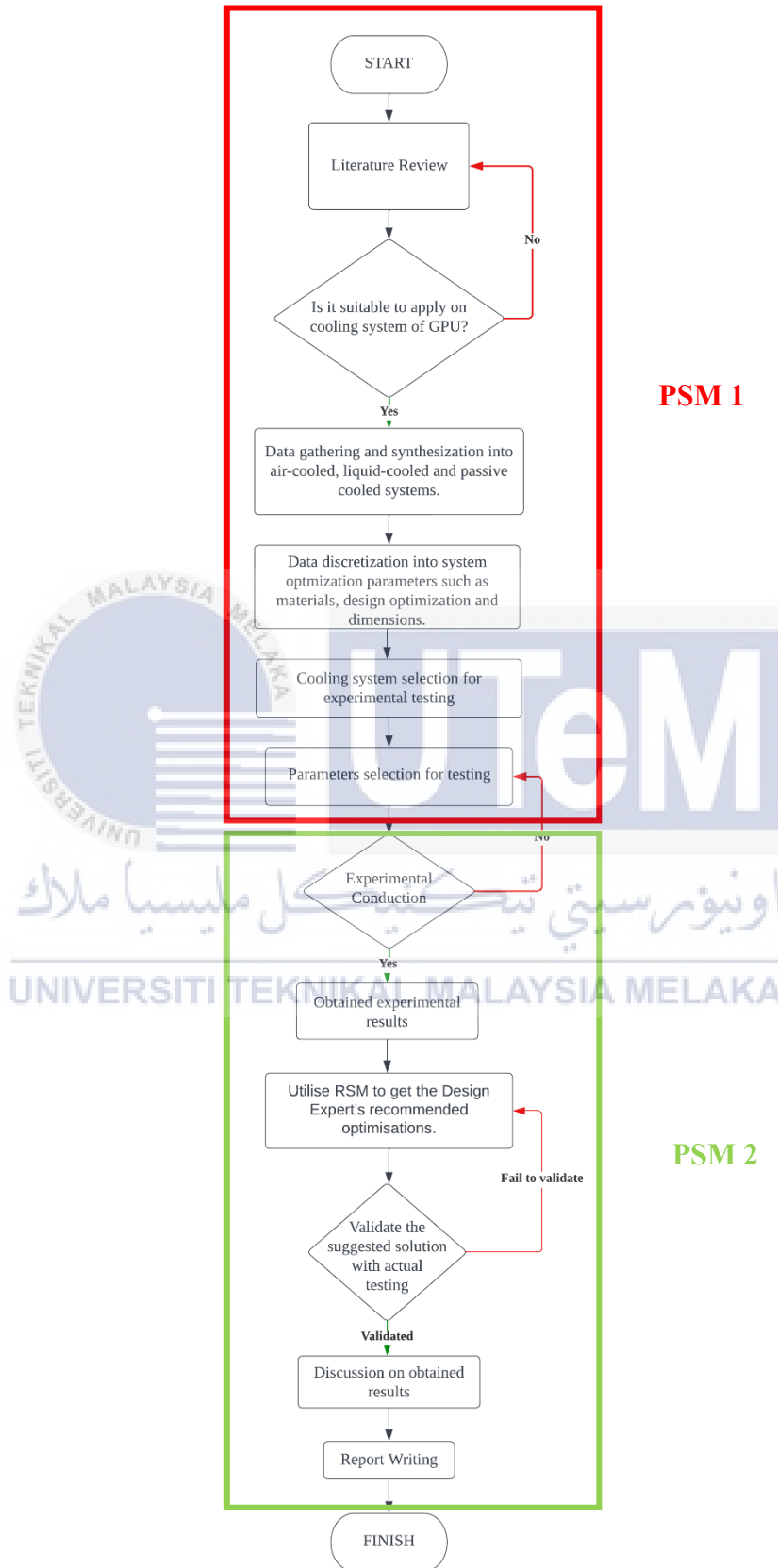


Figure 3.1 General Methodology of PSM.

The overall methodology for the PSM project is shown in Figure 3.1. The flow diagram shows that the first part of this research was a literature review, which meant reading and understanding all the previous research on GPU thermal management. Assessing the method's appropriateness for application on GPUs was the subsequent step following the completion of the literature review. After that, the next step is to gather data and sort it by cooling method: air, liquid, or passively through a heat sink. Afterwards, the data will be further discretized based on the optimisation parameters, which might encompass dimensions, materials, or design optimisation. The only remaining steps for PSM I are to select a cooling system and test parameters for this project.

Employing experimental conduction, PSM II would determine the effects of fan speed on GPU core and memory temperature. By incorporating RSM (Response Surface Methodology), Design Expert software would facilitate the Design of Experiments (DOE). To achieve the optimisation solution recommended by the Design Expert, the experimental test on fan speed will be carried out again. A second round of experimental testing would confirm and validate the optimisations. Immediately following that, the validated optimisation solution for fan speed will be discussed and written in the report in order to complete this project.

### **3.3 Initial stages of setting up the experiment**

Before conducting the experiment, it is imperative to undertake the necessary research during the preliminary phase of the investigation. For instance, the methodologies employed for GPU loading. In this study, mining was employed as the workload to evaluate the thermal performance of the GPU fan speed. In order to ensure its efficacy within this particular context, thorough preliminary research should be conducted on the mining

algorithm, mining platform, and mining method selected. In this particular scenario, the utilisation of the NiceHash mining platform and the Dagger Hashimoto mining algorithms will be implemented. Utilising the default settings of the GPU for mining operations may result in excessive heat generation, thereby necessitating a thorough examination of the mining settings. This finding is in accordance with the research conducted by Chamber (2022).

Consequently, the technique employed to regulate and track the temperature of the GPU's core and memory was critical, as these experimental outcomes would be utilised in the DOE to gather optimisation data. Therefore, in order to collect the experimental data, it is required to utilise the software that controls the clock setting of the GPU as well as the software that monitors the temperature. For this case, we use HWINFO64 and MSI Afterburner. Also, since Nvidia kept the hash rate of their RTX series graphics cards low to keep their products affordable for gamers, research on the best graphics drivers to use is necessary to unleash full mining performance. According to the research, the 512.15 driver is required on Windows in order to unlock the full mining potential of Nvidia RTX series graphics cards based on the work of Smith (2022).

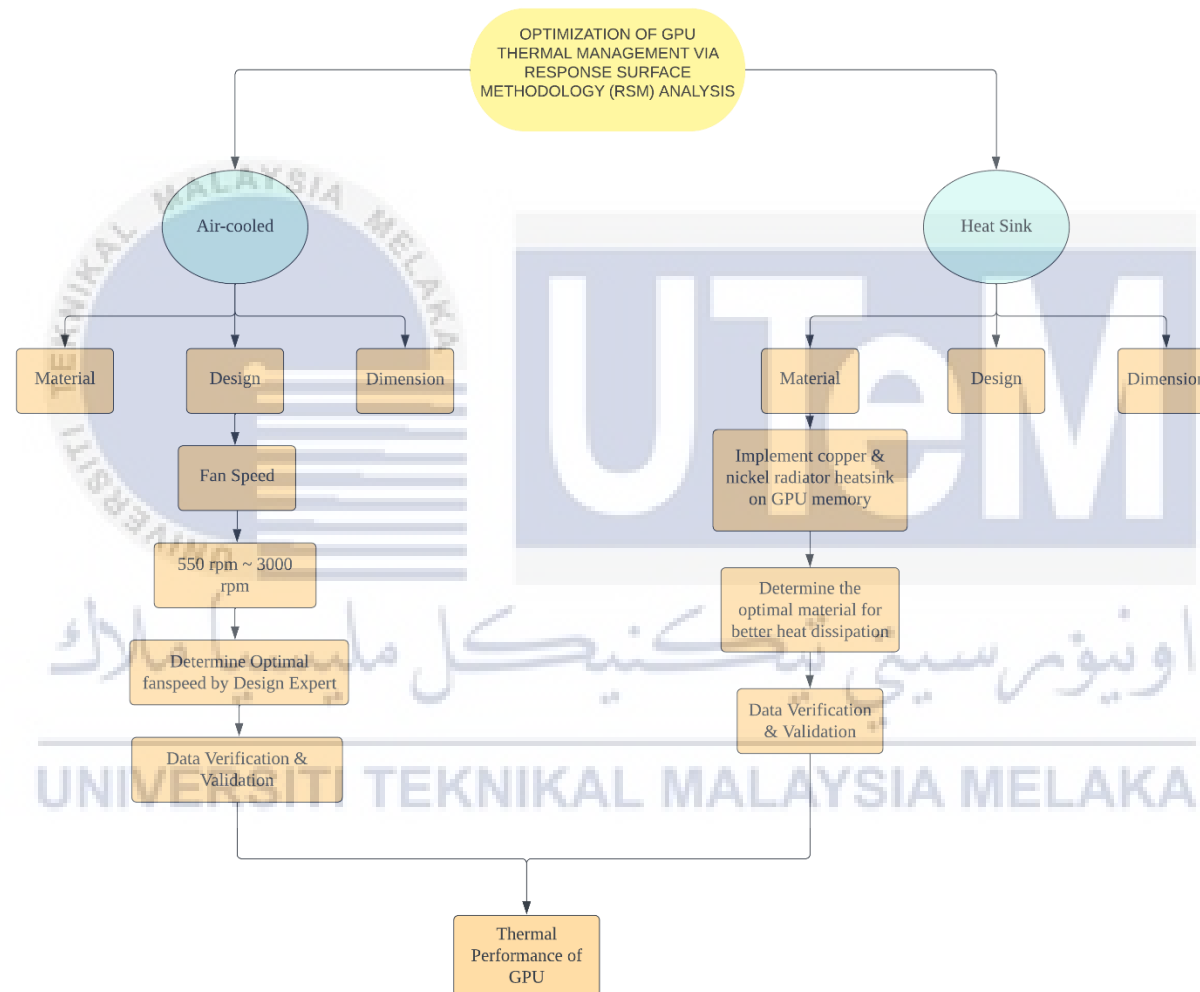


**Figure 3.2** Graphics processing unit (GPU) fan speed and radiator heatsink material experiment flowchart

### 3.4 Graphic Processing Unit (GPUs) selection

It is widely believed that selecting the optimal GPU is pivotal to achieving success. An air-cooled GPU is selected for this project. All of the required tools and space must be available at the UTeM laboratory in order to make this happen. Both Nvidia and AMD, two of the biggest manufacturers, make a vast range of different GPU types. Both of these market giants create GPUs, each with its own distinctive design and set of advantages and disadvantages. Since Nvidia GPUs can be found in the UTeM lab, they are the primary focus of our investigation. Since Nvidia GPU makers included more potent "Ti" versions of their RTX 30 series family, the RTX 30 Ti is a potent yes worth considering. Notable examples are the Geforce RTX 3090 Ti and Geforce RTX 3080 Ti, both of which are simply more powerful and expensive variants of the corresponding non-Ti GPUs. Therefore, the following suggestions are still generally applicable.

Here is some terminology that needs clarifying for readers' better comprehension before going deeper into the specification's comparison between the RTX 30 series family of GPUs. To begin, a GPU's parallel data processing units are known as Nvidia CUDA cores. They function much like a computer's central processing unit. The greater the number of CUDA cores in a GPU, the more complicated data it can process rapidly. Meanwhile, boost clock is the highest speed a GPU can run at with sufficient power and temperature. While there is a basic clock statistic, gamers should be aware that Nvidia graphics processing units (GPUs) consume significantly more system resources than average when playing games. There are many other elements, such as the PC's hardware, that affect performance, so don't assume that a higher Boost Clock speed automatically means better performance. There is a fine line between the various types of GPU memory. For instance, GDDR6X memory can handle more demanding games at higher settings since it has more bandwidth than GDDR6 memory. The maximum amount of electricity that a graphics processing unit (GPU) can

consume when it is fully loaded is known as its power drawn. Below is a table that compares the specifications of different RTX 30 series GPUs:



**Table 3.1** Specifications comparison between RTX 30 series GPU (Honorof & Moore-Colyer, 2023)

|                     | Nvidia Geforce RTX 3060   | Nvidia Geforce RTX 3060 Ti  | Nvidia Geforce RTX 3070   | Nvidia Geforce RTX 3080   | Nvidia Geforce RTX 3090   |
|---------------------|---|---|---|---|---|
| Specifications      |  |  |  |  |  |
| Nvidia CUDA Cores   | 3584  | 4864  | 5888  | 8704  | 10496   |
| Boost Clock (GHz)   | 1.78  | 1.67  | 1.73  | 1.71  | 1.7   |
| Memory Size (Gb)    | 12  | 8   | 8   | 10  | 24  |
| Memory Type         | GDDR6   | GDDR6   | GDDR6   | GDDR6X  | GDDR6X  |
| Dimensions (inches) | 9.5 × 4.4   | 9.5 × 4.4   | 9.5 × 4.4   | 11.2 × 4.4  | 12.3 × 5.4  |
| Power Draw (W)      | 170   | 200   | 220   | 320   | 350   |

The specifications of each GPU in the RTX 30 series family were compared in Table 3.1. The RTX 3080 shares the most similarities with the RTX 3090 with regard to boost clock and memory type, as can be seen from the information provided above. Hence, the RTX 3080 is the way to go when checking its thermal performance with various fan speeds and heat sink memory radiator materials. It would be ridiculous not to get an RTX 3080 when looking for a top-tier gaming rig. It has a lot of advantages over cheaper GPUs, such as GDDR6X memory and around 9000 CUDA cores. The large size and high power consumption of the card would make the thermal performance metrics more noticeable. The project supervisor suggested the ASUS TUF Gaming 3060 as the best GPU for testing due to its adaptability and the fact that it is smaller and less demanding on electricity than the RTX3080, making it easier to set up.

### 3.4.1 Specifications pertaining to the ASUS TUF Gaming 3060

The final testing GPU chosen for undergoing testing was ASUS TUF GAMING 3060. The figure below shown the physical appearance of the GPU.



**Figure 3.3** Physical appearance of ASUS TUF GAMING 3060 (ASUS TUF RTX 3060 GAMING Specs, n.d.)

**Table 3.2** Specifications of ASUS TUF GAMING 3060 (Specification Sheet (Buy Online), 2023)

|                                  |                                    |
|----------------------------------|------------------------------------|
| <b>Graphic Engine</b>            | NVIDIA Geforce RTX 3060            |
| <b>Bus Standard</b>              | PCI Express 4.0                    |
| <b>OpenGL</b>                    | OpenGL 4.6                         |
| <b>Video Memory</b>              | 8 GB GDDR6                         |
| <b>Memory Interface</b>          | 192-bit                            |
| <b>Resolution</b>                | Digital Max Resolution 7680 × 4320 |
| <b>Interface</b>                 | Native HDMI 2.1 × 2                |
|                                  | Native DisplayPort 1.4a × 3        |
|                                  | HDCP Support                       |
| <b>Maximum Display Support</b>   | 4                                  |
| <b>Nvlink/ Crossfire Support</b> | No                                 |
| <b>Dimensions (inches)</b>       | 11.81 × 5.63 × 2.13                |
| <b>Recommended PSU (W)</b>       | 750                                |
| <b>Power Connectors</b>          | 1 × 8-pin                          |
| <b>Slot</b>                      | 2.7 slot                           |

### 3.4.2 ASUS TUF GAMING 3060 GPU Mining Setting

As previously mentioned, conducting tests on the heat dissipation performance of a GPU through mining while utilising the default settings would result in excessive heat generation and potential overheating of the GPU. In this particular context, it was imperative to establish an optimal mining configuration for the RTX 3060 in order to ensure the seamless execution of the test while mitigating the risk of GPU overheating and potential consequential harm to the electrical module. The mining algorithm employed in our study was DaggerHashimoto, which is commonly used for mining ETChash. According to

Chamber (2022), the recommended mining configuration for the RTX 3060 is presented in the table below:

**Table 3.3** RTX 3060 ETChash Mining Overclocks setting (Chamber, 2022)

| PARAMETER               | DESCRIPTION                   |
|-------------------------|-------------------------------|
| Expected Mining Results | 50 MH/s [31.5 MH/S (Stock)]   |
| Power Consumption       | 115 Watts [140 Watts (Stock)] |
| Core Voltage (VDD)      | N/A                           |
| Power Limit             | 120 Watts or 70%              |
| Core Clock (CCLOCK)     | Absolute: 0 or Offset: 0      |
| Memory Clock (MCLOCK)   | Absolute: 0 or Offset: +1400  |
| Memory Voltage          | N/A                           |
| Fan Speed (%)           | 70% ± based on your temps     |

MSI Afterburner was used to control the power limit, core clock, memory clock, and fan speed to set the GPU setting, according to Chamber (2022). To verify that the device manager detected the RTX 3060 graphic driver, we clicked on the display adaptor before applying the mining setting. Figure below shows MSI Afterburner settings for the ASUS TUF Gaming 3060 GPU:

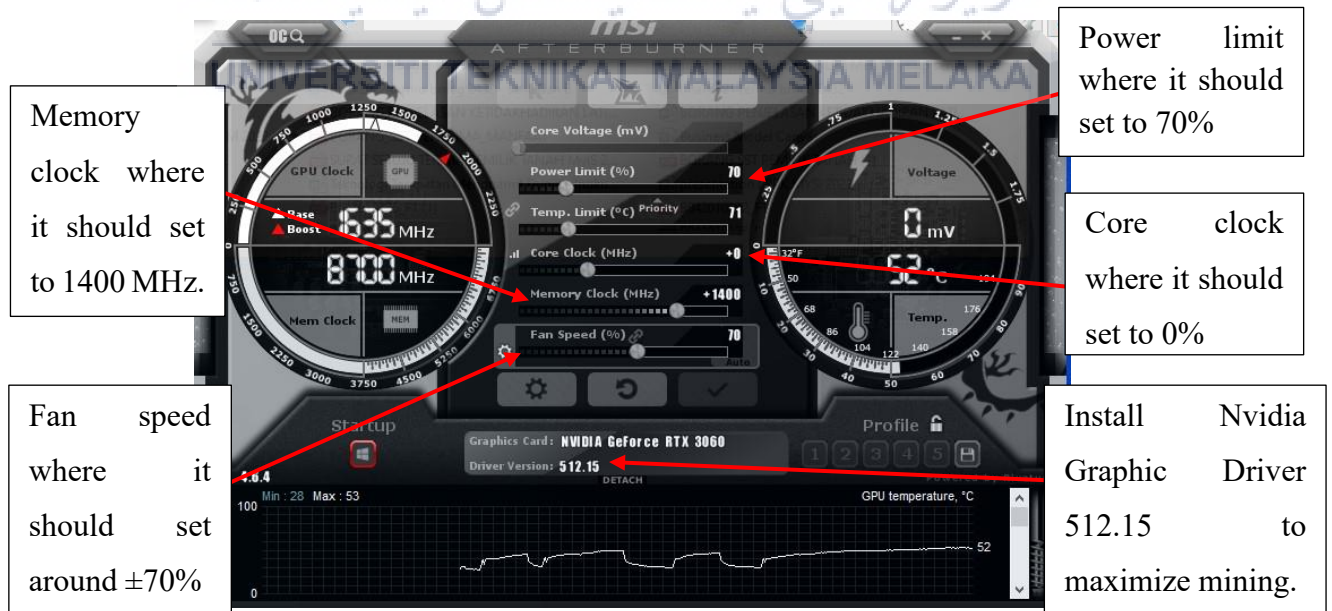


**Figure 3.4** GPU Mining Setting through MSI Afterburner

### 3.4.3 Setup of the Nicehash miner prior to testing

To induce a workload on the ASUS TUG Gaming 3060 GPU for the purpose of examining its core and memory temperatures, the Nicehash miner software was employed. Prior to initiating the Nicehash miner software, it is imperative to access the MSI Afterburner application in order to configure the GPU clock settings, as depicted in Figure 3.4. Subsequently, proceed to launch the HWINFO 64 software in order to monitor the temperature of the GPU core and memory, as depicted in the accompanying figure.

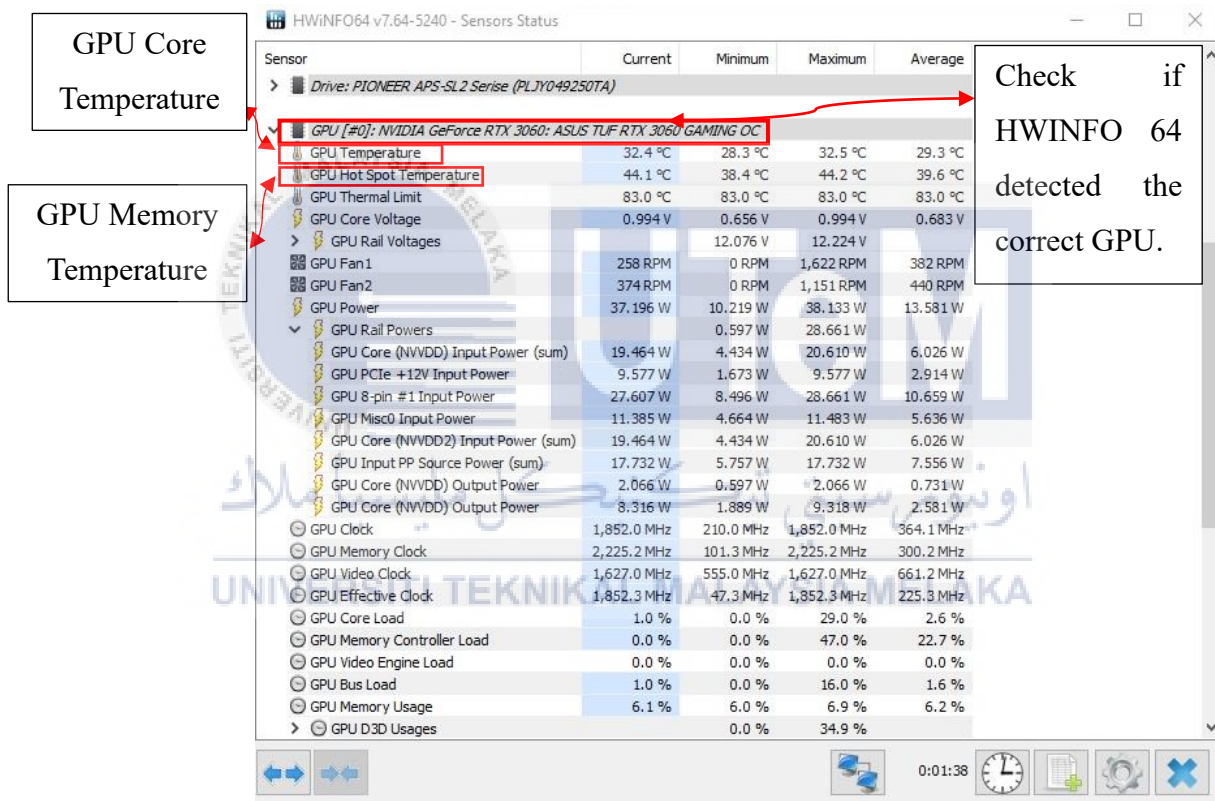


Figure 3.5 Initial GPU core and memory temperature checks.

Once the appropriate GPU model and the initial GPU core and memory temperature have been verified, the Nicehash miner application can be launched to commence the initial mining process. Within the programme interface, it was imperative to select the Dagger-Hashimoto algorithms, as our sole emphasis is placed on these specific mining algorithms. Upon initiating the mining process by clicking the "start mining" button, it became

imperative to commence monitoring the temperature curve, which is observable through the HWINFO 64 and MSI Afterburner software applications. The monitoring of GPU core and memory temperature can be achieved through the use of HWINFO 64, as depicted in the figure presented below.

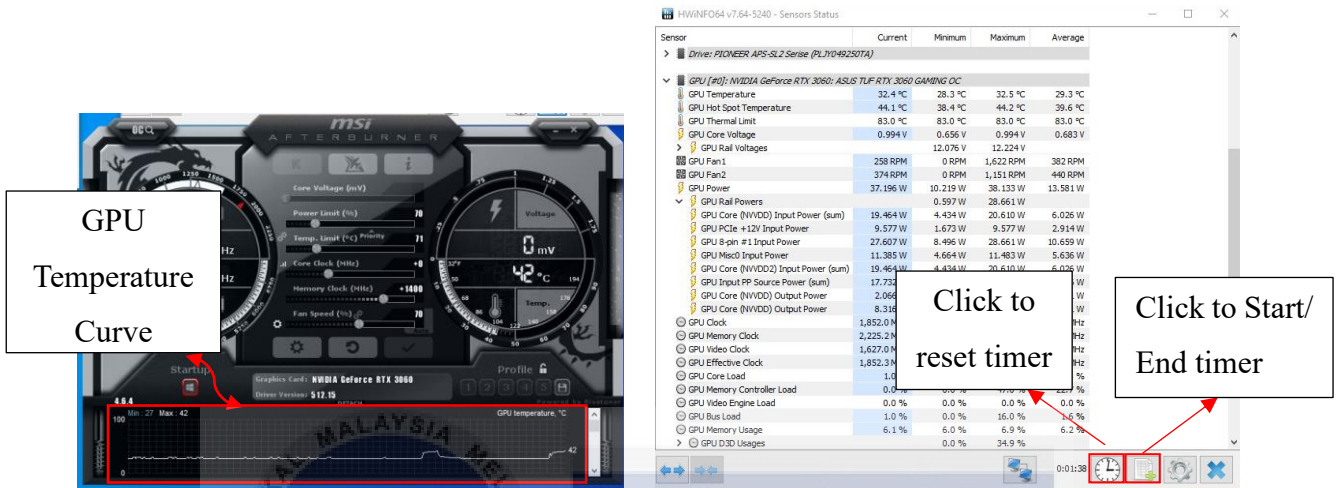


Figure 3.6 Method to log GPU temperature before and after the test.

### 3.5 Variable fan speed impact upon GPU temperature under identical GPU load and RSM Analysis optimal fan speed prediction validation

In the experiment that examined the effect of varying fan speeds on GPU temperatures under identical GPU load conditions, an ASUS TUF Gaming 3060 was used. The experimental data shows that the fan speed ranges from 550 rpm all the way up to 3000 rpm. The rationale for this was that it is acceptable for a graphics card to function properly while maintaining a temperature of 85 degrees Celsius or lower. To illustrate the point, all series of Nvidia graphic cards—which are now the most popular GPUs on the market—have the same maximum temperature report of 93 degrees Celsius. The 30 series cards are the sole exception; they can only withstand temperatures up to 92 degrees Celsius. Sarnick (2022) Additionally, the manufacturer of the graphics card had already configured MSI Afterburner,

forbidding users to adjust the fan speed lower than 550 rpm in order to prevent damage to their machines, so the least controllable fan speed was 40% of the total fan speed, which was approximately 550 rpm. Next, we went for 3000 rpm, as this was the highest fan speed that an ASUS TUG Gaming 3060 could handle.

Turning to the Design Expert software, reducing the total number of RSM experiment will aids in identifying the ideal input variables, considering the desired response outcomes and the values attained via the use of experimental techniques.

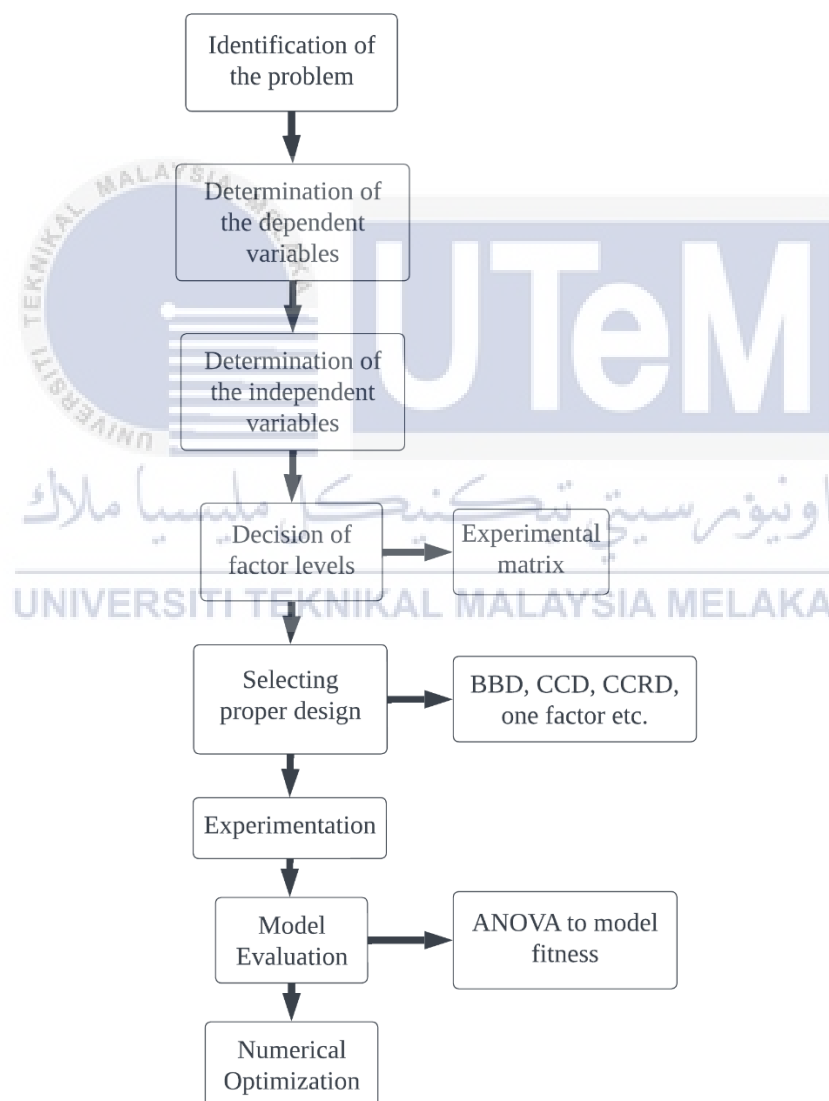
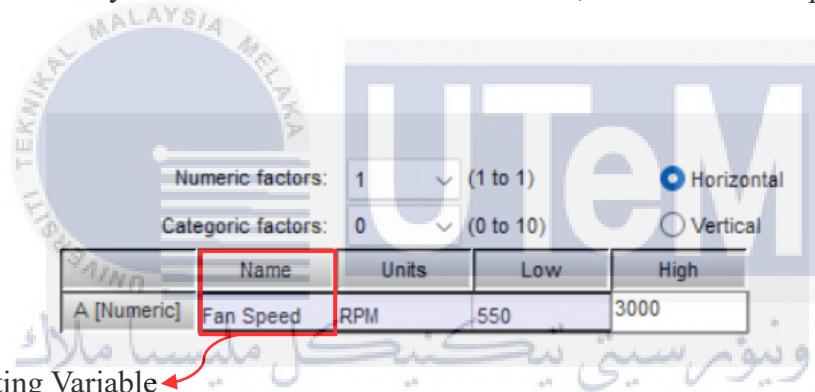


**Figure 3.7** RSM sequence for the GPU fan speed optimization. (Elumalai & Ravi, 2023)

The application sequence of RSM is shown in Figure 3.6. The investigation should begin with the establishment of the input variables' values, including their minimum and maximum values. As a result of the study, the specified response parameters are used to conduct the tests using the required data measurements. Once the dependent and independent variables have been determined, an RSM strategy may be devised, and experimental data sets can be created. Once everything is in order, the built experimental sets can be run using the specified input settings. In this research of GPU fan speed optimization, we used the response surface methodology (RSM) and selected the one factor to adjust the fan speed from 550 rpm to 3000 rpm. Since our testing only included one influencing variable—fan speed—we decided to concentrate on only one factor. In the illustration below, we can see the input of the single factor:



Manipulating Variable

**Figure 3.8** Single-factor RSM input for 550–3000 rpm fan speed.

A quadratic model was selected for the modelling because it was necessary to execute the experiment seven times. It turned out that the main difference between the cubic, linear, and quadratic designs was how well they estimated terms with more complex structures. When it comes to the quadratic model, the majority of the designs are sufficient. Therefore, a quadratic model was used for the design, and the table below shows the necessary variations in fan speed that were needed to carry out.

**Table 3.4** Completed RSM fan speed optimisation experiment design.

| Std. run no. | Run | Factor          | Response                |                           |
|--------------|-----|-----------------|-------------------------|---------------------------|
|              |     | Fan Speed (RPM) | GPU Core Temperature °C | GPU Memory Temperature °C |
| 5            | 1   | 3000            |                         |                           |
| 2            | 2   | 550             |                         |                           |
| 1            | 3   | 550             |                         |                           |
| 4            | 4   | 2387.5          |                         |                           |
| 6            | 5   | 3000            |                         |                           |
| 7            | 6   | 1775            |                         |                           |
| 3            | 7   | 1162.5          |                         |                           |

The seven required runs for conducting RSM analysis using the one-factor method are shown in Table 3.4. For the sake of minimising experimental error, the running order must adhere to the normal run number. Once the 7th run was finished, the optimisation and RSM ANOVA results could be acquired using the Design Expert 10 software.

### 3.6 Variable material of thermal pad on thermal dissipation performance of GPU memory by utilizing RSM analysis

The experiment aimed to investigate the impact of different thermal pad materials on the thermal performance of GPU memory. Specifically, nickel and copper thermal pads were utilised as replacements for the original thermal pads provided by ASUS TUG Gaming 3060 manufacturers. To conduct the test, the GPU was disassembled to perform the thermal pad replacement procedure. The disassembled GPU would thereafter employ isopropyl alcohol to eliminate any remnants of thermal grease on the GPU core and remove the thermal pad on the GPU memory. The disassembled GPU is depicted in the diagram below.

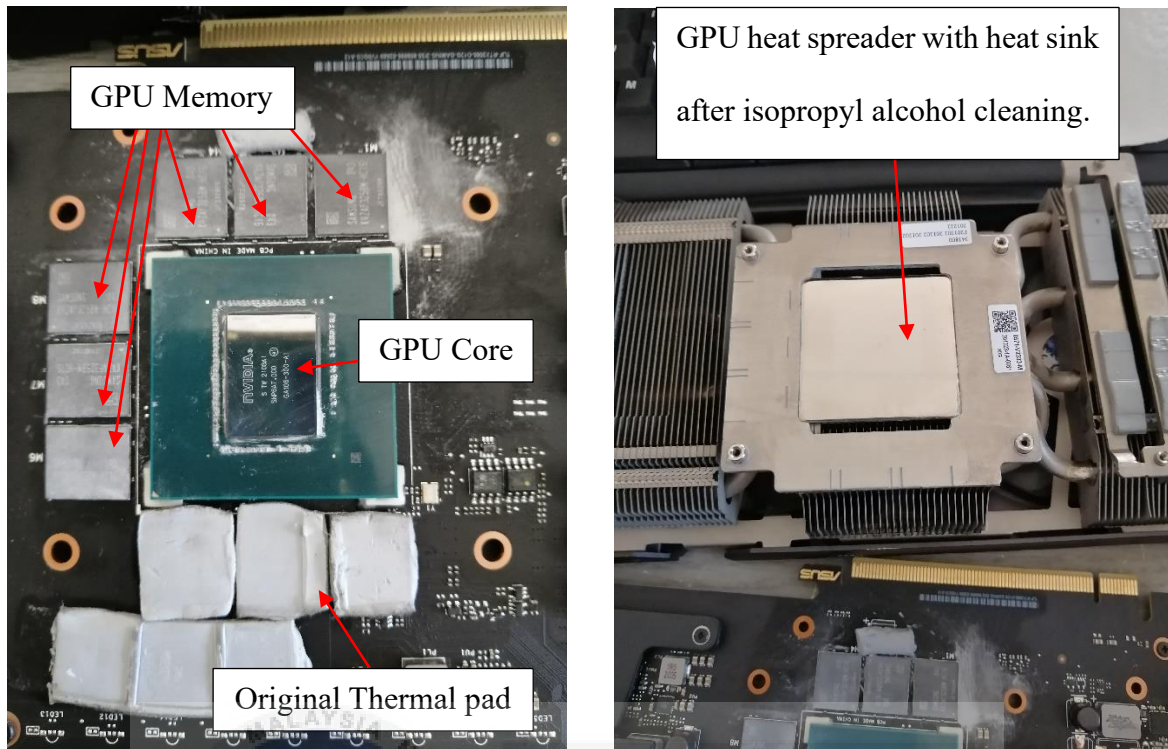


**Figure 3.9** The disassembled ASUS TUG GAMING 3060

It would then substitute the original thermal pad with a copper and nickel version. The detail specification of original thermal pad against nickel and copper thermal pad were shown in table below:

**Table 3.5** Detail Specification of original, nickel and copper thermal pad (“Thermal Conductivity Experiments – Resistance: Materials,” 2021)

| Properties                   | Types of Thermal Pad |        |               |
|------------------------------|----------------------|--------|---------------|
|                              | Arctic TP-3 (Stock)  | Nickel | Copper        |
| Tensile Strength (psi)       | 13.7                 | 8560   | 32000         |
| Thermal Conductivity (W/ mk) | 1 ~ 7                | 87.86  | 397.48        |
| Thermal Resistance (°C/W)    | 0.1540               | 0.0042 | 0.0010        |
| Colour                       | Grey                 | Silver | Reddish Brown |

Prior to applying the nickel thermal pad, it was essential to shield the PCB board with Kapton tape in order to insulate the conductive area and prevent any contact between the nickel thermal pad and the risk of an electrical short circuit.

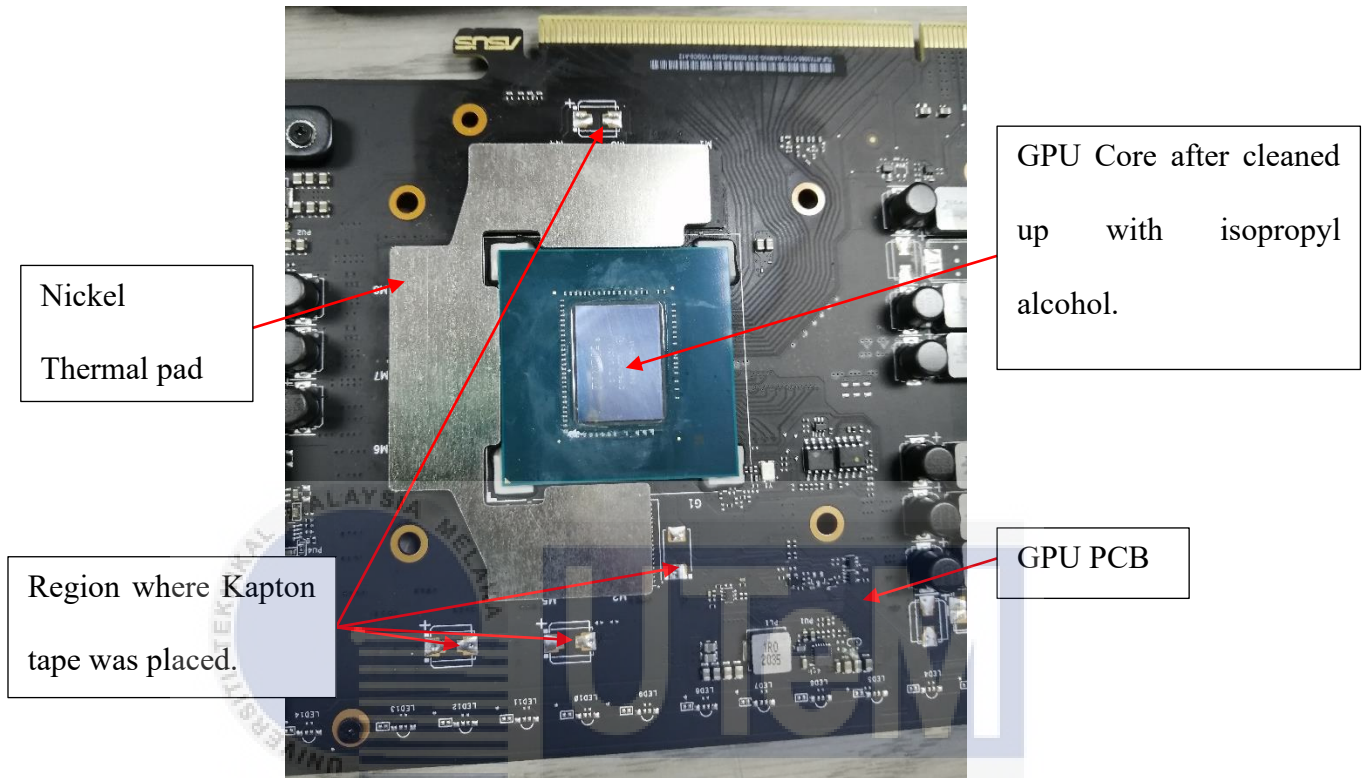


Figure 3.10 Placement location of nickel thermal pad on GPU PCB.

Following the placement of the Kapton material and nickel thermal pad on top of the GPU memory, a thermal paste was applied to enhance the thermal connection between the nickel thermal pad, the GPU memory chip, and the heat spreader of the GPU heat sink. The thermal paste employed must exhibit non-conductive properties to prevent electrical short circuits on the GPU component in the event that the thermal pad becomes misaligned from its original position. The OCinside website conducted a performance comparison review of the Arctic MX4, MX5, and MX6. The researchers chose to employ Arctic MX4 due to its comparatively lower viscosity compared to MX5, which allows for easier application and better spreading over the processor or GPU surface. Meanwhile, MX4 may be easily removed from the CPU without much difficulty, as it does not adhere strongly. Furthermore,

according to the performance test results presented in the table below, the MX6 exhibits the highest level of performance, but with a marginal difference of only 0.3 °C and 0.4 °C. The venerable MX4 was in remarkably close proximity. Therefore, while comparing performance, it is reasonable to consider using an MX4 thermal grease as thermal paste for our test.

**Table 3.6** Performance Comparison between Arctic MX4, MX5 & MX6. (Arctic MX-4 Vs MX-5 Vs MX-6 Thermal Paste Review Handling and Workability, n.d.)

| Heat Transfer Paste | Coollest Core | Hottest Core |
|---------------------|---------------|--------------|
| Arctic MX-4         | 72.9°C        | 83.4°C       |
| Arctic MX-5         | 74.2°C        | 84.6°C       |
| Arctic MX-6         | 72.5°C        | 83.1°C       |

The details specifications of thermal paste Arctic MX4 was shown in table below:

**Table 3.7** General Specification of Thermal Paste Arctic MX4 (MX-4 | Premium Performance Thermal Paste | ARCTIC, n.d.)

| Properties                   | Value                    |
|------------------------------|--------------------------|
| Viscosity                    | 31600 Poise              |
| Density (g/cm <sup>3</sup> ) | 2.5                      |
| Thermal Conductivity (W/mK)  | 8.5                      |
| Volume Resistivity (Ω-cm)    | $3.8 \times 10^{13}$     |
| Colour                       | Grey                     |
| Form                         | Grease                   |
| Odour                        | None                     |
| Flash point                  | >100°C (Seta Closed Cup) |
| Explosive Properties         | No                       |
| Specific Gravity             | 4.2                      |
| Oxidizing Properties         | No                       |

According to the comparative analysis of performance, the study examined the differences between the Arctic MX4, MX5, and MX6. All three thermal pastes are electrically non-conductive and can be used at sub-zero temperatures. Although the MX6

paste managed to slightly outperform the MX-4 paste by a few tenths of a degree, the MX-4 thermal paste definitely excelled in terms of its affordability, since it is currently priced at almost half of the MX-6 paste in the open market. Therefore, MX-4 thermal paste was selected for application in the investigations of nickel and copper thermal pads. In order to obtain optimal thermal dissipation performance, it is necessary to fully cover the surface of nickel and copper thermal pads with thermal paste. This ensures maximum thermal contact between the thermal pad and the GPU heat sink. The graphic below displays the region where the thermal paste is applied.

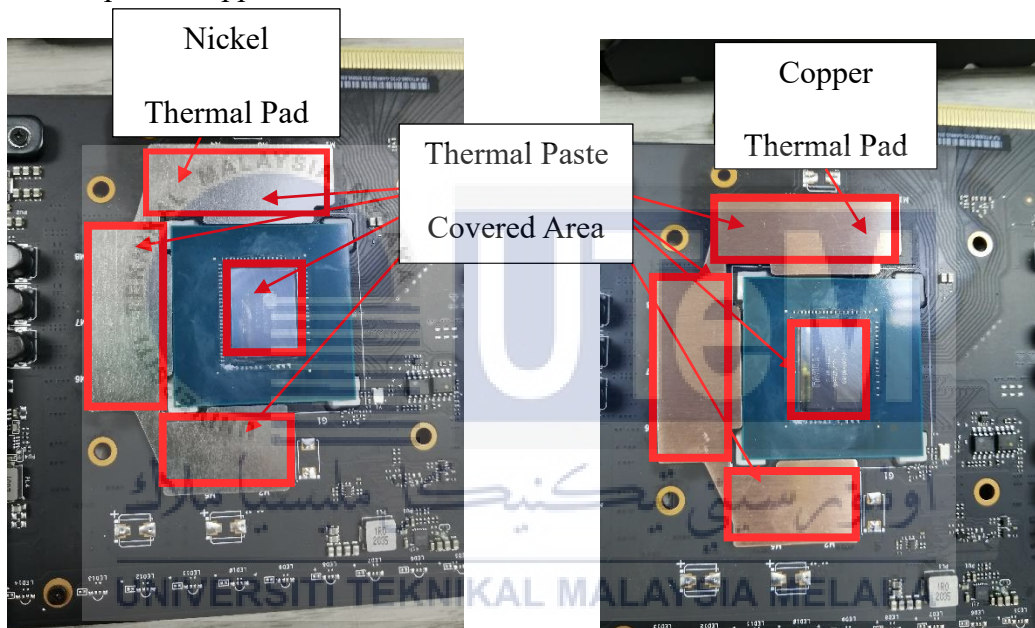


**Figure 3.11** Thermal Paste covered area for GPU on different thermal pad materials.

Once the thermal paste has been applied to the nickel thermal pads and GPU core, the GPU will be reassembled, and testing will commence. The testing method employed was identical to the variable fan speed test, which aimed to determine the optimal fan speed through RSM optimisation. Additionally, a comparison was made between the original thermal pad and nickel and copper thermal pads to assess the impact of different material properties on GPU memory temperature. Furthermore, the energy consumption savings in terms of cooling fan energy consumption were evaluated by comparing the thermal

conductivity of the original thermal pad with that of nickel and copper. The objective was to assess the impact of thermal conductivity on the thermal dissipation performance and energy consumption of a cooling fan.

### 3.7 Performing Response Surface Methodology (RSM) analysis

Conducting an examination of response surface methodology (RSM) is essential to ascertaining the statistical significance of both the response and each term in the model. In order to assess the null hypothesis, the p-value for each term in the model was compared to the significance level to determine the connection between the response and the term. The null hypothesis presented here pertained to the coefficient of the term being equal to zero, indicating that there is no correlation between the term and the response. Typically, the significance threshold, commonly represented as  $\alpha$ , set at 0.05 is generally effective. A significance level of 0.05 signifies a 5% probability of erroneously concluding the presence of a relationship when no such relationship actually exists.

In RSM analysis, it was imperative to ascertain if the P-value was less than or equal to  $\alpha$  or greater than  $\alpha$ . This determination is crucial as it determines the statistical significance, or lack thereof, of the relationship. In this scenario, the P-value for the GPU fan speed, GPU core, and memory temperature should be less than or equal to  $\alpha$  in order to indicate a statistically significant relationship between the response variable and the term. Alternatively, it was necessary to modify the model by excluding the term. According to the Analysis of Variance (ANOVA) conducted using Design Expert software, if a coefficient for a component is found to be significant, it indicates that the means of all levels of that factor are not equal. If the coefficient for a squared term is statistically significant, it indicates that

the relationship between the factor and the response variable may be described by a curved line.

In addition, it was imperative to assess the degree of alignment between the model and our data by scrutinising the goodness-of-fit numbers presented in the Model Summary Table. The Model Summary Table displays the values of S, R-sq, adjusted R-sq, and projected R-sq, which indicate the degree to which our model accurately represents our data. A higher R<sup>2</sup> value suggests a stronger match between the model and the data. The adjusted R<sup>2</sup> was employed to compare models with varying amounts of predictors. The coefficient of determination, R<sup>2</sup>, consistently increases as a predictor is added to the model, regardless of whether there is any actual enhancement to the model's performance. The predicted R<sup>2</sup> is used to assess the accuracy of your model in predicting the response to new observations. A higher R<sup>2</sup> value indicates stronger predicting ability.

Next, it was necessary to assess whether the RSM model satisfies the assumptions of the analysis, as shown by the optimisation recommended by numerical analysis. Residual plots are used to determine the adequacy of the model and assess whether it fits the assumptions of the analysis. In the residuals versus fits plot, a fanning or uneven spreading pattern indicates nonconstant variance, whereas a curved pattern suggests the presence of a missing higher-order term. If a point is significantly distant from zero, it could potentially be an outlier. Similarly, if a point is considerably distant from the other points in the x-direction, it may suggest the presence of an influential point. In addition, a normal probability plot of the residuals was employed to confirm the premise that the residuals follow a normal distribution. If the graphs do not exhibit a linear pattern, it may suggest nonnormality.

### 3.8 Summary

The objective of this study is to use the RSM one-factor technique to identify the ideal speed for the fan by numerical analysis, thereby achieving an optimised fan speed. The improved fan speed will be tested by actual experimentation to confirm the accuracy of the model's response. The study proceeded by using various thermal pad materials, including nickel, copper, and the stock thermal pad which is referring to Arctic TP-3. The RSM study was conducted to determine the best fan speed and compare the performance of Arctic TP-3, nickel, and copper thermal pads. The variation in recommended fan speeds will be evaluated and examined based on the thermal conductivity of the materials and their parameters.



## CHAPTER 4

### RESULTS AND DISCUSSION

#### 4.0 Overview of RSM analysis

This section will go over the results of the RSM analysis that determined the optimal fan speed for three different kinds of thermal pads: the copper thermal pad, the nickel thermal pad, and the Arctic TP-3 thermal pad. In order to provide a quantitative comparison, the response surface analysis would use optimization for the first response surface factor. Considering the thermal conductivity characteristics of the materials and the discrepancies between the two sets of temperatures, the suggested optimization compares the fan speed needed to generate a specific temperature as predicted by the Design Expert software with the actual temperature attained. Also, we'll see what percentage of energy we can save by switching out the original thermal pad with different materials. In order to determine which model was most suited for making predictions, we ran a lack of fit test, compared the models graphically to see which had the fewest outliers, and finally, checked the numerical optimisation solution to make sure the model was fit for the process order. This was all part of the results and discussion analysis.

#### 4.1 Results of Design of Experiments (DOE) for variable fan speed under identical GPU load

##### 4.1.1 Optimization of GPU core temperature-dependent fan speed via response surface-based Response Surface Methodology (RSM) with a single factor

Based on the testing for variable fan speed under identical GPU load, it was required to run 7 times for quadratic model. The results of 7 run of experiments that had been done were shown in the table below:

**Table 4.1** Results of Design of Experiments for variable fan speed on original thermal pad.

| Std. run no. | Run | Factor          | Response                |                           |
|--------------|-----|-----------------|-------------------------|---------------------------|
|              |     | Fan Speed (RPM) | GPU Core Temperature °C | GPU Memory Temperature °C |
| 5            | 1   | 3000            | 43.6                    | 54.5                      |
| 2            | 2   | 550             | 89.7                    | 104                       |
| 1            | 3   | 550             | 89.9                    | 104.5                     |
| 4            | 4   | 2387.5          | 46.4                    | 57.4                      |
| 6            | 5   | 3000            | 44.7                    | 55.5                      |
| 7            | 6   | 1775            | 49.2                    | 60.1                      |
| 3            | 7   | 1162.5          | 56.7                    | 68.3                      |

It was observed, according to the data in Table 4.1, that as fan speed increased, the GPU core and memory temperatures decreased gradually. This was significant because it was related to the study of thermodynamics, as an increase in fan speed would increase the velocity of air blowing onto the GPU's heat sink, resulting in more powerful forced convection and a literal acceleration in the rate at which heat is transferred away from the GPU. At 3000 rpm, the utmost fan speed, both the core and memory temperatures were at their minimum. Nonetheless, it was observed that the temperature of the GPU memory was significantly higher than that of the GPU core, indicating that the GPU memory had produced significantly more heat than the GPU core. Therefore, the component of a GPU

that generated the most heat was the memory. When the fan speed was set to 550 rpm, the memory reached its maximum temperature of 104°C. Additionally, as the fan speed increased from 550 rpm to 1162.5 rpm, the greatest temperature difference occurred, which decreased from 89.7°C to 56.7°C, a 33°C difference. GPU core and memory temperature were slightly affected by this fan speed, whereas the temperature difference was only about 10.9°C for the fan speed ranging from 550 rpm to 2387.5 rpm, which was not as significant as the temperature difference for the fan speed ranging from 550 rpm to 1162.5 rpm. A marginal temperature reduction of approximately 1.5°C was observed across the fan speed spectrum of 2387.5 rpm to 3000 rpm. Based on this scenario, it was determined that increasing the fan speed starting from 2387.5 rpm had no appreciable effect on the change in temperature; thus, the maximal cooling capacity had already been reached.

**Table 4.2** Model Evaluation of Quartic Order for GPU Core and Memory Temperature

| Term           | Std Error | VIF   | Ri-Squared | 2 Std. Dev. |
|----------------|-----------|-------|------------|-------------|
| A              | 1.89      | 16.13 | 0.9380     | 6.3 %       |
| A <sup>2</sup> | 6.26      | 48.36 | 0.9793     | 5.5 %       |
| A <sup>3</sup> | 2.00      | 16.13 | 0.9380     | 6.2 %       |
| A <sup>4</sup> | 5.54      | 48.36 | 0.9793     | 5.6 %       |

**Table 4.3** Summary of Statistics of various models for GPU Core Temperature

| Source         | Sequential<br>p-value | Lack of Fit<br>p-value | Adjusted<br>R-Squared | Predicted<br>R-Squared |                         |
|----------------|-----------------------|------------------------|-----------------------|------------------------|-------------------------|
| Linear         | 0.0068                | 0.0018                 | 0.7572                | 0.6221                 |                         |
| Quadratic      | 0.0079                | 0.0084                 | 0.9569                | 0.9316                 |                         |
| <u>Cubic</u>   | <u>0.0068</u>         | <u>0.0690</u>          | <u>0.9964</u>         | <u>0.9824</u>          | <b><u>Suggested</u></b> |
| <u>Quartic</u> | <u>0.0690</u>         |                        | <u>0.9993</u>         |                        | <b><u>Suggested</u></b> |
| Fifth          |                       |                        |                       |                        | Aliased                 |

Table 4.3 illustrates the P-values, Adjusted  $R^2$ , and Predicted  $R^2$  values for the linear, quadratic, cubic, and quartic models that were studied in the investigation. The sequential p-value column displays the level of significance for each model term as it is added to the model in succession. The observed data or more extreme outcomes are used to calculate the likelihood of receiving such data if the null hypothesis is correct. A p-value below 0.05 indicates that the term is statistically significant, implying that it has a meaningful impact on the variation in the response variable. The summary of statistics for GPU core temperature models indicates that all models had a substantial impact on the variance in the response variable. However, only the quartic model had a slightly higher value than 0.05. The Adjusted  $R^2$  column displays the fraction of the overall variability in the dependent variable that can be explained by the model while considering the number of independent variables. A greater adjusted  $R^2$  value signifies a superior alignment of the model with the data. The Predicted  $R^2$  column is the anticipated proportion of variability in future observations that the model can explain. A higher Predicted  $R^2$  score suggests that the model is more likely to exhibit good performance when applied to new data.

Upon examination of the table, it is evident that the cubic and quartic models exhibit the greatest Adjusted  $R^2$  values (0.9964 and 0.9993) as well as a Predicted  $R^2$  value of

0.9824. This indicates that these models offer the most accurate fit to the data and are therefore the optimal choices for predicting the response variable. The quadratic model exhibits a significantly high Adjusted  $R^2$  value of 0.9569, while the linear model demonstrates the lowest Adjusted  $R^2$  values. The fifth model does not provide any Adjusted  $R^2$  or predicted  $R^2$  values and is marked as aliased. The meaning conveyed is indistinguishable from another model due to collinearity or confounding factors. Therefore, the cubic and quartic models were chosen for further examination in this study.

**Table 4.4** ANOVA outcome for the suggested cubic model on GPU Core Temperature

| Source         | Sum of Squares | df | Mean Square | F Value | p-value |                 |
|----------------|----------------|----|-------------|---------|---------|-----------------|
| Model          | 2586.94        | 3  | 862.31      | 551.45  | 0.0001  | Significant     |
| A-FANSPEED     | 10.47          | 1  | 10.47       | 6.70    | 0.0812  |                 |
| A <sup>2</sup> | 449.98         | 1  | 449.98      | 287.76  | 0.0004  |                 |
| A <sup>3</sup> | 69.72          | 1  | 69.72       | 44.59   | 0.0068  |                 |
| Residual       | 4.69           | 3  | 1.56        |         |         |                 |
| Lack of Fit    | 4.07           | 1  | 4.07        | 13.01   | 0.0690  | Not significant |
| Pure Error     | 0.63           | 2  | 0.31        |         |         |                 |
| Cor Total      | 2591.63        | 6  |             |         |         |                 |

Table 4.4 presents the ANOVA results for the cubic model based on GPU core temperature. The sources of variation are enumerated, accompanied by their respective sums of squares, degrees of freedom, mean squares, F-values, and p-values. ANOVA uses the F-value to assess the significance of the variation between components. The estimation is obtained by dividing the variation among the factors by the variance within the factors. The F-value of 2586.94 indicates that the model is statistically significant, as the probability of

attaining such a high F-value by chance alone is very low at 0.0001%. The p-values for FANSPEED are greater than those for lack of fit, indicating that both FANSPEED and lack of fit are not significant factors in impacting the response. The p-values for the  $A^2$  and  $A^3$  terms are more than 0.05, suggesting that they are not statistically significant. However, the p-value for the model terms is less than 0.0001, indicating that it is a statistically significant term.

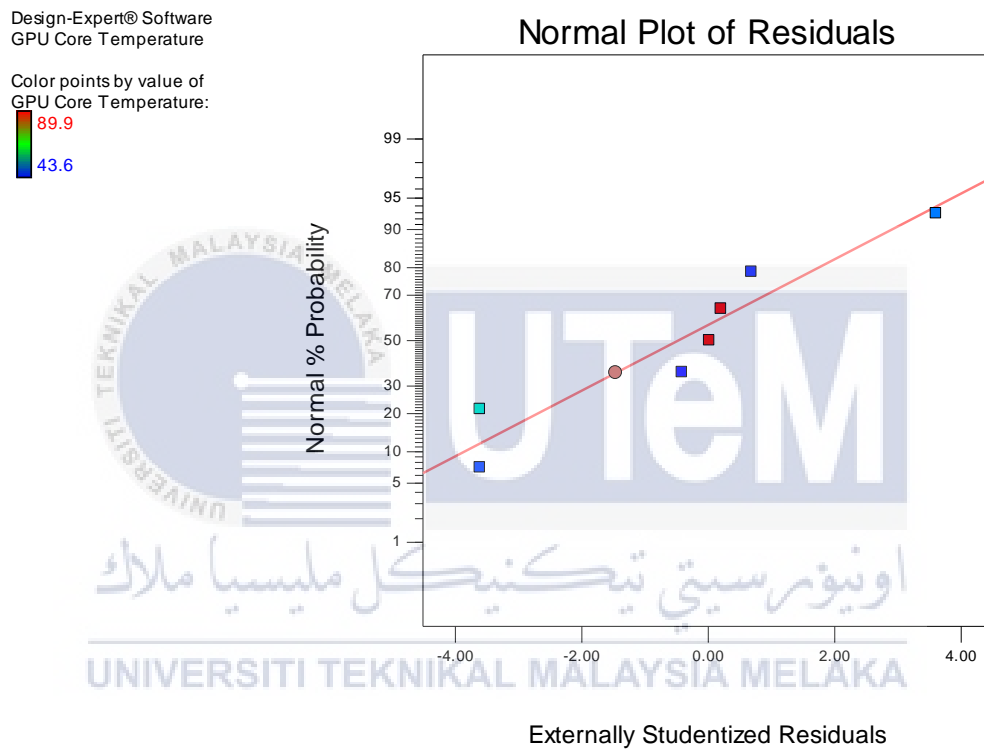


**Figure 4.1** Normal Plot of Residuals against Externally Studentized Residuals of Cubic model on GPU Core Temperature

The points in the normal plot of residuals vs. externally studentized residuals form a straight line, indicating that the residuals follow a normal distribution. Along the straight line, there were just a handful of noticeable outliers, but they were largely minor. Regression did not encounter any major problems due to the low leverage observations, which were only an outlier.

Design-Expert® Software  
GPU Core Temperature

Color points by value of  
GPU Core Temperature:  
89.9  
43.6

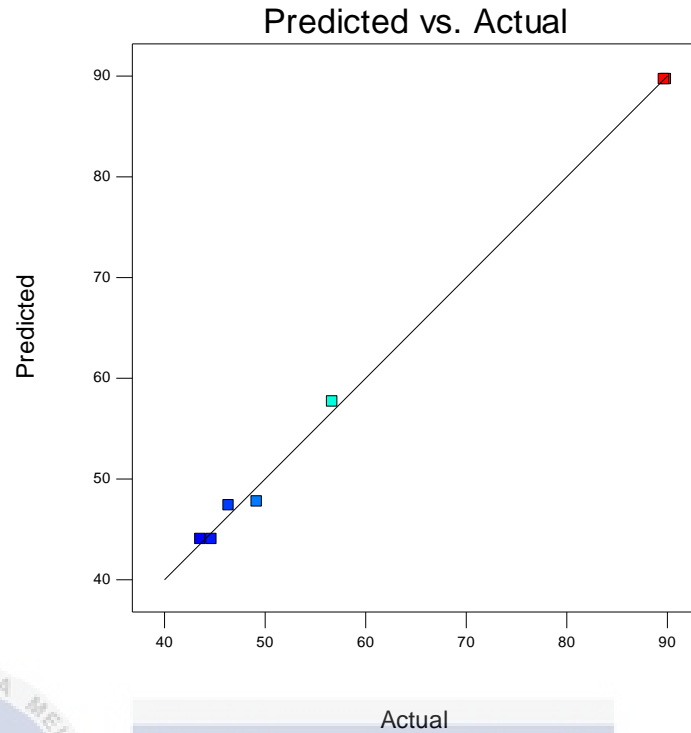


**Figure 4.2** Graph of Predicted against Actual of cubic model on GPU Core Temperature

A graph comparing the expected and actual response levels may be seen in Figure 4.2. A value or set of values that defy easy model prediction can be located with its help. A high linear association with the real core temperature was observed in the graph in Figure 4.2. Thanks to the 45° line's equal distribution of the data points, we can see that the expected and actual responses are reasonably in agreement. Based on the corresponding fan speed RPM, it appears that the GPU core temperature has been successfully forecasted using a cubic model. A tiny subset of data points, called low leverage data, might skew the results of a fitted regression model with little effect.

Design-Expert® Software  
 Factor Coding: Actual  
 GPU Core Temperature (°C)  
 ● Design Points  
 --- 95% CI Bands  
 X1 = A: FANSPEED

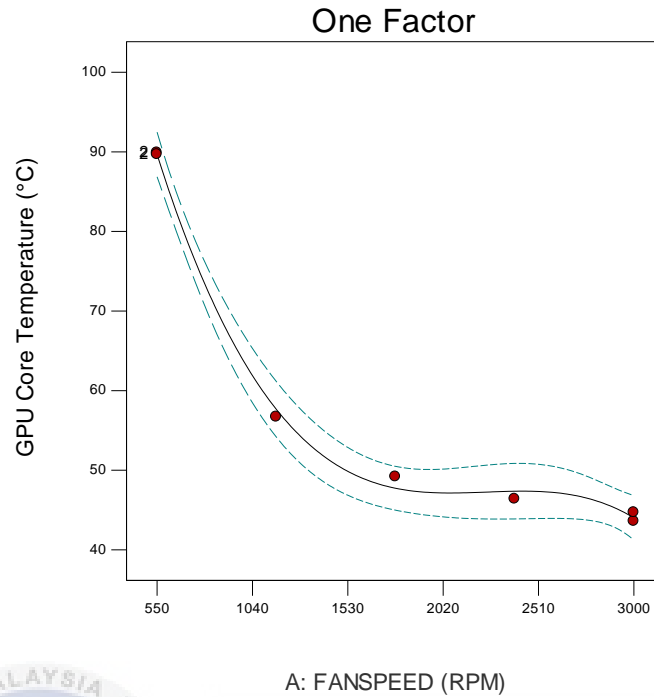


**Figure 4.3** Model Graph of cubic model on GPU Core Temperature

The reaction surface plot of the GPU Core indicates that the temperature changes with the speed of the fan. The 95% confidence band on the mean prediction at any given GPU core temperature is shown by the dotted lines. As demonstrated, every fan speed and accompanying GPU core temperature fell inside the dotted lines, indicating a 5% possibility of making an inaccurate decision using this supposed proper model. A 95% confidence interval spanning 91.5 to 43.6 degrees Celsius is seen from the model graph, which represents the response mean value.

**Table 4.5** ANOVA outcome for the suggested quartic model on GPU Core Temperature

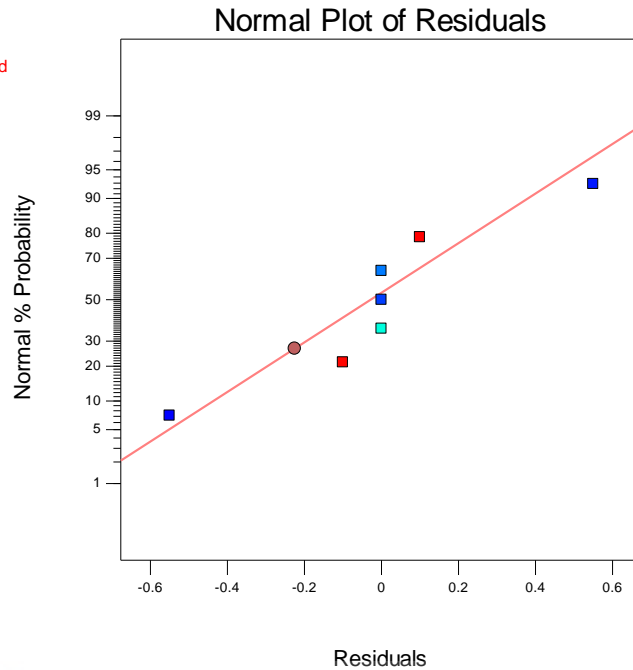
| Source         | Sum of Squares | df | Mean Square | F Value | p-value |                    |
|----------------|----------------|----|-------------|---------|---------|--------------------|
| Model          | 2591.01        | 4  | 647.75      | 2072.81 | 0.0005  | <b>Significant</b> |
| A-FANSPEED     | 10.47          | 1  | 10.47       | 33.50   | 0.0286  |                    |
| A <sup>2</sup> | 1.11           | 1  | 1.11        | 3.56    | 0.1998  |                    |
| A <sup>3</sup> | 69.72          | 1  | 69.72       | 223.11  | 0.0045  |                    |
| A <sup>4</sup> | 4.07           | 1  | 4.07        | 13.01   | 0.0690  |                    |
| Pure Error     | 0.63           | 2  | 0.31        |         |         |                    |
| Cor Total      | 2591.63        | 6  |             |         |         |                    |

Table 4.5 presents the ANOVA results for the quartic model based on GPU core temperature. The F-value of 2591.01 indicates that the model is statistically significant, as the probability of attaining such a high F-value by chance alone is very low at 0.005%. The p-values for FANSPEED are greater than those for A<sup>3</sup> and A<sup>4</sup>, indicating that all FANSPEED, A<sup>3</sup> and A<sup>4</sup> are not significant factors in impacting the response. The p-values for the A<sup>2</sup> terms are more than 0.05, suggesting that they are not statistically significant. However, the p-value for the model terms is less than 0.005, indicating that it is a statistically significant term.

Design-Expert® Software  
GPU Core Temperature

Studentized residuals recommended

Color points by value of  
GPU Core Temperature:



**Figure 4.4** Normal Plot of Residuals against Residuals of quartic model on GPU Core Temperature

Upon analysing the normal plot of residuals, it was noted that the Design Expert was not able to calculate all externally studentized residuals hence it was switched to normal plot of residuals against residuals. From the plot, it was determined that there are few points ranging from 89.9 until 43.6 had run against the lines which emitted as outlier. Since we did not detect any conspicuous outliers or atypical observations, There were simply a few insignificant observations. The low leverage observations were an anomaly that did not pose a significant issue in regression.

Design-Expert® Software  
GPU Core Temperature

Color points by value of  
GPU Core Temperature:  
89.9  
43.6

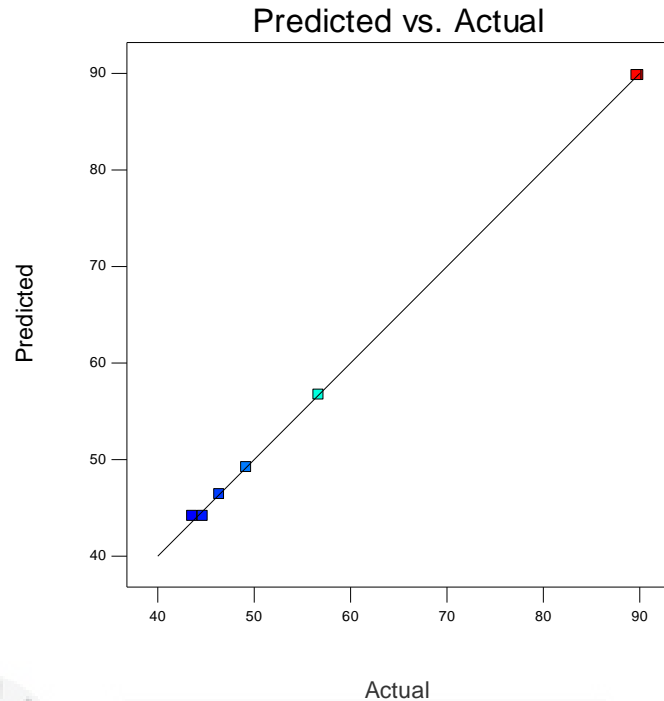


**Figure 4.5** Graph of Predicted against Actual of quartic model on GPU Core Temperature

Figure 4.5 displays a graph that compares the anticipated and observed levels of reaction. The assistance of this tool can be used to identify a value or group of values that are difficult to anticipate using a model. The graph in Figure 4.5 demonstrates a strong positive correlation with the actual core temperature. Due to the even distribution of data points along the 45° line, it is evident that the expected and actual responses are fairly consistent. The quartic model has effectively predicted the GPU core temperature based on the associated fan speed RPM. Based on the aforementioned result, it can be inferred that the quartic model is an effective tool for exploring the design space of GPU core temperature.

Design-Expert® Software  
 Factor Coding: Actual  
 GPU Core Temperature (°C)  
 ● Design Points  
 --- 95% CI Bands  
 X1 = A: FANSPEED

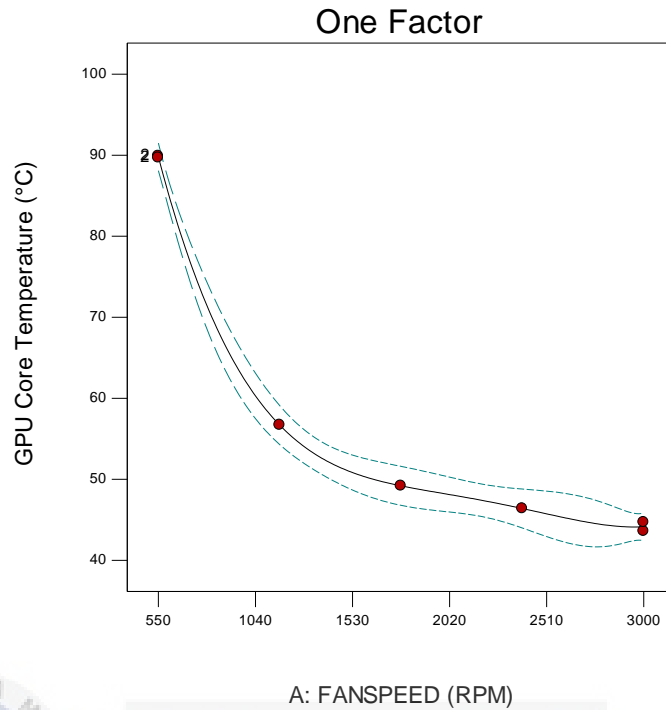


**Figure 4.6** Model Graph of Quartic model on GPU Core Temperature

The GPU Core's reaction surface plot demonstrates that the temperature varies in accordance with the fan's speed. The dotted lines represent the 95% confidence interval for the mean prediction at any certain GPU core temperature. As shown, all fan speeds and corresponding GPU core temperatures remained within the boundaries represented by the dotted lines, suggesting a 5% chance of making an erroneous decision using this presumed accurate model. According to the displayed model graph, it was seen that the gap between two dotted lines was thinner for the quartic model compared to the cubic model. This suggests that the quartic model had less error in forecasting the real GPU core temperature at different fan speeds. Therefore, the quartic model is the most appropriate choice for optimising fan speed.

#### 4.1.2 Optimization of GPU memory temperature-dependent fan speed via response surface-based Response Surface Methodology (RSM) with a single factor

**Table 4.6** Summary of Statistics of various models for GPU Memory Temperature

| Source         | Sequential<br>p-value | Lack of Fit<br>p-value | Adjusted<br>R-Squared | Predicted<br>R-Squared |                         |
|----------------|-----------------------|------------------------|-----------------------|------------------------|-------------------------|
| Linear         | 0.0072                | 0.0015                 | 0.7519                | 0.6141                 |                         |
| Quadratic      | 0.0079                | 0.0071                 | 0.9561                | 0.9305                 |                         |
| <u>Cubic</u>   | <u>0.0055</u>         | <u>0.0668</u>          | <u>0.9968</u>         | <u>0.9844</u>          | <b><u>Suggested</u></b> |
| <u>Quartic</u> | <u>0.0668</u>         |                        | <u>0.9994</u>         |                        | <b><u>Suggested</u></b> |
| Fifth          |                       |                        |                       |                        | Aliased                 |

Table 4.6 displays the cubic and quartic models, which have the greatest Adjusted  $R^2$  values of 0.9968 and 0.9994, respectively. Additionally, cubic models have a Predicted  $R^2$  value of 0.9844. Utilising these models to forecast the response variable is the optimal choice since they offer the most accurate alignment with the data. The quadratic model exhibits a significantly high Adjusted  $R^2$  value of 0.9561, while the linear model has the lowest value. Due to its aliasing, the fifth model does not provide any Adjusted  $R^2$  or Predicted  $R^2$  values. Due to collinearity or other complicating conditions, the meaning ascribed is indistinguishable from another model. Therefore, this study will only examine the cubic and quartic models.

**Table 4.7** ANOVA outcome for the suggested cubic model on GPU Memory Temperature

| Source         | Sum of Squares | df | Mean Square | F Value | p-value |                    |
|----------------|----------------|----|-------------|---------|---------|--------------------|
| Model          | 3022.36        | 3  | 1007.45     | 624.70  | 0.0001  | <b>Significant</b> |
| A-FANSPEED     | 11.16          | 1  | 11.16       | 6.92    | 0.0782  |                    |
| A <sup>2</sup> | 537.39         | 1  | 537.39      | 333.23  | 0.0004  |                    |
| A <sup>3</sup> | 83.72          | 1  | 83.72       | 51.91   | 0.0055  |                    |
| Residual       | 4.84           | 3  | 1.61        |         |         |                    |
| Lack of Fit    | 4.21           | 1  | 4.21        | 13.48   | 0.0668  | Not significant    |
| Pure Error     | 0.63           | 2  | 0.31        |         |         |                    |
| Cor Total      | 3027.20        | 6  |             |         |         |                    |

The ANOVA findings for the cubic model incorporating GPU core temperature are presented in Table 4.7. The model exhibits statistical significance, as evidenced by its F-value of 3022.36. The probability of obtaining such a high F-value by chance alone is exceedingly low, at 0.0001%. The observation that the p-value of FANSPEED is greater than that of A<sup>2</sup> and A<sup>3</sup> implies that none of these factors have a significant impact on the outcome. The lack of fit terms is not statistically significant since their p-values exceed 0.05. The model terms exhibit p-values below 0.0001, indicating their statistical significance.

Design-Expert® Software  
GPU Memory Temperature

Color points by value of  
GPU Memory Temperature:

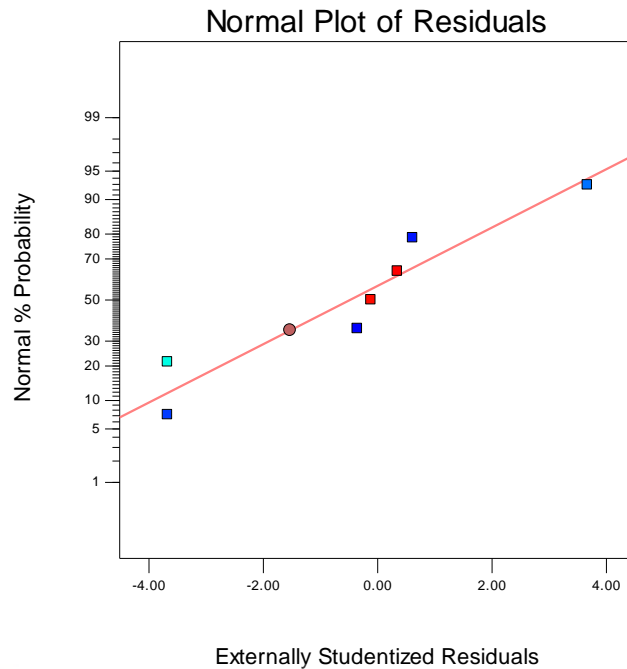
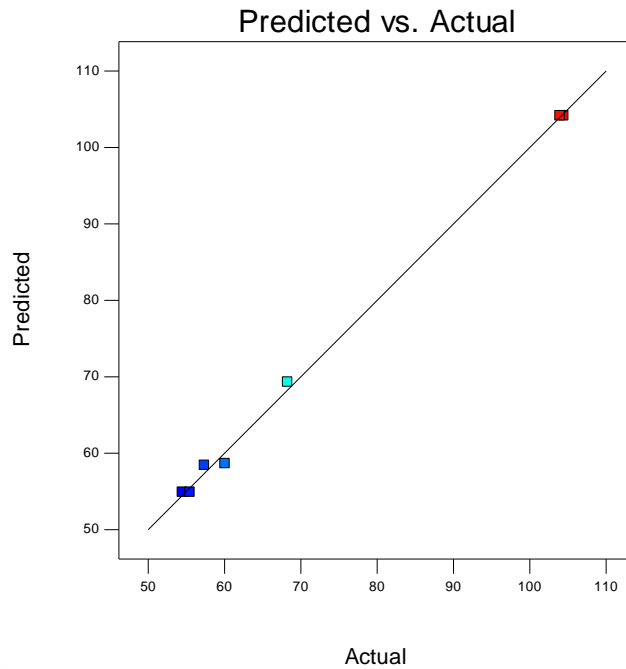


**Figure 4.7** Normal Plot of Residuals against Externally Studentized Residuals of cubic model on GPU Memory Temperature

Figure 4.7 shows a straight line representing the normal distribution of residuals against externally studentized residuals. This means that the residuals are distributed normally. On the linear path, there were just a few noticeable anomalies, but they were mostly insignificant. Regression did not face any severe complications due to the low leverage observations, which were merely an aberration.

Design-Expert® Software  
 GPU Memory Temperature

Color points by value of  
 GPU Memory Temperature:  
 104.5  
 54.5



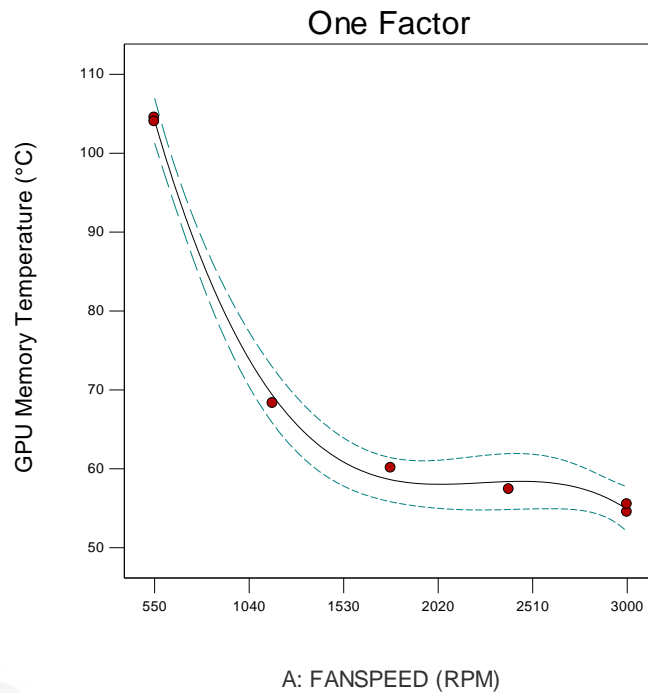
**Figure 4.8** Graph of Predicted against Actual of cubic model on GPU Memory Temperature

Figure 4.8 shows a graph that compares the expected and actual reaction levels. It can help you find a value or set of values that are difficult to forecast using a model. Figure 4.8's graph showed a strong linear relationship with the actual core temperature. The 45° line shows that the data points are evenly distributed, so we can see that the expected and actual responses are rather close to each other. It seems that the cubic model has been successful in forecasting the GPU core temperature, as indicated by the associated fan speed RPM. Low leverage data refers to a small selection of data points that may slightly alter the outcomes of a fitted regression model.

Design-Expert® Software  
 Factor Coding: Actual  
 GPU Memory Temperature (°C)

● Design Points  
 --- 95% CI Bands

X1 = A: FANSPEED



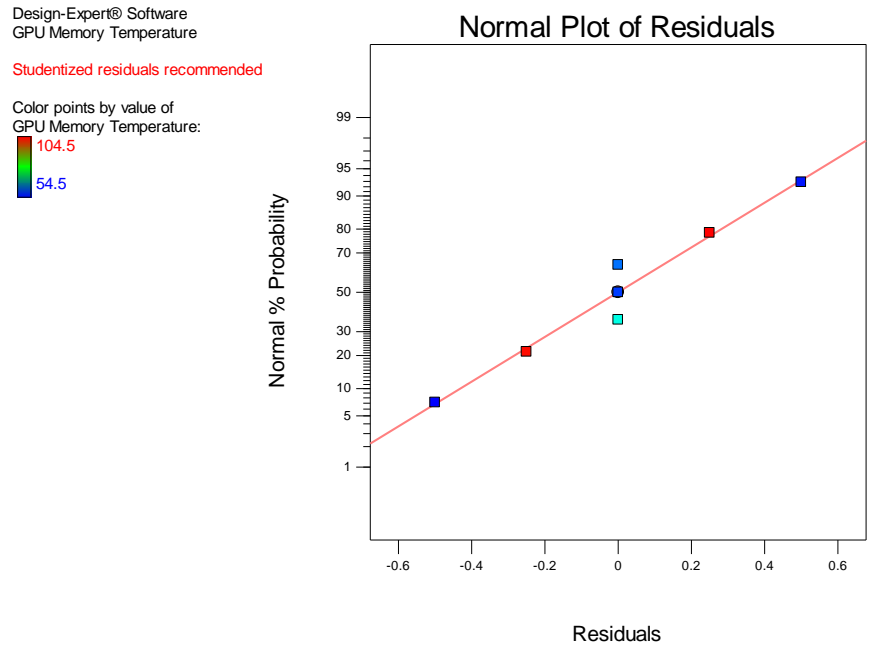
**Figure 4.9** Model Graph of Cubic model on GPU Memory Temperature

Figure 4.9 shows the GPU Core's reaction surface map, which shows that the temperature changes as the fan speed does. The dashed lines represent the 95% confidence interval around the mean projection for each specific GPU core temperature. All of the fan speeds and GPU core temperatures were within the specified range, suggesting a 5% chance of making a mistake with this purportedly precise model. The reaction mean value, as shown by the model graph, falls within a 95% confidence zone of about 54.5 degrees Celsius.

**Table 4.8** ANOVA outcome for the suggested quartic model on GPU Memory Temperature

| Source         | Sum of Squares | df | Mean Square | F Value | p-value |                    |
|----------------|----------------|----|-------------|---------|---------|--------------------|
| Model          | 3026.57        | 4  | 756.64      | 2421.26 | 0.0004  | <b>Significant</b> |
| A-FANSPEED     | 11.16          | 1  | 11.16       | 35.73   | 0.0269  |                    |
| A <sup>2</sup> | 1.70           | 1  | 1.70        | 5.43    | 0.1452  |                    |
| A <sup>3</sup> | 83.72          | 1  | 83.72       | 267.91  | 0.0037  |                    |
| A <sup>4</sup> | 4.21           | 1  | 4.21        | 13.48   | 0.0668  |                    |
| Pure Error     | 0.62           | 2  | 0.31        |         |         |                    |
| Cor Total      | 3027.20        | 6  |             |         |         |                    |

Table 4.8 presents the ANOVA results for the quartic model based on GPU Memory Temperature. The F-value of 2421.26 indicates that the model is statistically significant, as the probability of attaining such a high F-value by chance alone is very low at 0.0004%. The p-values for FANSPEED are greater than those for A<sup>3</sup> and A<sup>4</sup>, indicating that all FANSPEED, A<sup>3</sup> and A<sup>4</sup> are not significant factors in impacting the response. The p-values for the A<sup>2</sup> terms are more than 0.05, suggesting that they are not statistically significant. However, the p-value for the model terms is less than 0.0004, indicating that it is a statistically significant term.



**Figure 4.10** Normal Plot of Residuals against Residuals of quartic model on GPU Memory Temperature

Upon evaluating the normal plot of residuals, it was noticed that the design expert was not able to calculate all externally studentized residuals; hence, it was switched to the normal plot of residuals against residuals. From the plot, it was discovered that a few points of normal probability ranging from 64.3 to 35.7 had run against the lines that emitted an outlier. Since we did not find any apparent outliers or abnormal observations, there were only a few minor observations. The low leverage observations were an aberration that did not pose a substantial challenge in regression.

Design-Expert® Software  
GPU Memory Temperature

Color points by value of  
GPU Memory Temperature:

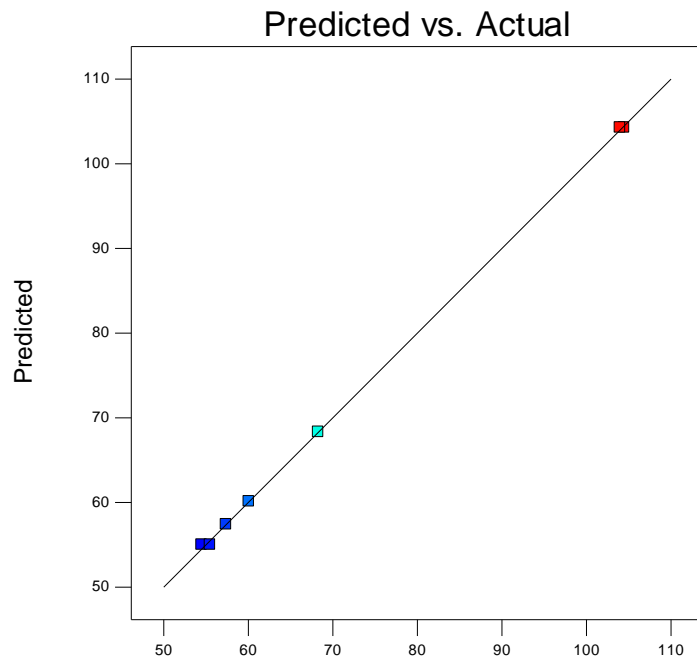


**Figure 4.11** Graph of Predicted against Actual of quartic model on GPU Memory Temperature

Figure 4.11 shows a graph that contrasts the expected and actual levels of response. If you're having trouble predicting a certain value or set of data using a model, this tool can help. The real core temperature is strongly positively correlated with the curve in Figure 4.11. The data points are evenly distributed along the 45° line, so it's clear that the expected and actual responses are rather consistent. In this case, the quartic model's prediction of the GPU core temperature from the corresponding fan speed RPM was spot on. The data shown above suggests that the quartic model works well for investigating GPU core temperature design space.

Design-Expert® Software  
 Factor Coding: Actual  
 GPU Memory Temperature (°C)  
 ● Design Points  
 --- 95% CI Bands  
 X1 = A: FANSPEED

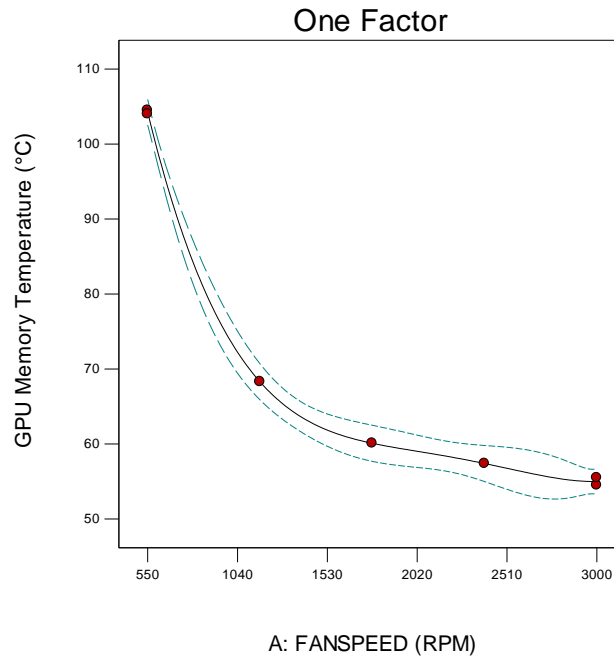


**Figure 4.12** Model Graph of quartic model on GPU Memory Temperature

The response surface plot of the GPU Core shows that the temperature changes as a function of the fan speed. The mean projection at any given GPU core temperature is accompanied by a 95% confidence interval, shown by the dotted lines. Considering that all fan speeds and GPU core temperatures stayed inside the dotted lines, there's a 5% possibility that this assumedly accurate model made a mistake. In comparison to the cubic model, the quartic model had a narrower space between the two dotted lines, as shown in the model graph. Results like these show that the quartic model was better at predicting the actual GPU core temperature over a range of fan speeds. Optimising fan speed based on GPU memory temperature is best accomplished using the quartic model.

## 4.2 Results of RSM analysis of Nickel thermal pad on GPU core and memory temperature

### 4.2.1 Optimization of GPU Core Temperature on nickel thermal pad via response surface-based Response Surface Methodology (RSM) with a single factor

Based on the testing for variable fan speed under identical GPU load for nickel thermal pad, it was required to run 7 times for quadratic model. The results of 7 run of experiments that had been done were shown in the table below:

**Table 4.9** Results of Design of Experiments for variable fan speed on nickel thermal pad.

| Std. run no. | Run | Factor          | Response                |                           |
|--------------|-----|-----------------|-------------------------|---------------------------|
|              |     | Fan Speed (RPM) | GPU Core Temperature °C | GPU Memory Temperature °C |
| 4            | 1   | 2387.5          | 53.2                    | 66.3                      |
| 7            | 2   | 1775            | 56.8                    | 69.3                      |
| 2            | 3   | 550             | 79.4                    | 92.4                      |
| 1            | 4   | 550             | 79.9                    | 93                        |
| 5            | 5   | 3000            | 51.8                    | 64.7                      |
| 3            | 6   | 1162.5          | 61.7                    | 75.1                      |
| 6            | 7   | 3000            | 51.4                    | 64.4                      |

According to the data in Table 4.8, it was noted that the temperatures of the GPU core and memory reduced progressively as the fan speed rose. An important reason for this's importance in thermodynamics is that a faster fan speed would cause air to blow faster onto the GPU's heat sink, leading to stronger forced convection and a real acceleration in the rate of heat transfer. The lowest temperatures for the core and memory were seen at 3000 rpm, which is the maximum fan speed. Still, it was noted that the GPU memory had a far greater temperature than the GPU core, suggesting that the memory had generated a lot more heat. Thus, the GPU's memory was the heat-generating component. The memory attained a maximum temperature of 93°C when the fan speed was set to 550 rpm, which is marginally lower than the original thermal pad. The nickel thermal pad's high thermal conductivity and

low thermal contact resistance likely caused this. Compared to the old thermal pad, the nickel one had better thermal contact resistance and greater thermal conductivity, allowing more heat to be transferred out of the GPU memory board. In addition, the biggest temperature difference was seen for the GPU core temperature, which dropped from 79.9°C to 61.7°C, an 18.2°C drop, when the fan speed increased from 550 rpm to 1162.5 rpm. The fan speed had a small but noticeable effect on the temperature of the GPU memory; however, the temperature differential between the GPU core and the fan speed range of 550 rpm to 1162.5 rpm was much larger, at 17.9°C. From 2387.5 rpm all the way up to 3000 rpm, the fan speed spectrum showed a slight drop in temperature of about 1.4°C. In this case, we found that increasing the fan speed from 2387.5 rpm had no noticeable impact on the temperature change, meaning that we had reached the maximum cooling capability.

**Table 4.10** Model Evaluation of Quartic Order for GPU Core and Memory Temperature on nickel thermal pad.

| Term           | Std Error | VIF   | Ri-Squared | 2 Std. Dev. |
|----------------|-----------|-------|------------|-------------|
| A              | 1.89      | 16.13 | 0.9380     | 6.3 %       |
| A <sup>2</sup> | 6.26      | 48.36 | 0.9793     | 5.5 %       |
| A <sup>3</sup> | 2.00      | 16.13 | 0.9380     | 6.2 %       |
| A <sup>4</sup> | 5.54      | 48.36 | 0.9793     | 5.6 %       |

**Table 4.11** Summary of Statistics of various models for GPU Core Temperature

| Source         | Sequential<br>p-value | Lack of Fit<br>p-value | Adjusted<br>R-Squared | Predicted<br>R-Squared |                         |
|----------------|-----------------------|------------------------|-----------------------|------------------------|-------------------------|
| Linear         | 0.0028                | 0.0023                 | 0.8287                | 0.7312                 |                         |
| Quadratic      | 0.0055                | 0.0128                 | 0.9746                | 0.9586                 |                         |
| <u>Cubic</u>   | <u>0.0267</u>         | <u>0.0427</u>          | <u>0.9948</u>         | <u>0.9739</u>          | <b><u>Suggested</u></b> |
| <u>Quartic</u> | <u>0.0427</u>         |                        | <u>0.9993</u>         |                        | <b><u>Suggested</u></b> |
| Fifth          |                       |                        |                       |                        | Aliased                 |

As accordance to Table 4.10, the cubic and quartic models stand out with the highest adjusted  $R^2$  values (0.9948 and 0.9993) and a predicted  $R^2$  value of 0.9739, as can be seen from the table. This means that these models are the best options for predicting the response variable since they provide the best fit to the data. With an adjusted  $R^2$  value of 0.9993, the quartic model stands out, while the linear model shows the lowest results. As it is labelled as aliased, the fifth model fails to supply either adjusted  $R^2$  or projected  $R^2$  values. Because of collinearity or other complicating factors, the meaning that is given is identical to another model. As a result, this research focused on the cubic and quartic models.

**Table 4.12** ANOVA outcome for the suggested cubic model on GPU Core Temperature on nickel thermal pad

| Source         | Sum of Squares | df | Mean Square | F Value | p-value Prob > F |                    |
|----------------|----------------|----|-------------|---------|------------------|--------------------|
| Model          | 941.68         | 3  | 313.89      | 384.14  | 0.0002           | <b>Significant</b> |
| A-FANSPEED     | 12.37          | 1  | 12.37       | 15.14   | 0.0301           |                    |
| A <sup>2</sup> | 118.76         | 1  | 118.76      | 145.33  | 0.0012           |                    |
| A <sup>3</sup> | 13.57          | 1  | 13.57       | 16.60   | 0.0267           |                    |
| Residual       | 2.45           | 3  | 0.82        |         |                  |                    |
| Lack of Fit    | 2.25           | 1  | 2.25        | 21.92   | 0.0427           | <b>Significant</b> |
| Pure Error     | 0.20           | 2  | 0.10        |         |                  |                    |
| Cor Total      | 944.13         | 6  |             |         |                  |                    |

Results of the analysis of variance (ANOVA) for the cubic model that relies on the temperature of the GPU core on a nickel thermal pad are shown in Table 4.11. Because a big F-value like this can only happen by accident (with a probability of only 0.02%), the 941.68 F-value indicates that the model is statistically significant. The significance of the model terms was demonstrated by "Prob > F" values below 0.0500. The A<sup>2</sup> and A<sup>3</sup> terms are statistically significant, as their p-values are smaller than 0.05. The significance of the lack of fit is indicated by the "Lack of Fit F-value" of 21.92. The likelihood of a "Lack of Fit F-value" of this magnitude occurring as a result of random chance is 4.27%. The request was made for the model to fit because the absence of fit is considerable.

Design-Expert® Software  
GPU Core Temperature

Color points by value of  
GPU Core Temperature:

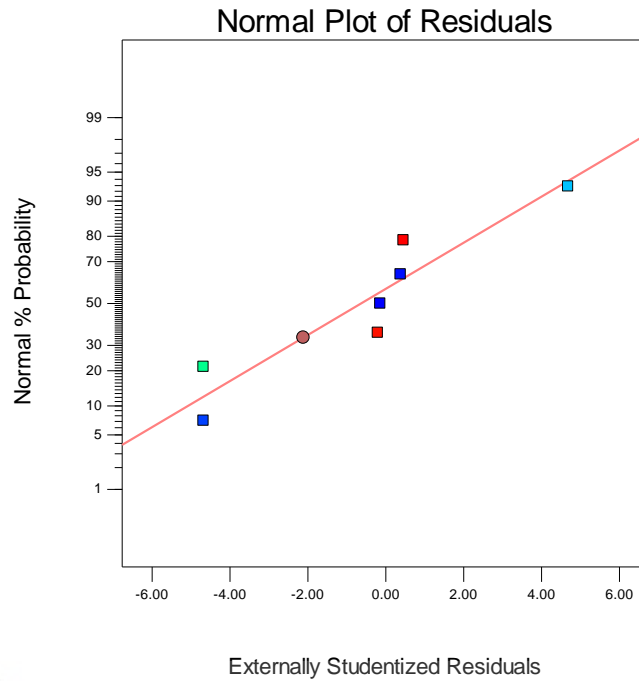


**Figure 4.13** Normal Plot of Residuals against Externally Studentized Residuals of Cubic model of GPU Core Temperature on nickel thermal pad

There is a straight line connecting the points in the normal plot of externally studentized residuals to the residuals, suggesting that the residuals are normally distributed. Only a small number of outliers were really evident along the straight line. The low leverage observations were merely an outlier; therefore, regression did not face any severe complications.

Design-Expert® Software  
GPU Core Temperature

Color points by value of  
GPU Core Temperature:

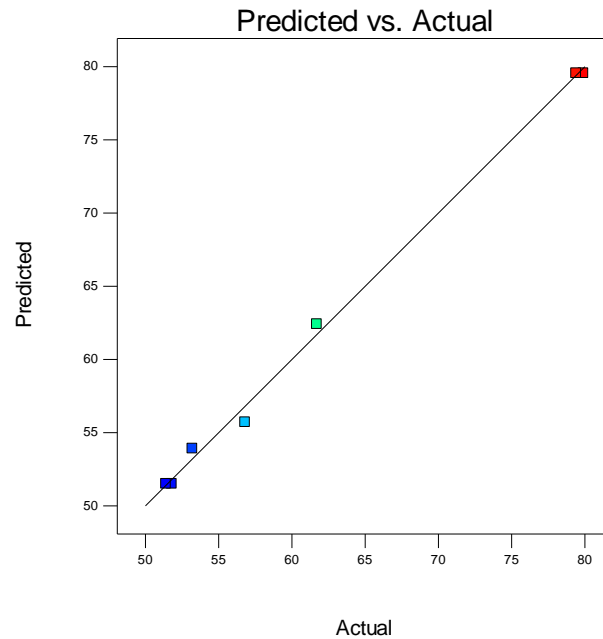


**Figure 4.14** Graph of Predicted against Actual of cubic model of GPU Core Temperature on nickel thermal pad.

Figure 4.13 shows a graph contrasting the predicted and observed levels of response. It can help you find a value or set of values that are difficult to forecast using a model. Figure 4.13 shows a very linear relationship with the actual core temperature. We can observe that the anticipated and actual replies are quite congruent because the data points on the 45° line are evenly distributed. It seems that the cubic model has been successful in forecasting the GPU core temperature, as indicated by the associated fan speed RPM. The results of a fitted regression model could be slightly skewed by a small group of data points known as low-leverage data.

Design-Expert® Software  
 Factor Coding: Actual  
 GPU Core Temperature (°C)  
 ● Design Points  
 ---- 95% CI Bands  
 X1 = A: FANSPEED

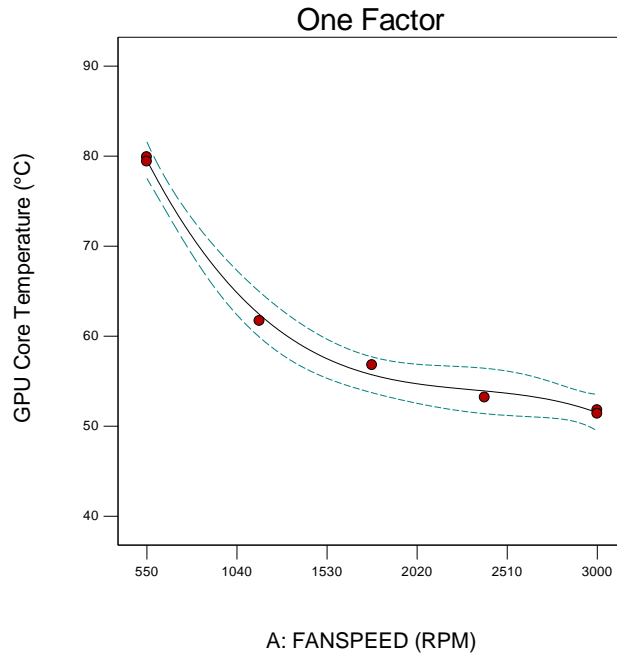


**Figure 4.15** Model Graph of cubic model of GPU Core Temperature on nickel thermal pad

Figure 4.14 displays a graph contrasting the projected and observed levels of response. It can help you identify a value or set of variables that are tough to forecast using a model. Figure 4.14 demonstrates a highly linear relationship with the real core temperature. We can note that the predicted and actual replies are highly consistent because the data points on the 45° line are uniformly dispersed. It seems that the cubic model has been successful in projecting the GPU core temperature, as demonstrated by the accompanying fan speed RPM. The results of a fitted regression model could be slightly biased by a small collection of data points known as low leverage data.

**Table 4.13** ANOVA outcome for the suggested quartic model of GPU Core Temperature on nickel thermal pad

| Source         | Sum of Squares | df | Mean Square | F Value | p-value Prob > F |                    |
|----------------|----------------|----|-------------|---------|------------------|--------------------|
| Model          | 943.93         | 4  | 235.98      | 2302.27 | 0.0004           | <b>Significant</b> |
| A-FANSPEED     | 12.37          | 1  | 12.37       | 120.70  | 0.0082           |                    |
| A <sup>2</sup> | 7.022E-003     | 1  | 7.022E-003  | 0.069   | 0.8180           |                    |
| A <sup>3</sup> | 13.57          | 1  | 13.57       | 132.36  | 0.0075           |                    |
| A <sup>4</sup> | 2.25           | 1  | 2.25        | 21.92   | 0.0427           |                    |
| Pure Error     | 0.20           | 2  | 0.10        |         |                  |                    |
| Cor Total      | 944.13         | 6  |             |         |                  |                    |

The graph in Figure 4.12 compares the expected and actual response levels. It might help you find a value or group of variables that are hard to model and predict. A very linear correlation with the actual core temperature is shown in Figure 4.12. The evenly distributed data points on the 45° line allow us to observe that the expected and actual responses are very compatible with one another. The fan speed RPM that comes with the GPU shows that the cubic model has predicted the core temperature. A tiny set of data points, called low leverage data, could somewhat skew the findings of a fitted regression model.

Design-Expert® Software  
GPU Core Temperature

Studentized residuals recommended

Color points by value of  
GPU Core Temperature:

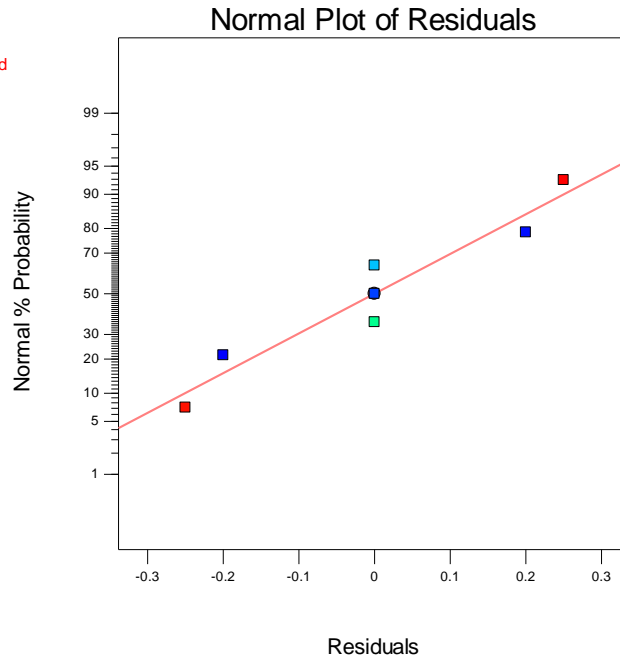


**Figure 4.16** Scatter plot of residuals versus residuals of a quartic model representing the relationship between GPU core temperature and nickel thermal pad.

After observing that the design expert couldn't compute all externally studentized residuals using the normal plot of residuals, the focus shifted to using the normal plot of residuals versus residuals. The plot revealed that the lines that produced the outlier crossed several times, with normal probabilities varying from 92.9 to 21.4%. Since there were no obvious anomalies or outliers, the number of minor observations was quite low. Because they were outliers, the low-leverage observations did not significantly complicate the regression process.

Design-Expert® Software  
GPU Core Temperature

Color points by value of  
GPU Core Temperature:

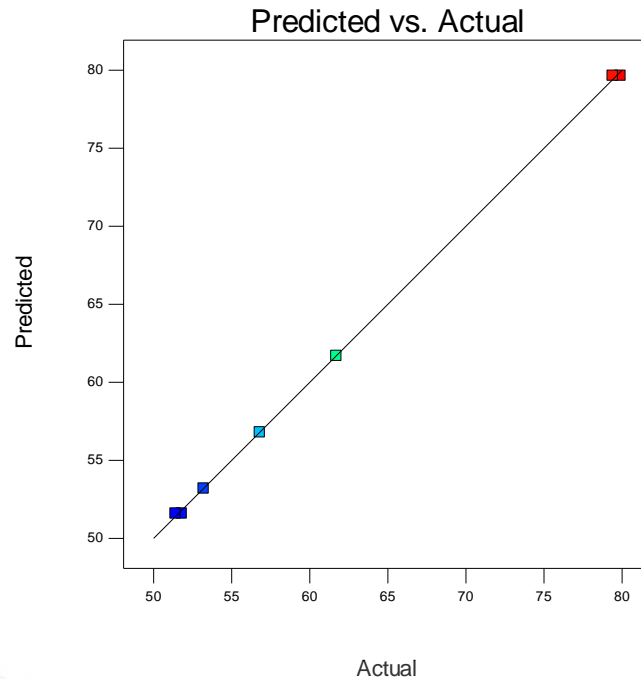


**Figure 4.17** Comparison of the quartic model's predicted and actual values for the temperature of GPU memory on a nickel thermal pad

Figure 4.17 displays a graph comparing the anticipated and observed levels of reaction. If you are encountering difficulties in forecasting a specific metric or dataset using a model, this tool can provide assistance. There is a high positive correlation between the actual core temperature and the curve shown in Figure 4.16. The data points exhibit a uniform distribution along the 45° line, indicating a high level of consistency between the expected and actual responses. The quartic model accurately predicted the GPU core temperature based on the associated fan speed RPM in this instance. The data shown above indicates that the quartic model is effective in exploring the design space of GPU core temperature.

Design-Expert® Software  
 Factor Coding: Actual  
 GPU Core Temperature (°C)  
 ● Design Points  
 --- 95% CI Bands  
 X1 = A: FANSPEED

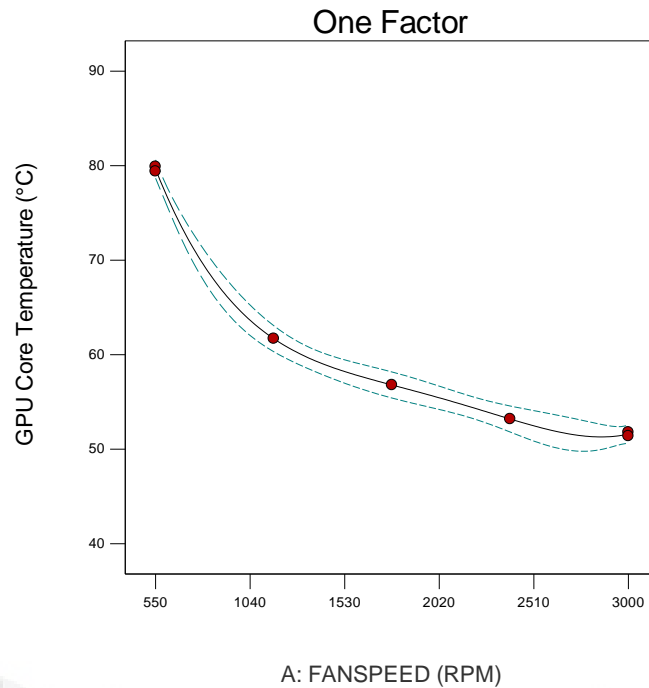


**Figure 4.18** Model Graph of quartic model of GPU Core Temperature on nickel thermal pad

The reaction surface plot of the GPU Core illustrates the relationship between temperature and fan speed. The average forecast at any specific GPU core temperature is accompanied by a 95% confidence interval, indicated by the dotted lines. Given that the fan speeds and GPU core temperatures remained below the specified limits, there is a 5% probability that this presumably precise model has made an error. The quartic model exhibited a smaller gap between the two dashed lines on the model graph, in contrast to the cubic model. These results demonstrate that the quartic model outperformed in forecasting the real GPU core temperature across various fan speeds. The most effective approach to optimising fan speed depending on GPU core temperature is by utilising the quartic model.

#### 4.2.2 Optimization of GPU memory temperature on nickel thermal pad via response surface-based Response Surface Methodology (RSM) with a single factor

**Table 4.14** Summary of statistical data on GPU memory temperature across different models using a nickel thermal pad.

| Source       | Sequential<br>p-value | Lack of Fit<br>p-value | Adjusted<br>R-Squared | Predicted<br>R-Squared |                         |
|--------------|-----------------------|------------------------|-----------------------|------------------------|-------------------------|
| Linear       | 0.0027                | 0.0025                 | 0.8306                | 0.7353                 |                         |
| Quadratic    | 0.0038                | 0.0168                 | 0.9789                | 0.9663                 |                         |
| <u>Cubic</u> | <u>0.0093</u>         | <u>0.1160</u>          | <u>0.9978</u>         | <u>0.9901</u>          | <b><u>Suggested</u></b> |
| Quartic      | 0.1160                |                        | 0.9993                |                        |                         |
| Fifth        |                       |                        |                       |                        | Aliased                 |

The cubic and quartic models, shown in Table 4.13, had the highest adjusted  $R^2$  values of 0.9978 and 0.9993, respectively. In addition, cubic models exhibit a predicted  $R^2$  value of 0.9901. Using these models to predict the response variable is the best choice since they provide the most exact fit with the data. The quadratic model demonstrates a notably high adjusted  $R^2$  value of 0.9789, ranking slightly below the cubic and quartic models. In contrast, the linear model reveals the lowest value. The fifth model lacks adjusted  $R^2$  or predicted  $R^2$  values due to aliasing. As a result of collinearity or other complicating factors, the attributed meaning cannot be differentiated from that of another model. Hence, this study will just investigate the cubic models.

**Table 4.15** ANOVA outcome for the suggested cubic model on GPU Memory Temperature

| Source             | Sum of Squares | df | Mean Square | F Value | p-value  |                    |
|--------------------|----------------|----|-------------|---------|----------|--------------------|
|                    |                |    |             |         | Prob > F |                    |
| Model              | 952.36         | 3  | 317.45      | 925.18  | < 0.0001 | <b>Significant</b> |
| A-FANSPEED         | 13.84          | 1  | 13.84       | 40.33   | 0.0079   |                    |
| A <sup>2</sup>     | 121.22         | 1  | 121.22      | 353.29  | 0.0003   |                    |
| A <sup>3</sup>     | 12.37          | 1  | 12.37       | 36.04   | 0.0093   |                    |
| Residual           | 1.03           | 3  | 0.34        |         |          |                    |
| <i>Lack of Fit</i> | 0.80           | 1  | 0.80        | 7.15    | 0.1160   | Not significant    |
| <i>Pure Error</i>  | 0.22           | 2  | 0.11        |         |          |                    |
| Cor Total          | 953.39         | 6  |             |         |          |                    |

Table 4.14 displays the results of the analysis of variance (ANOVA) for the cubic model that takes GPU core temperature into account. A statistical significance of 925.18 is demonstrated by the model. The odds of getting such a high F-value by pure chance are 0.0001%, which is extremely low. Given that FANSPEED's p-value is larger than A<sup>2</sup> and A<sup>3</sup>, it may be inferred that none of these factors significantly affect the result. When compared to the pure error, the "lack of fit F-value" of 7.15 indicates that the lack of fit does not warrant substantial consideration. A noise-induced lack of fit F-value of this magnitude is possible (11.60% likelihood). The p-values for the lack of fit terms are greater than 0.05; hence, they are not considered statistically significant. The statistical importance of the model terms is indicated by their p-values being less than 0.0001.

Design-Expert® Software  
GPU Memory Temperature

Color points by value of  
GPU Memory Temperature:

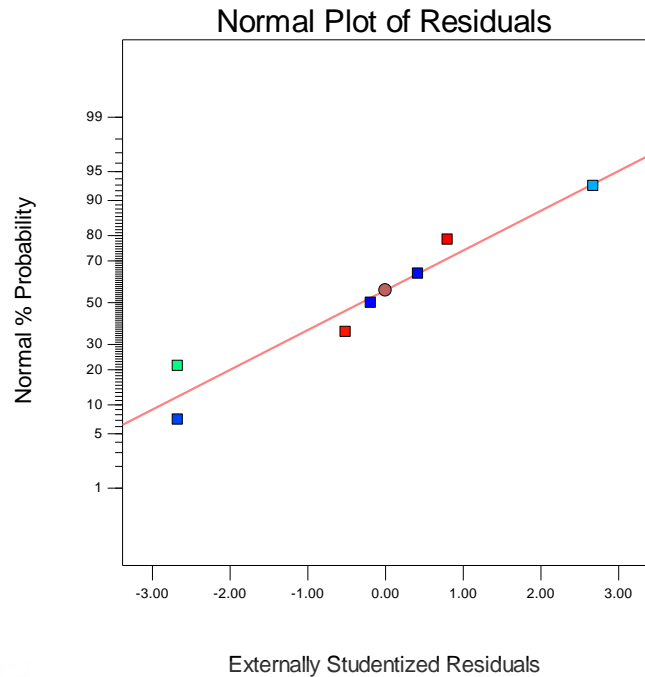


**Figure 4.19** The thermal nickel pad for normal plot of residuals versus externally standardised residuals of a cubic model of GPU memory temperature

In Figure 4.19, we can see that the residuals, when compared to the externally studentized residuals, follow a normal distribution. The usual distribution of the residuals is indicated by this. There were a handful of small but apparent outliers throughout the linear path. Although the low-leverage observations were unusual, they did not pose any serious problems for regression.

Design-Expert® Software  
GPU Memory Temperature  
Color points by value of  
GPU Memory Temperature:  
93  
64.4

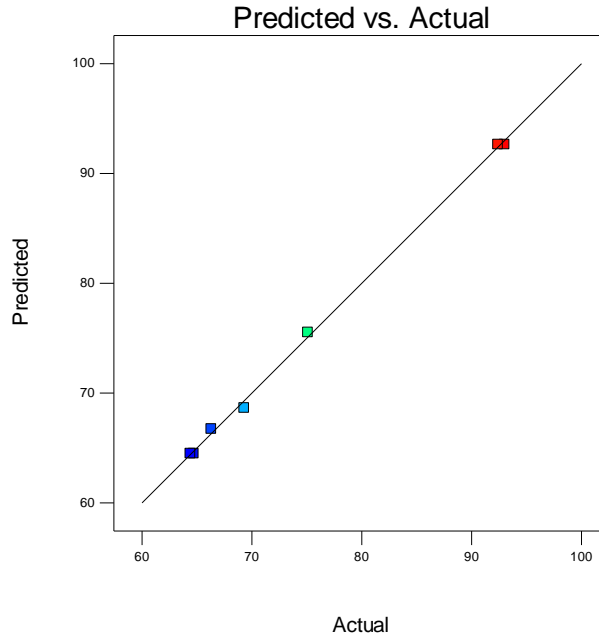


**Figure 4.20** Graph comparing the predicted values to the actual values of a cubic model representing the GPU memory temperature on a nickel thermal pad.

Graph 4.20 illustrates a comparison between the anticipated and observed levels of reaction. It can assist in identifying elusive or challenging-to-predict values or sets of variables that cannot be accurately forecasted using a model. The graph in Figure 4.20 exhibited a robust linear correlation with the actual temperature of the memory. The presence of a 45° line indicates a uniform distribution of data points, suggesting a close proximity between the expected and actual answers. The cubic model appears to have effectively predicted the GPU memory temperature in the nickel thermal pad, as seen by the corresponding fan speed RPM.

Design-Expert® Software  
 Factor Coding: Actual  
 GPU Memory Temperature (°C)  
 ● Design Points  
 ---- 95% CI Bands  
 X1 = A: FANSPEED

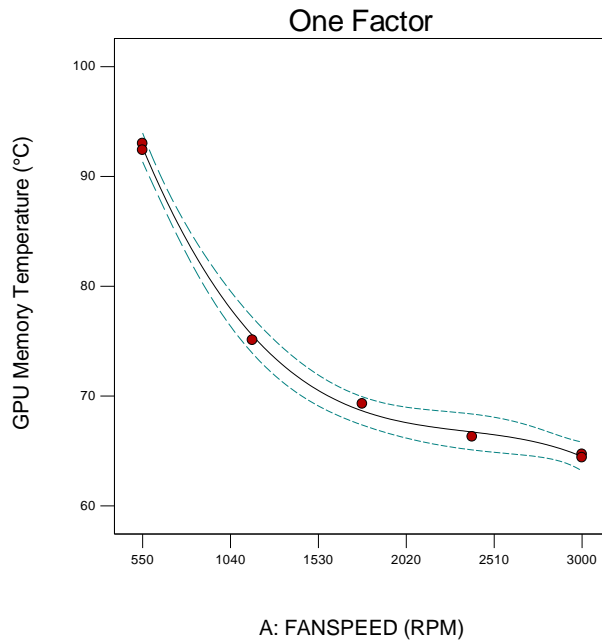


**Figure 4.21** Graphical representation of a cubic model of the temperature of GPU memory on a nickel thermal pad

The reaction surface map of the GPU memory temperature, as shown in Figure 4.21, reveals that the memory temperature changes in relation to the fan speed. For each GPU memory temperature, the dotted lines show the 95% confidence interval around the mean projection. With no outliers observed, this supposedly accurate model has a 5% margin of error because both the fan speeds and GPU memory temperatures fell within the prescribed range. According to the model graph, the average reaction temperature is within a 95% confidence interval of approximately 69.3 degrees Celsius.

### 4.3 Results of RSM analysis of copper thermal pad on GPU core and memory temperature

#### 4.3.1 Optimization of GPU Core Temperature on nickel thermal pad via response surface-based Response Surface Methodology (RSM) with a single factor

Based on the testing for variable fan speed under identical GPU load for copper thermal pad, it was required to run 7 times for quadratic model. The results of 7 run of experiments that had been done were shown in the table below:

**Table 4.16** Results of Design of Experiments for variable fan speed on copper thermal pad.

| Std. run no. | Run | Factor          | Response                |                           |
|--------------|-----|-----------------|-------------------------|---------------------------|
|              |     | Fan Speed (RPM) | GPU Core Temperature °C | GPU Memory Temperature °C |
| 7            | 1   | 1775            | 52.3                    | 64.3                      |
| 5            | 2   | 3000            | 48.4                    | 60.6                      |
| 2            | 3   | 550             | 77.4                    | 90.2                      |
| 4            | 4   | 2387.5          | 51.2                    | 63.3                      |
| 6            | 5   | 3000            | 48.9                    | 61.6                      |
| 1            | 6   | 550             | 77.2                    | 90.3                      |
| 3            | 7   | 1162.5          | 59.1                    | 71.7                      |

Based on the data shown in Table 4.15, it was seen that the temperatures of the GPU core and memory decreased gradually as the fan speed increased. A significant factor contributing to its significance in thermodynamics is that an increased fan speed would result in a higher velocity of air blowing across the GPU's heat sink, resulting in enhanced forced convection and a tangible augmentation in the rate of heat transfer. The core and memory saw their lowest temperatures at 3000 rpm, which corresponds to the highest fan speed. However, it was observed that the temperature of the GPU memory was far higher than that of the GPU core, indicating that the memory had produced a significantly larger amount of heat. Therefore, the component responsible for generating heat was the memory of the GPU. At a fan speed of 550 rpm, the memory reached a peak temperature of 90.3°C, which is

somewhat below both the original thermal pad and the nickel thermal pad. The copper thermal pad's superior thermal conductivity and minimal thermal contact resistance, compared to the original and nickel thermal pads, certainly contributed to this issue. When comparing the original and nickel thermal pads, the copper pad exhibited superior thermal contact resistance and higher thermal conductivity. This resulted in a more efficient transfer of heat from the GPU memory board. Furthermore, the most significant disparity in temperature was observed in the GPU core temperature, which decreased from 77.4°C to 59.1°C, resulting in a reduction of 18.3°C when the fan speed escalated from 550 rpm to 1162.5 rpm. The fan speed had a slight yet discernible impact on the temperature of the GPU memory. However, the temperature difference between the GPU memory and the fan speed range of 550 rpm to 1162.5 rpm was significantly greater, measuring at 18.6°C. Between 2387.5 rpm and 3000 rpm, the fan speed spectrum exhibited a minor decrease in temperature of around 2.3°C. Upon investigation, we discovered that raising the fan speed from 2387.5 rpm did not result in any discernible effect on the temperature alteration, indicating that the cooling capacity had hit its upper limit.

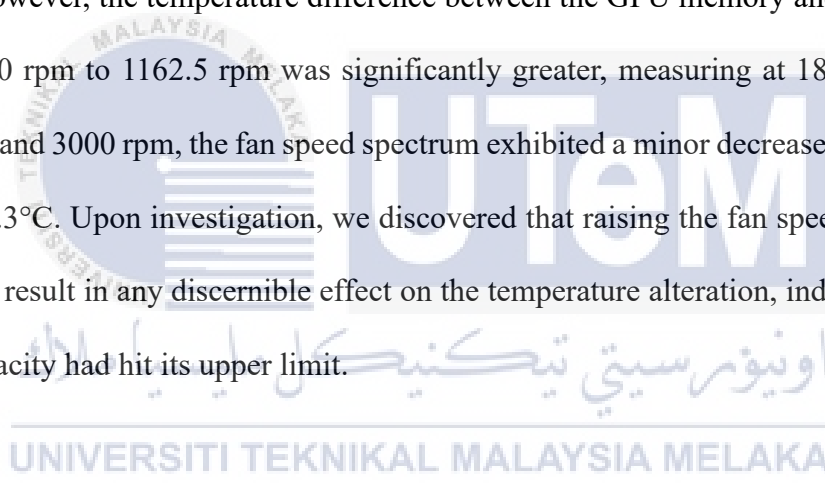


**Table 4.17** Model Evaluation of Quartic Order for GPU Core and Memory Temperature on copper thermal pad.

| <b>Term</b>    | <b>Std Error</b> | <b>VIF</b> | <b>Ri-Squared</b> | <b>2 Std. Dev.</b> |
|----------------|------------------|------------|-------------------|--------------------|
| A              | 1.89             | 16.13      | 0.9380            | 6.3 %              |
| A <sup>2</sup> | 6.26             | 48.36      | 0.9793            | 5.5 %              |
| A <sup>3</sup> | 2.00             | 16.13      | 0.9380            | 6.2 %              |
| A <sup>4</sup> | 5.54             | 48.36      | 0.9793            | 5.6 %              |

**Table 4.18** Summary of Statistics of various models for GPU Core Temperature on copper thermal pad

| Source       | Sequential<br>p-value | Lack of Fit<br>p-value | Adjusted<br>R-Squared | Predicted<br>R-Squared |                         |
|--------------|-----------------------|------------------------|-----------------------|------------------------|-------------------------|
| Linear       | 0.0036                | 0.0014                 | 0.8109                | 0.7094                 |                         |
| Quadratic    | 0.0055                | 0.0078                 | 0.9719                | 0.9561                 |                         |
| <u>Cubic</u> | <u>0.0004</u>         | <u>0.5833</u>          | <u>0.9996</u>         | <u>0.9991</u>          | <b><u>Suggested</u></b> |
| Quartic      | 0.5833                |                        | 0.9996                |                        |                         |
| Fifth        |                       |                        |                       |                        | Aliased                 |

According to the data presented in Table 4.17, the cubic and quartic models exhibit the greatest adjusted  $R^2$  values (0.9996) and a predicted  $R^2$  value of 0.9991, as indicated in the table. Consequently, these models are the most optimal choices for forecasting the response variable, as they offer the most accurate alignment with the data. The quartic and cubic models provide a remarkable adjusted  $R^2$  value of 0.9996, while the linear model demonstrates the lowest results with a value of 0.8109. The fifth model, which is designated as aliased, does not provide adjusted  $R^2$  or predicted  $R^2$  values. Due to collinearity or other complicating variables, the assigned meaning is indistinguishable from another model. Consequently, our research specifically concentrated on the cubic models.

**Table 4.19** ANOVA outcome for the suggested cubic model on GPU Core Temperature on copper thermal pad

| Source             | Sum of Squares | df | Mean Square | F Value | p-value  |                    |
|--------------------|----------------|----|-------------|---------|----------|--------------------|
|                    |                |    |             |         | Prob > F |                    |
| Model              | 989.41         | 3  | 329.80      | 5638.61 | < 0.0001 | <b>Significant</b> |
| A-FANSPEED         | 9.25           | 1  | 9.25        | 158.21  | 0.0011   |                    |
| A <sup>2</sup>     | 137.39         | 1  | 137.39      | 2348.86 | < 0.0001 |                    |
| A <sup>3</sup>     | 18.35          | 1  | 18.35       | 313.67  | 0.0004   |                    |
| Residual           | 0.18           | 3  | 0.058       |         |          |                    |
| <i>Lack of Fit</i> | 0.030          | 1  | 0.030       | 0.42    | 0.5833   | not significant    |
| <i>Pure Error</i>  | 0.15           | 2  | 0.073       |         |          |                    |
| Cor Total          | 989.59         | 6  |             |         |          |                    |

The ANOVA findings for the cubic model based on GPU core temperature on a copper thermal pad are presented in Table 4.18. The F-value of 5638.61 suggests that the model is statistically significant, as the probability of obtaining such a high F-value by chance alone is extremely low at 0.0001%. The F-values for FANSPEED are higher than those for lack of fit, suggesting that neither FANSPEED nor lack of fit have a substantial impact on the reaction. The p-values for the A<sup>2</sup> and A<sup>3</sup> components are below the threshold of 0.05, indicating that they lack statistical significance. The p-value for the model terms is less than 0.0001, indicating that it is a statistically significant term.

Design-Expert® Software  
GPU Core Temperature

Color points by value of  
GPU Core Temperature:

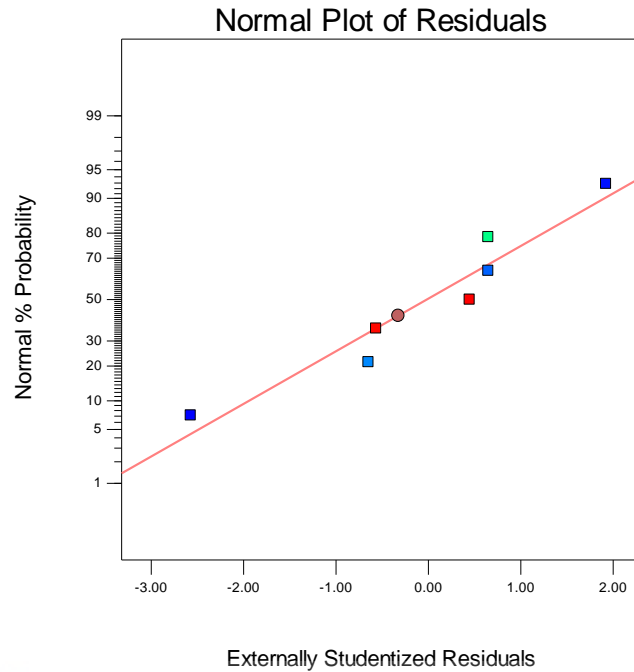


**Figure 4.22** Normal Plot of Residuals against Externally Studentized Residuals of Cubic model of GPU Core Temperature on copper thermal pad

The residuals appear to follow a normal distribution, as they are connected to the points in the normal plot of externally studentized residuals by a straight line. A handful of extreme values were clearly visible along the straight line. Because the low leverage observations were an aberration, regression did not encounter any major challenges.

Design-Expert® Software  
GPU Core Temperature

Color points by value of  
GPU Core Temperature:

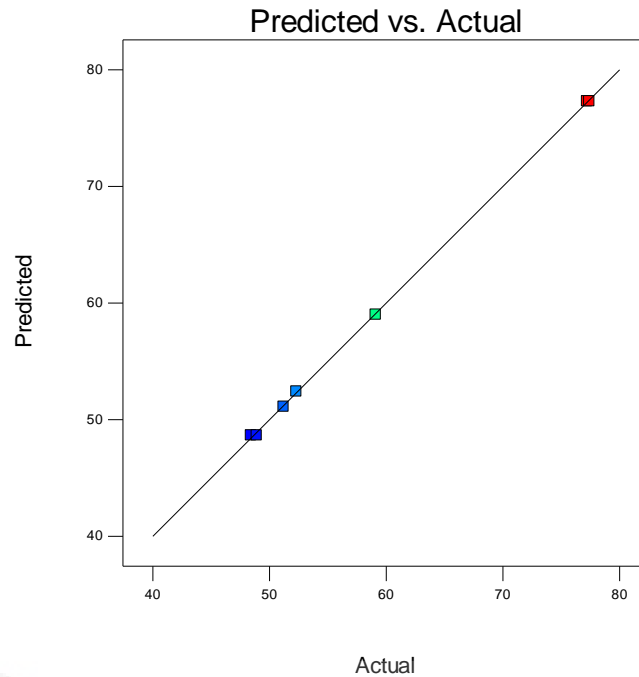


**Figure 4.23** Graph of Predicted against Actual of cubic model of GPU Core Temperature on copper thermal pad.

A graph comparing the expected and actual levels of response is shown in Figure 4.23. The real core temperature and the curve in Figure 4.23 are highly correlated. The data points are evenly distributed along the 45° line, showing that the expected and actual responses are very consistent. In this case, the GPU core temperature was precisely predicted by the cubic model using the appropriate fan speed RPM. The data presented above supports the idea that the cubic model works well for investigating GPU core temperature design space.

Design-Expert® Software  
 Factor Coding: Actual  
 GPU Core Temperature (°C)  
 ● Design Points  
 --- 95% CI Bands  
 X1 = A: FANSPEED

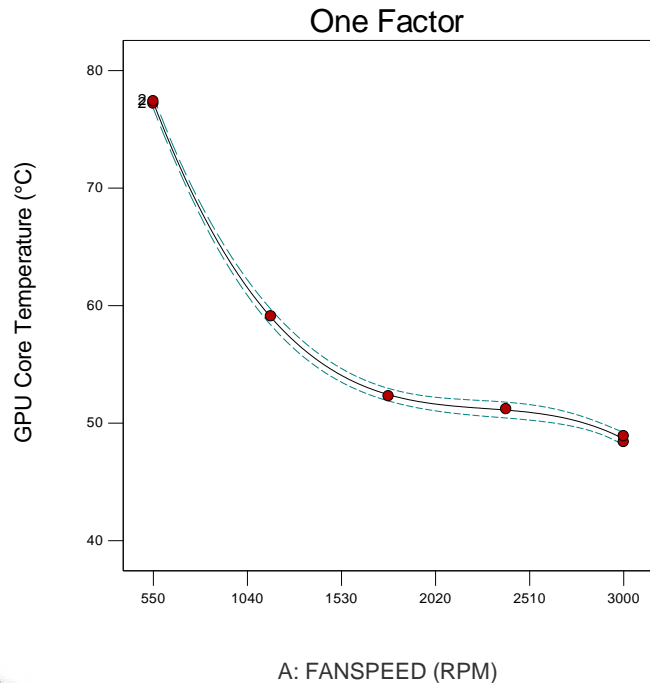


**Figure 4.24** Graph depicting the cubic model of GPU core temperature on a copper thermal pad.

The reaction surface plot of the GPU Core illustrates the correlation between the temperature and the speed of the fan. The dashed lines depict the 95% confidence interval for the average forecasted value at a specific GPU core temperature. As observed, the fan speeds and accompanying GPU core temperatures consistently stayed within the limits indicated by the dotted lines. This indicates that there is a 5% probability of making an incorrect decision using this presumably accurate model. Based on the presented model graph, it is apparent that the gap between the two dotted lines is tightly connected, indicating a negligible margin of error. These findings indicate that the cubic model exhibited the lowest level of inaccuracy when predicting the actual GPU core temperature under varying fan speeds. Hence, the cubic model is the most suitable option for improving fan speed.

### 4.3.2 Optimization of GPU memory temperature on copper thermal pad via response surface-based Response Surface Methodology (RSM) with a single factor

**Table 4.20** Summary of statistical data on GPU memory temperature across different models using a copper thermal pad.

| Source       | Sequential<br>p-value | Lack of Fit<br>p-value | Adjusted<br>R-Squared | Predicted<br>R-Squared |                         |
|--------------|-----------------------|------------------------|-----------------------|------------------------|-------------------------|
| Linear       | 0.0040                | 0.0044                 | 0.8028                | 0.6966                 |                         |
| Quadratic    | 0.0041                | 0.0287                 | 0.9746                | 0.9598                 |                         |
| <u>Cubic</u> | <u>0.0029</u>         | <u>0.5652</u>          | <u>0.9988</u>         | <u>0.9969</u>          | <b><u>Suggested</u></b> |
| Quartic      | 0.5652                |                        | 0.9985                |                        |                         |
| Fifth        |                       |                        |                       |                        | Aliased                 |

The cubic and quartic models, as displayed in Table 4.19, exhibited the highest adjusted  $R^2$  values of 0.9988 and 0.9985, respectively. Furthermore, cubic models demonstrate a forecasted  $R^2$  value of 0.9969. Utilising these models for predicting the response variable is the optimal decision since they offer the most precise alignment with the data. The quadratic model exhibits a significantly high adjusted  $R^2$  value of 0.9746, which places it somewhat lower than the cubic and quartic models. Conversely, the linear model indicates the minimum value. The fifth model does not have modified  $R^2$  or anticipated  $R^2$  values because of aliasing. Due to collinearity or other complicating circumstances, it is not possible to distinguish the attributed meaning from that of another model. Therefore, this study will solely examine the cubic models.

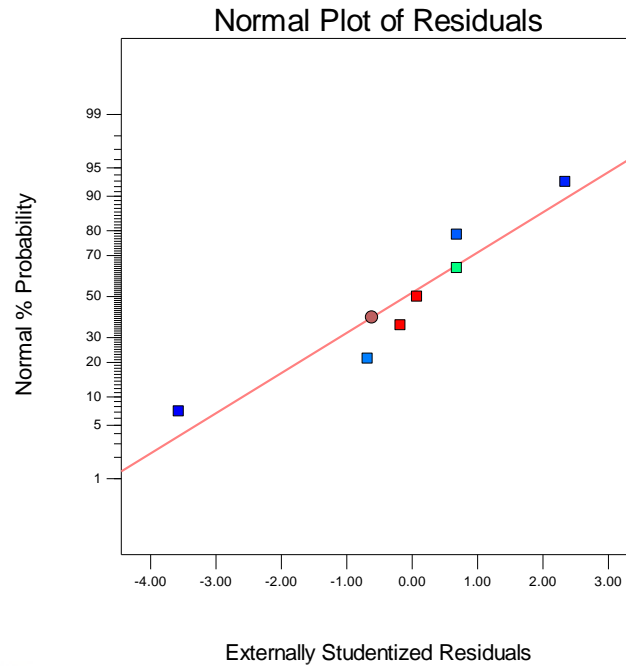
**Table 4.21** ANOVA outcome for the suggested cubic model on GPU Memory Temperature

| Source             | Sum of Squares | df | Mean Square | F Value | p-value  |                    |
|--------------------|----------------|----|-------------|---------|----------|--------------------|
|                    |                |    |             |         | Prob > F |                    |
| Model              | 1038.13        | 3  | 346.04      | 1667.09 | < 0.0001 | <b>Significant</b> |
| A-FANSPEED         | 11.22          | 1  | 11.22       | 54.07   | 0.0052   |                    |
| A <sup>2</sup>     | 153.12         | 1  | 153.12      | 737.69  | 0.0001   |                    |
| A <sup>3</sup>     | 16.95          | 1  | 16.95       | 81.64   | 0.0029   |                    |
| Residual           | 0.62           | 3  | 0.21        |         |          |                    |
| <i>Lack of Fit</i> | 0.12           | 1  | 0.12        | 0.47    | 0.5652   | Not significant    |
| <i>Pure Error</i>  | 0.50           | 2  | 0.25        |         |          |                    |
| Cor Total          | 1038.75        | 6  |             |         |          |                    |

The ANOVA findings for the cubic model, which include GPU memory temperature, are presented in Table 4.20. The model demonstrates a statistical significance of 1038.13. The probability of obtaining such a high F-value by random chance is 0.0001%, indicating an exceedingly low likelihood. Since the p-value of FANSPEED is greater than that of A2 and A3, it may be concluded that none of these parameters have a significant impact on the outcome. The "lack of fit F-value" of 0.47 suggests that the lack of fit is not significant enough to be given serious consideration as compared to the pure error. It is feasible to have a noise-induced lack of fit F-value of this magnitude with a likelihood of 56.52%. The p-values for the lack of fit terms exceed 0.05, indicating that they are not statistically significant. The model terms are considered statistically significant if their p-values are less than 0.0001.

Design-Expert® Software  
GPU Memory Temperature

Color points by value of  
GPU Memory Temperature:



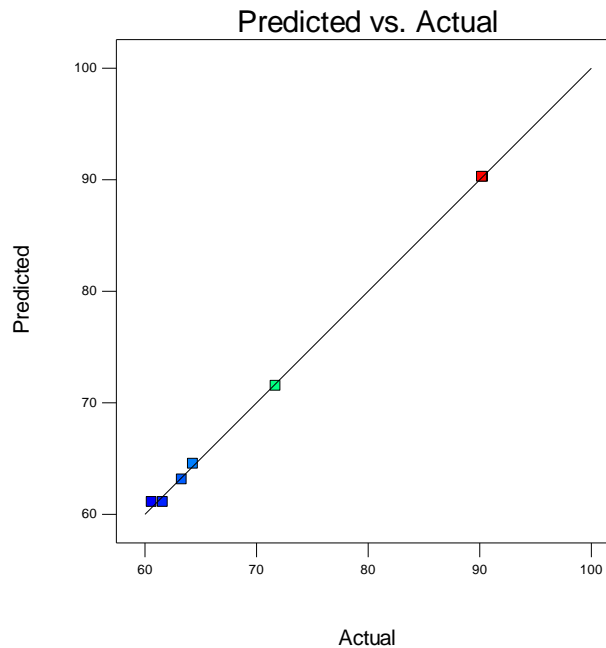
**Figure 4.25** The thermal copper pad for normal plot of residuals versus externally standardised residuals of a cubic model of GPU memory temperature

Figure 4.25 demonstrates that the residuals comply with a normal distribution when compared to the externally studentized residuals. This is indicative of the typical distribution of the residuals. Several modest but noticeable outliers were present along the linear course. While the low-leverage observations were atypical, they did not provide any significant issues for regression.

Design-Expert® Software  
 GPU Memory Temperature

Color points by value of  
 GPU Memory Temperature:

90.3  
 60.6



**Figure 4.26** Graph comparing the predicted values to the actual values of a cubic model representing the GPU memory temperature on a copper thermal pad.

Figure 4.26 depicts a comparison between the expected and actual levels of response. It can help find elusive or difficult-to-predict values or groupings of variables that cannot be successfully projected using a model. The graph displayed in Figure 4.26 demonstrated a strong linear association with the true temperature of the memory. A 45° line on the graph signifies a homogeneous distribution of data points, implying a strong correlation between the predicted and observed values. The cubic model accurately forecasted the GPU memory temperature in the copper thermal pad, as seen by the associated fan speed RPM.

Design-Expert® Software  
 Factor Coding: Actual  
 GPU Memory Temperature (°C)  
 ● Design Points  
 --- 95% CI Bands  
 X1 = A: FANSPEED

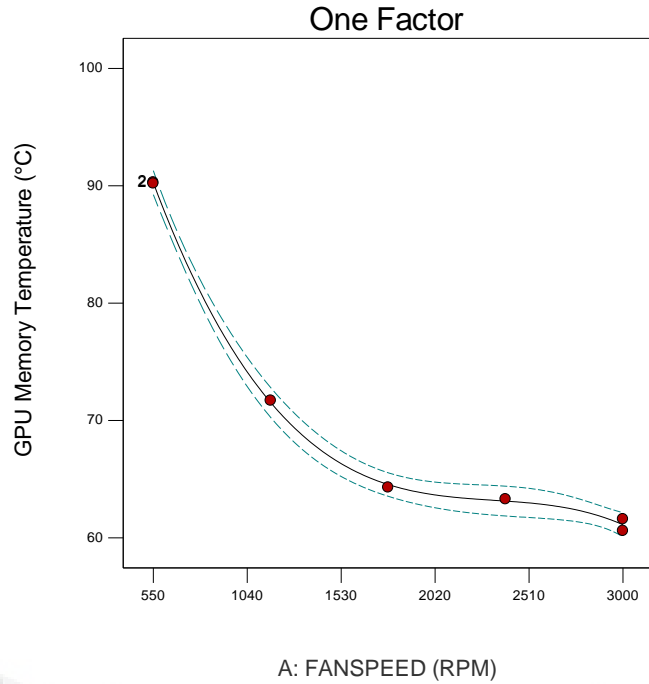


**Figure 4.27** Graphical representation of a cubic model of the temperature of GPU memory on a copper thermal pad

Figure 4.27 displays a reaction surface map illustrating the correlation between the fan speed and the temperature of the GPU memory. It demonstrates that the memory temperature fluctuates in response to variations in fan speed. The 95% confidence interval around the mean projection is represented by the dotted lines for each GPU memory temperature. Without any outliers, this purportedly precise model exhibits a 5% margin of error due to the fact that both the fan speeds and GPU memory temperatures were within the specified range. Based on the model graph, the mean reaction temperature falls within a 95% confidence interval of around 64.3 degrees Celsius.

**4.4 Discussion on the GPU core and memory temperature achieved by various thermal pad material.**

**GPU Core Temperature against variations of thermal pad**

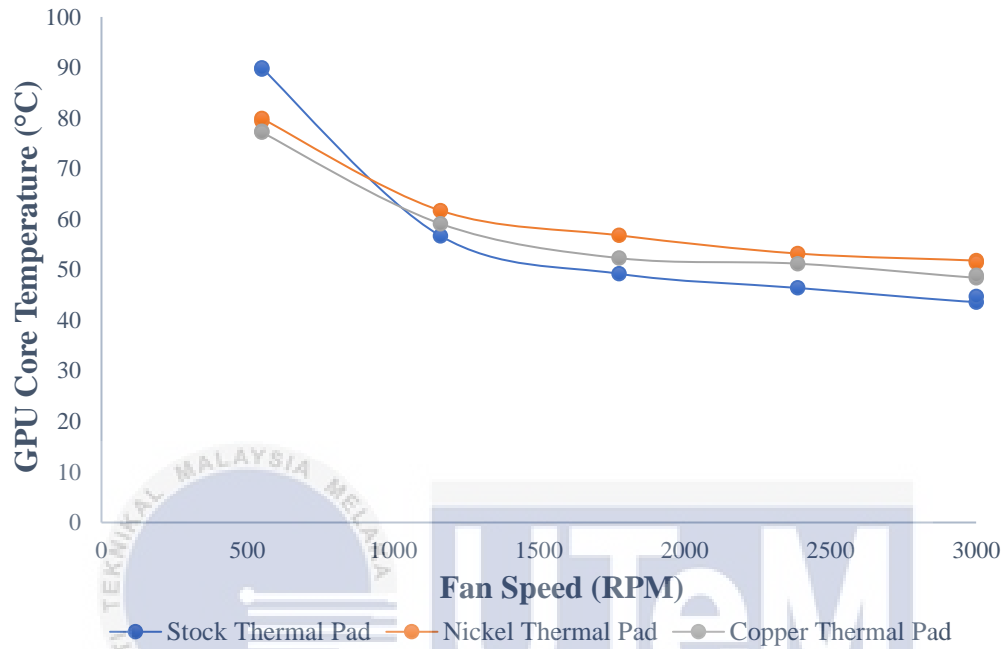


**Figure 4.28** Graph of GPU Core Temperature against variations of thermal pad.

**GPU Memory Temperature against variations of thermal pad**

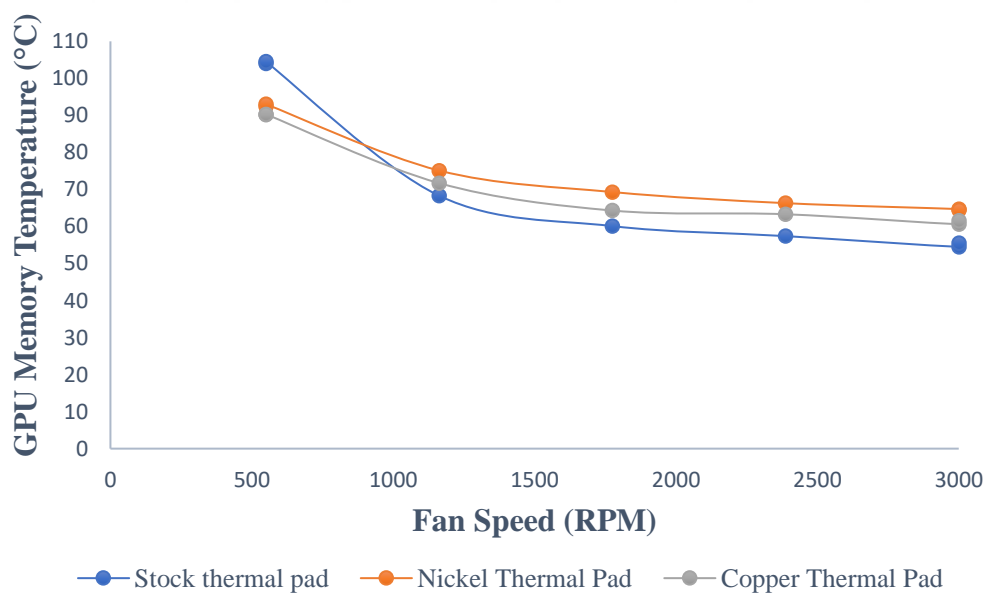


**Figure 4.29** Graph of GPU Memory Temperature against variations of thermal pad.

In theory, increasing the fan speed and wind velocity will result in improved cooling performance. Upon doing a comparative analysis of the three thermal pad variants on the GPU core temperature, it was observed that the conventional thermal pad had the highest temperature reading at a fan speed of 550 rpm. The nickel thermal pad and copper thermal pad exhibited lower temperatures in contrast. This phenomenon can be ascribed to the thermal pad's ability to withstand high temperatures, which is consistent across three distinct materials. The initial thermal pad has the most elevated thermal resistance, quantified at 0.1540 °C/W. When comparing the two, the nickel thermal pad exhibits a thermal resistance of 0.0042 °C/W, whilst the copper thermal pad has the lowest thermal resistance, measuring at 0.0010 °C/W. The copper thermal pad achieved the lowest temperature when the fan speed was set at 550 rpm, making this explanation the most lucid. The copper thermal pad exhibits the most minimal thermal resistance, facilitating effective transmission of heat to the heat sink of the GPU. Upon comparing the rates at which heat is dissipated by copper, nickel, and stock thermal pads, it was determined that the copper thermal pad exhibited the highest rate. Despite operating at a low fan speed and with limited air flow, the copper thermal pad successfully lowered the core temperature to 77.2°C. In contrast, thermal pads designed for stocks achieve their peak core temperature at 89.7 °C.

The increase in fan speed, ranging from 1162.5 rpm to 2387.5 rpm, significantly reduced the GPU core temperature. Nevertheless, by progressively raising the fan speed from 1162.5 rpm to 2387.5 rpm, the thermal pad provided with the product achieved the lowest temperature for the GPU core. These circumstances can be attributed to the inherent heat capacity of materials. The stock thermal pad is made of silicone, which has a heat capacity of 1300 J/kg (Blinzler et al., 2020). In comparison, nickel has a heat capacity of 445 J/KgK (“Specific Heat for all the elements in the Periodic Table,” n.d.), while copper has a heat capacity of 385 J/KgK (“Specific heat capacity,” n.d.). The heat capacity of a material

is defined as the amount of heat energy required to increase its temperature by 1°C. Therefore, in this scenario, even if the fan speed remains constant, the stock thermal pad can exhibit the lowest temperature. This is because it has the capacity to retain more heat energy before its temperature increases, as compared to the nickel and copper thermal pads. Even though nickel and copper thermal pads had better yet higher thermal conductivity than stock thermal pad, however, due to its higher elastic modulus than stock thermal pad. Its solid metal body of nickel and copper thermal pad results to lesser actual contact area with GPU heat sink which cannot further enhance its heat transfer characteristics fully between the interfaces, in contrast, the softer stock thermal pads provide softer contact surface which enhance the thermal contact with GPU heat sink allows better heat transfer than nickel and copper thermal pad.

Apart from that, it is well known to us that thermal conductivity of the thermal pad will greatly influence the heat dissipation from chip to heat sink. As accordance to (Ren et al., 2023) who had done a numerical study on thermal pad, they found that the temperature of the chip sharply decreases with an increase in the thermal conductivity of the thermal pad, which shows that a higher thermal conductivity of the thermal pad will significantly enhance the heat dissipation. In our case, this statement validated on the 550 rpm fan speed where the copper thermal pad behaved the lowest temperature followed by nickel and the stock thermal pad at the last. This were due to their corresponding thermal conductivity of material itself, for copper thermal pad, it has thermal conductivity of 397.48 W/mK while 87.86 W/mK for nickel thermal pad followed by around 1 ~ 7 W/mK for the stock thermal pad. This scenario clearly explain why we could obtain a lowest temperature on copper thermal pad if comparing with nickel and stock thermal pad on 550 rpm fan speed.

#### 4.5 Verification and validation of GPU core and memory temperatures in accordance with the RSM mathematical model's optimised fan speed.

In order to ensure the accuracy of the selected mathematical expression, this subtopic will be utilised to validate and verify the actual GPU core and memory temperatures against the proposed GPU core and memory temperatures. The mathematical models that would be the focus in this scenario are the cubic and quartic models. A limited number of criteria would be used to evaluate the numerical optimisation, including selecting the minimum values for fan speed, core temperature, and memory temperature or falling within the acceptable ranges for each of these variables.

##### 4.5.1 Verification on GPU Core Temperature and memory temperature for stock thermal pad in accordance with the RSM mathematical model's optimised fan speed.

Based on the numerical optimization criteria, the optimization chosen were all minimize for fan speed, core and memory temperature. The table of constraints was shown in table below:

**Table 4.22** Table of constraints RSM numerical optimization

| <b>Name</b>            | <b>Goal</b> |
|------------------------|-------------|
| A: FANSPEED            | Minimize    |
| GPU Core Temperature   | Minimize    |
| GPU Memory Temperature | Minimize    |

**Table 4.23** Solutions proposed by RSM numerical optimization.

| <b>FANSPEED<br/>(RPM)</b> | <b>GPU Core<br/>Temperature<br/>(°C)</b> | <b>GPU Memory<br/>Temperature<br/>(°C)</b> | <b>Desirability</b> |
|---------------------------|--|--|---------------------|
| 1430.592                  | 51.885                                   | 63.001                                     | 0.759               |

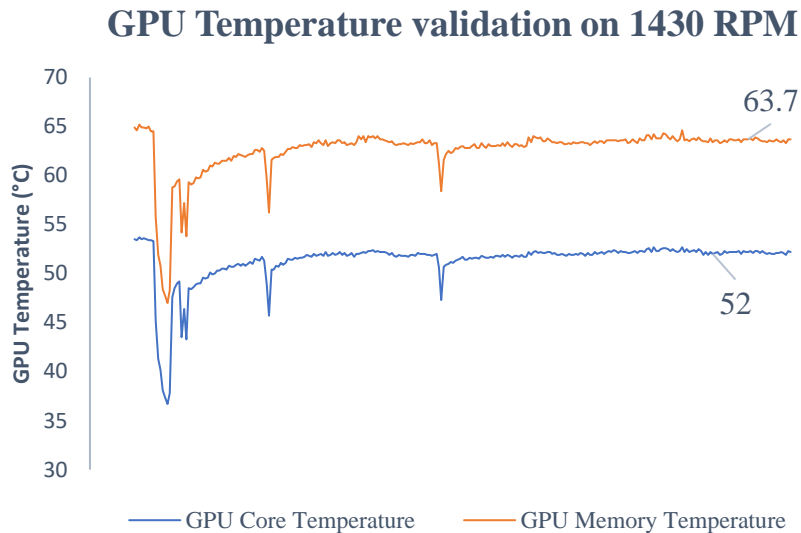


**Figure 4.30** Temperature validation on 1430 RPM on stock thermal pad

The analysis of the temperature versus time graph in Figure 4.30 revealed that the GPU memory temperature stabilised at 63.7°C, whereas the GPU core temperature attained 52°C. The mathematical model yielded a standard error of approximately 1.11% for GPU memory and 0.22% for GPU core temperature in the given scenario. It was evident that the quartic model had accurately predicted the temperature of the GPU core and memory; consequently, this model could be employed to optimise the temperature by utilising the recommended fan speed.

#### **4.5.2 Verification on GPU Core Temperature and memory temperature for nickel thermal pad in accordance with the RSM mathematical model's optimised fan speed.**

Based on the numerical optimization criteria, the optimization chosen were in range for fan speed and GPU core temperature while minimize for GPU memory temperature. The table of constraints was shown in table below:

**Table 4.24** Table of constraints RSM numerical optimization

| Name                   | Goal     |
|------------------------|----------|
| A: FANSPEED            | In-range |
| GPU Core Temperature   | In-range |
| GPU Memory Temperature | Minimize |

**Table 4.25** Solutions proposed by RSM numerical optimization.

| FANSPEED (RPM) | GPU Core Temperature (°C) | GPU Memory Temperature (°C) | Desirability |
|----------------|---------------------------|-----------------------------|--------------|
| 2979.046       | 51.514                    | 64.546                      | 0.995        |

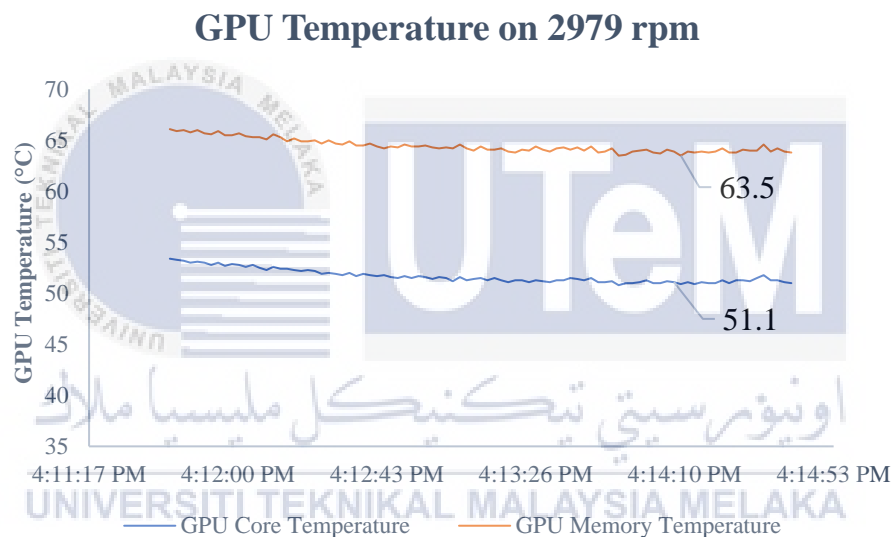


**Figure 4.31** Temperature validation on 2979 RPM on nickel thermal pad

Upon examining the temperature versus time graph depicted in Figure 4.31, it was determined that the GPU memory temperature reached a state of stability at 63.5°C, while the GPU core temperature peaked at 51.1°C. In the provided scenario, the mathematical model produced standard errors of around 1.62% and 0.80%, respectively, for GPU memory and GPU core temperature. The accuracy with which the quartic model predicted the GPU core and memory temperatures was readily apparent. As a result, this model could be used to optimise the temperature by implementing the suggested fan speed.

**4.5.3 Verification on GPU Core Temperature and memory temperature for copper thermal pad in accordance with the RSM mathematical model's optimised fan speed.**

Based on the numerical optimization criteria, the optimization chosen were in range GPU core temperature while minimize for fan speed and GPU memory temperature. The table of constraints was shown in table below:

**Table 4.26** Table of constraints RSM numerical optimization

| Name                   | Goal     |
|------------------------|----------|
| A: FANSPEED            | Minimize |
| GPU Core Temperature   | In-range |
| GPU Memory Temperature | Minimize |

**Table 4.27** Solutions proposed by RSM numerical optimization.

| FANSPEED (RPM) | GPU Core Temperature (°C) | GPU Memory Temperature (°C) | Desirability |
|----------------|---------------------------|-----------------------------|--------------|
| 1365.734       | 55.848                    | 68.218                      | 0.704        |

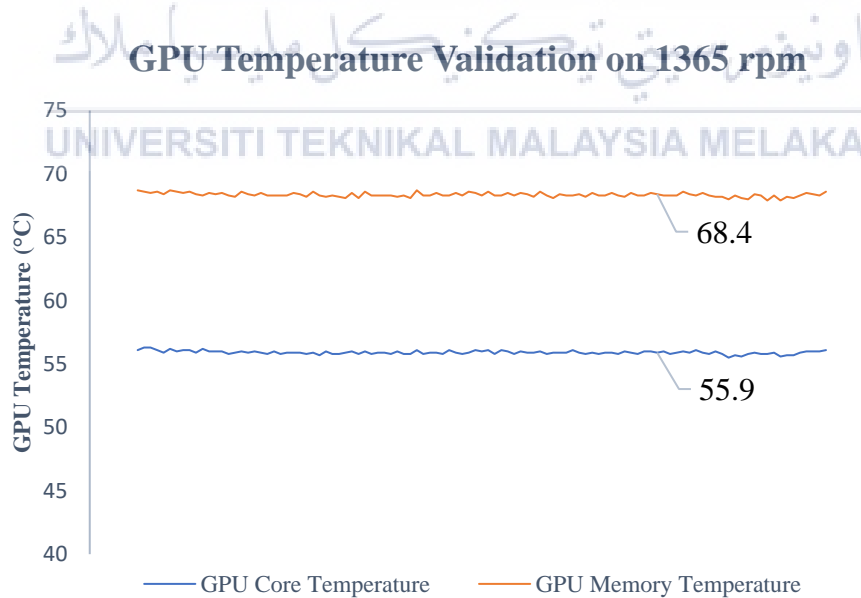


**Figure 4.32** Temperature validation on 1365 RPM on copper thermal pad

After analysing the temperature versus time graph illustrated in Figure 4.32, it was ascertained that the GPU core temperature peaked at 55.9°C, whereas the GPU memory temperature stabilised at 68.4°C. The mathematical model generated standard errors of approximately 0.27% and 0.093% for GPU memory and GPU core temperature, respectively, in the given scenario. It was immediately apparent that the quartic model accurately anticipated the temperatures of the GPU's core and memory. Thus, by implementing the recommended fan speed, this model could be utilised to optimise the temperature.



## CHAPTER 5

### CONCLUSION AND RECOMMENDATIONS

#### 5.1 Conclusions

Essentially, this study examined how changes in fan speed impact the behaviour of GPU temperature while the GPU is under the same level of load. This study involved applying GPU load to the GPU by utilising Dagger Hashimoto mining algorithms via the NiceHash Miner programme. The MSI Afterburner was employed to regulate the clock settings and fan speed of the GPU, while HWINFO 64 was utilised to monitor the temperature of the GPU's core and memory. Based on the collected data, it was discovered that increasing the fan speed has a substantial impact on the GPU temperature. This is because the increased air flow velocity to the GPU's heat sink enhances the rate of heat transfer between the heat sink and the GPU chips. However, it was observed that increasing the fan speed to 1162.5 rpm and beyond did not result in a substantial decrease in temperature compared to the increase in fan speed from 550 rpm to 1162.5 rpm. This can be attributed to the inherent cooling capability of the GPU system. For instance, when the fan speed of the stock thermal pad was decreased from 550 rpm to 1162.5 rpm, the temperature decreased by 33°C. However, when the fan speed was increased from 1162.5 rpm to the maximum speed of 3000 rpm, the temperature only decreased by approximately 12°C. If the ASUS TUF Gaming 3060 GPU were to be fully utilised, increasing the fan speed further would have a significant impact on heat dissipation performance.

Furthermore, it has been discovered that the elastic modulus of the thermal pad has a substantial impact on the actual contact area at the interface, which in turn impacts the heat

transfer of the sandwich structure between the thermal pad and the heat sink. (Ren et al., 2023) Therefore, the thermal pad made of stock material, which had a lower elastic modulus, exhibited a softer surface. This softness enabled a larger contact area between the thermal pad and the GPU heat sink, resulting in enhanced heat transfer compared to thermal pads made of nickel and copper. During this investigation, the RSM analysis proposed the use of cubic and quartic models through the Design Expert programme. To validate the results, we conducted additional experiments to evaluate if the required GPU core and memory temperatures could be achieved. According to the validation process, it was seen that the validation was successful, as the margin of error was found to be below 5%. This indicates that the mathematical model selection accurately predicted the GPU core and memory temperature based on the recommended fan speed. The study successfully accomplished its purpose by utilising RSM to input values and determine the appropriate fan speed required to attain the specified GPU core and memory temperature.

Regarding the impact of different thermal pad materials on the temperature of the GPU core and memory, it was observed that nickel and copper thermal pads exhibited lower temperatures compared to the stock thermal pad when the fan speed was set to low. This was attributed to the significant influence of their material properties on their heat dissipation performance. Increasing material thermal conductivity towards surface thermal resistivity is more effective, as it can enhance the convective heat transfer coefficient on the side of the heat sink. The experiment demonstrated that the copper thermal pad attained a temperature of 90°C, while the nickel thermal pad reached a slightly higher temperature of 93°C. In contrast, the stock thermal pad recorded the greatest temperature at 104°C. Although the heat capacity of the stock thermal pad, which is primarily composed of silicone rubber, is higher than that of nickel and copper, However, thermal conductivity plays a crucial role in the disposal of heat. Despite the copper thermal pad maintaining a higher temperature than the

stock thermal pad at high fan speed, Using a copper thermal pad on the GPU memory is still a beneficial choice for extreme applications such as gaming and cryptocurrency mining. It effectively lowers the memory temperature even when the fan speed is low, resulting in energy savings on the cooling system while still attaining a high hash rate.

## 5.2 Recommendations for future study

In this study, we conducted tests on three different materials, namely silicone rubber, nickel, and copper thermal pads, under the same GPU load. It was discovered that materials with higher thermal conductivity, such as nickel and copper, and lower thermal resistance can effectively reduce the temperature of the GPU. However, the thermal pads made of nickel and copper have a lower heat capacity compared to the stock thermal pad. As a result, they exhibit slightly higher temperatures than the stock thermal pad when the fan speed is increased. This is due to their characteristic of heating up more quickly than the stock thermal pad. Additionally, it was discovered that the solid thermal pad had inferior thermal contact compared to the softer stock thermal pad, resulting in improved thermal contact and a higher rate of heat transfer.

In this scenario, I recommend conducting a replicated test on the thermal dissipation performance of GPU thermal pads using higher-ranked GPUs such as the RTX 3080, RTX 3090, or the latest Nvidia graphic cards like the RTX 4070 and RTX 4090. I assert this because the aforementioned graphic cards have allocated a higher memory bandwidth, indicating a greater number of memory chips compared to the ASUS TUF Gaming 3060. Consequently, this leads to more heat generation. Therefore, it is ideal to verify the efficacy of these materials in extracting memory chips from the GPU. Additionally, I propose conducting the tests by utilising alternative mining algorithms such as KAWPOW, Autolykos, and others.

## REFERENCES

- A.B. Etemoglu, A brief survey and economical analysis of air cooling for electronic equipments, *Int. Commun. Heat Mass Transf.* 34 (2007) 103–113, <https://doi.org/10.1016/j.icheatmasstransfer.2006.08.005>
- A.H. Shourideha, W.B. Ajrama, J.A. Lamia, S. Haggaga, A. Mansouri, A comprehensive study of an atmospheric water generator using Peltier effect, *Therm. Sci. Eng. Prog.* 6 (2018) 14–26, <https://doi.org/10.1016/j.tsep.2018.02.015>.
- Al-Rashed, A. A., Shahsavari, A., Entezari, S., Moghimi, M., Adio, S., & Nguyen, T. K. (2019, June). Numerical investigation of non-Newtonian water-CMC/CuO nanofluid flow in an offset strip-fin microchannel heat sink: Thermal performance and thermodynamic considerations. *Applied Thermal Engineering*, 155, 247–258. <https://doi.org/10.1016/j.applthermaleng.2019.04.009>
- Arctic MX-4 vs MX-5 vs MX-6 Thermal Paste Review Handling and Workability. (n.d.). [https://www.ocinside.de/review/arctic\\_mx4\\_mx5\\_mx6/4/](https://www.ocinside.de/review/arctic_mx4_mx5_mx6/4/)
- Bahraei, M., Heshmatian, S., & Keshavarzi, M. (2018, October). Multi-attribute optimization of a novel micro liquid block working with green graphene nanofluid regarding preferences of decision maker. *Applied Thermal Engineering*, 143, 11–21. <https://doi.org/10.1016/j.applthermaleng.2018.07.074>
- Balaji, T., Selvam, C., Lal, D. M., & Harish, S. (2020, October). Enhanced heat transport behavior of micro channel heat sink with graphene based nanofluids. *International Communications in Heat and Mass Transfer*, 117, 104716. <https://doi.org/10.1016/j.icheatmasstransfer.2020.104716>
- Bejan. 2013. *Convection Heat Transfer*. Ed. John Wiley & Sons.

- Blinzler, B.J., Khalili, P., Ahlström, J., 2020. Integrated Computational Material Design for PMC Manufacturing with Trapped Rubber. *Materials* 13, 3825. <https://doi.org/10.3390/ma13173825>
- Borode, A., & Olubambi, P. (2023, August). Modelling the effects of mixing ratio and temperature on the thermal conductivity of GNP-Alumina hybrid nanofluids: A comparison of ANN, RSM, and linear regression methods. *Heliyon*, 9(8), e19228. <https://doi.org/10.1016/j.heliyon.2023.e19228>
- C. Nadjahi, H. Louahlia, S. Lemasson, A review of thermal management and innovative cooling strategies for data center, *Sustainable Computing: Informatics and Systems*,2018,19:14-28
- Chamber, M. (2022, January 1). RTX 3060 Mining Settings. Mining Chamber. <https://www.miningchamber.com/gpus/rtx-3060/mining-settings>
- Chinta, V. S., Ravinder Reddy, P., & Prasad, K. E. (2022). The effect of stacking sequence on the tensile properties of jute fibre reinforced hybrid composite material for axial flow fan blades: An experimental and finite element investigation. *Materials Today: Proceedings*, 59, 747–755. <https://doi.org/10.1016/j.matpr.2021.12.500>
- Cuttler, P. C. P. R. S. J. I. C. A. C. D. C. L. A. C. (n.d.). 9.1 Setting Up a Factorial Experiment – Research Methods in Psychology. <https://opentext.wsu.edu/carriecuttler/chapter/9-1-setting-up-a-factorial-experiment/>
- Design-Expert | Stat-Ease. (n.d.). <https://www.statease.com/software/design-expert/>
- Electronics, A. (2023). Active vs passive cooling: Thermal management of electronic devices. Arrow.com. <https://www.arrow.com/en/research-and-events/articles/thermal-management-of-electronics-active-vs-passive-cooling>
- Elumalai, R., & Ravi, K. (2023, September). A hybrid calibration scheme for developing hydrogen enrichment ratio control map using RSM and ANN technique to enhance the

characteristics of an ammonia biodiesel RCCI combustion engine. *Case Studies in Thermal Engineering*, 49, 103257. <https://doi.org/10.1016/j.csite.2023.103257>

Etchash Algorithm Coins - Mining Calculator and Hashrate Distribution for Etchash. (n.d.). 2CryptoCalc. <https://2cryptocalc.com/etchash-algorithm>

F. Ino, "The Past, Present, and Future of GPU-Accelerated Grid Computing," 2013 First International Symposium on Computing and Networking, Matsuyama, Japan, 2013, pp. 17-21, doi: 10.1109/CANDAR.2013.10.

F. Meng, L. Chen, Z. Xie, Y. Ge, Thermoelectric generator with air-cooling heat recovery device from wastewater, *Therm. Sci. Eng. Prog.* 4 (2017) 106–112, <https://doi.org/10.1016/j.tsep.2017.09.008>.

Frankenfield, J. (2021). *What Is a Graphics Processing Unit (GPU)? Definition and Examples*. Investopedia. <https://www.investopedia.com/terms/g/graphics-processing-unit-gpu.asp>

Frankenfield, J. (2023, May 31). Ethereum Classic (ETC) Definition, History, Future. Investopedia. <https://www.investopedia.com/terms/e/ethereum-classic.asp>

Gunnasegaran, P., Abdullah, M. Z., Yusoff, M. Z., & Kanna, R. (2017, September 13). Heat Transfer in a Loop Heat Pipe using Diamond-H<sub>2</sub>O Nanofluid. *Heat Transfer Engineering*, 39(13–14), 1117–1131. <https://doi.org/10.1080/01457632.2017.1363616>

H.R. Liu, B.J. Li, L.J. Hua, et al., Designing thermoelectric self-cooling system for electronic devices: experimental investigation and model validation, *Energy* (2022) 243, doi: 10.1016/j.energy.2021.123059 .

Harun, M. A., & Che Sidik, N. A. (2020, December 10). A Review on Development of Liquid Cooling System for Central Processing Unit (CPU). *Journal of Advanced Research in Fluid Mechanics and Thermal Sciences*, 78(2), 98–113. <https://doi.org/10.37934/arfmts.78.2.98113>

Hasan, Husam Abdulrasool, Zainab Alquziweeni, and Kamaruzzaman Sopian. "Heat Transfer Enhancement Using Nanofluids For Cooling A Central Processing Unit (CPU) System." *Journal of Advanced Research in Fluid Mechanics and Thermal Sciences* 51, no. 2 (2018): 145-157

He, W., Zhang, J., Guo, R., Pei, C., Li, H., Liu, S., Wei, J., & Wang, Y. (2022, December). Performance analysis and structural optimization of a finned liquid-cooling radiator for chip heat dissipation. *Applied Energy*, 327, 120048. <https://doi.org/10.1016/j.apenergy.2022.120048>

Hong, E. (2023, October 18). How Does Bitcoin Mining Work? Investopedia. <https://www.investopedia.com/tech/how-does-bitcoin-mining-work/#citation-12>

I. Sauciuc, R. Prasher, J. Chang, H. Erturk, G. Chrysler, C. Chiu, R. Mahajan, Thermal performance and key challenges for future CPU cooling, IPACK2005, 17–22 July 2005, San Francisco, USA, 2005, <https://doi.org/10.1115/IPACK2005-73242>

Interpret the key results for Analyze Response Surface Design - Minitab. (n.d.). (C) Minitab, LLC. All Rights Reserved. 2023. <https://support.minitab.com/en-us/minitab/21/help-and-how-to/statistical-modeling/doe/how-to/response-surface/analyze-response-surface-design/interpret-the-results/key-results/>

J. (2016, December 6). Don't confuse Mixture DOE with Factorial DOE and RSM -. SQT Training. <https://www.sqt-training.com/2016/11/dont-confuse-mixture-doe-factorial-doe-rsm/>

J. Seymour, R. Cray, Immersion Cooled High Density Electronic Assembly, United States, 1986, Patent 4590538

J.V. Es, H.V. Gerner, Benefits and drawbacks of using two-phase cooling technologies in military platforms, *Electron. Cooling* 19 (1) (2013) (accessed 3 December,2018),

<https://www.electronics-cooling.com/2013/03/benefits-and-drawbacks-of-using-two-phase-cooling-technologies-in-military-platforms/#>.

KAWPOW Algorithm Coins - Mining Calculator and Hashrate Distribution for KAWPOW.

(n.d.). 2CryptoCalc. <https://2cryptocalc.com/kawpow-algorithm>

Leach, T.T. & Cadou, C.P. 2005. The role of structural heat exchange and heat loss in the design of efficient silicon micro-combustors. *Proceedings of the Combustion institute* 30(2): 2437-44.

Maheshwari, R. (2023, June 30). What Are Crypto Exchanges And How Do They Work. Forbes Advisor INDIA. <https://www.forbes.com/advisor/in/investing/cryptocurrency/what-is-a-crypto-exchange/>

Mathematics Learning Support Centre. (2007). Design Expert 7: Introduction. Design Expert 7: Introduction. Retrieved November 14, 2023, from <https://www.lboro.ac.uk/media/media/schoolanddepartments/mlsc/downloads/Design-Expert-7.pdf>

Mehrali, M., Sadeghinezhad, E., Latibari, S. T., Kazi, S. N., Mehrali, M., Zubir, M. N. B. M., & Metselaar, H. S. C. (2014, January 13). Investigation of thermal conductivity and rheological properties of nanofluids containing graphene nanoplatelets. *Nanoscale Research Letters*, 9(1). <https://doi.org/10.1186/1556-276x-9-15>

Misic, Marko & Đurđević, Đorđe & Tomasevic, Milo. (2012). Evolution and trends in GPU computing. 289-294.

Mixture Design. (2023, July 21). Benchmark Six Sigma Forum. <https://www.benchmarksixsigma.com/forum/topic/39484-mixture-design/>

Mohammed, Shilan & Muhammad, Shilan & Najat, Zryan & Saeed, Rezgar & Ageed, Zainab. (2021). GPU Concepts and Graph Application Challenges: A Review. 52-57.

Moore-Colyer, R., & T. (2022, October 19). Nvidia GeForce RTX 3090 vs 3080 vs 3070 vs 3060: Which GPU should you buy? Nvidia GeForce RTX 3090 Vs 3080 Vs 3070 Vs 3060: Which GPU Should You Buy? | Tom's Guide. <https://www.tomsguide.com/news/nvidia-geforce-rtx-comparison>

MX-4 | Premium Performance Thermal Paste | ARCTIC. (n.d.). ARCTIC GmbH. <https://www.arctic.de/en/MX-4/ACTCP00007B>

Narendra Babu, N., & Kamath, H. (2015). Materials used in Heat Pipe. *Materials Today: Proceedings*, 2(4–5), 1469–1478. <https://doi.org/10.1016/j.matpr.2015.07.072>

Nazari, M., Karami, M., & Ashouri, M. (2014, September). Comparing the thermal performance of water, Ethylene Glycol, Alumina and CNT nanofluids in CPU cooling: Experimental study. *Experimental Thermal and Fluid Science*, 57, 371–377. <https://doi.org/10.1016/j.expthermflusci.2014.06.003>

NiceHash - Leading Cryptocurrency Platform for Mining and Trading. (n.d.). <https://www.nicehash.com/support/general-help/nicehash-service/what-is-nicehash-and-how-it-works>

NiceHash - Leading Cryptocurrency Platform for Mining and Trading. (n.d.). <https://www.nicehash.com/blog/post/crypto-mining-algorithms-why-they-matter-and-how-they-work>

NiceHash - Leading Cryptocurrency Platform for Mining and Trading. (n.d.). [https://www.nicehash.com/blog/post/new-algorithm-autolykos-\(ergo\)-available-on-the-hashpower-marketplace](https://www.nicehash.com/blog/post/new-algorithm-autolykos-(ergo)-available-on-the-hashpower-marketplace)

Nordstokke, D., & Colp, S. M. (2014, January 1). *Factorial Design*. Springer eBooks. [https://doi.org/10.1007/978-94-007-0753-5\\_982](https://doi.org/10.1007/978-94-007-0753-5_982)

- Park, M., Lee, D. J., & Lee, H. (2022, February). Experimental and computational investigation of the effect of blade sweep on acoustic characteristics of axial fan. *Applied Acoustics*, 189, 108613. <https://doi.org/10.1016/j.apacoust.2021.108613>
- Paul Chambers. Heat Has a Negative Affect on Electronics | Element5 Digital. (2020, June 4). Retrieved from <https://element5digital.com/heat-has-a-negative-affect-on-electronics/>
- Publishing, R. (n.d.). Using Mixture Designs in DOE++. 2016. <https://www.weibull.com/hotwire/issue180/hottopics180.htm>
- Rafati, M., Hamidi, A., & Shariati Niaser, M. (2012, December). Application of nanofluids in computer cooling systems (heat transfer performance of nanofluids). *Applied Thermal Engineering*, 45–46, 9–14. <https://doi.org/10.1016/j.applthermaleng.2012.03.028>
- Ram, Jyothi. (2023). A Review on GPU Architectures and Programming.
- Ren, X.-J., Tang, Q.-F., Zhang, H., Zhang, J.-R., Du, M., Tao, W.-Q., 2023. Numerical study on the effect of thermal pad on enhancing interfacial heat transfer considering thermal contact resistance. *Case Studies in Thermal Engineering* 49, 103226. <https://doi.org/10.1016/j.csite.2023.103226>
- S.S. Khaleduzzaman, M.R. Sohel, R. Saidur, I.M. Mahbubul, I.M. Shahrul, B.A. Akash, J. Selvaraj, Energy and energy analysis of alumina-water nanofluid for an electronic liquid cooling system, *Int. Commun. Heat Mass Transf.* 57 (2014) 118–127, <https://doi.org/10.1016/j.icheatmasstransfer.2014.07.015>.
- Sarafraz, M., Arya, A., Hormozi, F., & Nikkhah, V. (2017, February). On the convective thermal performance of a CPU cooler working with liquid gallium and CuO/water nanofluid: A comparative study. *Applied Thermal Engineering*, 112, 1373–1381. <https://doi.org/10.1016/j.applthermaleng.2016.10.196>
- Siddique, A. R. M., Muresan, H., Majid, S. H., & Mahmud, S. (2019, May). An adjustable closed-loop liquid-based thermoelectric electronic cooling system for variable load thermal

management. *Thermal Science and Engineering Progress*, 10, 245–252.

<https://doi.org/10.1016/j.tsep.2019.02.004>

Siricharoenpanich, A., Wiriyasart, S., & Naphon, P. (2021, June). Study on the thermal dissipation performance of GPU cooling system with nanofluid as coolant. *Case Studies in Thermal Engineering*, 25, 100904. <https://doi.org/10.1016/j.csite.2021.100904>

Smith, J. (2022, May 11). How to Fully Unlock Nvidia LHR Graphics Cards with NBMiner: . . . Crypto Mining Blog. <https://2miners.com/blog/how-to-fully-unlock-nvidia-lhr-graphics-cards-with-nbminer-experiment-results/>

Smith, J.M. 1975. Introduction to Chemical Engineering Thermodynamics. Tesis Rensselaer Polytechnic Institute.

Specific Heat for all the elements in the Periodic Table [WWW Document], n.d. URL <https://periodictable.com/Properties/A/SpecificHeat.al.html>

Sun, B., & Liu, H. (2017, March). Flow and heat transfer characteristics of nanofluids in a liquid-cooled CPU heat radiator. *Applied Thermal Engineering*, 115, 435–443. <https://doi.org/10.1016/j.applthermaleng.2016.12.108>

Sushma Chinta, V., Ravinder Reddy, P., & Eshwar Prasad, K. (2023, March). Investigation of shear properties of axial flow fan blade material with partial woven jute reinforcements. *Materials Today: Proceedings*. <https://doi.org/10.1016/j.matpr.2023.02.426>

Team, W. (2023, May 6). Factorial Design. WallStreetMojo. <https://www.wallstreetmojo.com/factorial-design/>

Tharwan, M. Y., & Hadidi, H. M. (2022, September). Experimental investigation on the thermal performance of a heat sink filled with PCM. *Alexandria Engineering Journal*, 61(9), 7045–7054. <https://doi.org/10.1016/j.aej.2021.12.045>

Thermal Conductivity Experiments – Resistance: Materials [WWW Document], 2021. .

Thermtest. URL <https://thermtest.com/thermal-resources/thermal-conductivity-experiments/variations-in-material>

Thermal Interfaces for CPUs and GPUs | ARCTIC [WWW Document], n.d. . ARCTIC GmbH. URL <https://www.arctic.de/en/products/cooling/thermal-interface/>

Thermal Pad - TP-3 | Premium Performance Thermal Pad | ARCTIC [WWW Document], n.d. . ARCTIC GmbH. URL <https://www.arctic.de/en/TP-3/ACTPD00054A>

Tyler, J.M., Sofrin, T.G., 1962. Axial Flow Compressor Noise Studies. SAE Technical Paper. <https://doi.org/10.4271/620532>.

Wang, J. C. (2012, November). 3-D numerical and experimental models for flat and embedded heat pipes applied in high-end VGA card cooling system. *International Communications in Heat and Mass Transfer*, 39(9), 1360–1366. <https://doi.org/10.1016/j.icheatmasstransfer.2012.07.030>

What is the difference between a combination design and a split design for an experiment testing two independent variables at once on multiple levels? (n.d.). Quora. <https://www.quora.com/What-is-the-difference-between-a-combination-design-and-a-split-design-for-an-experiment-testing-two-independent-variables-at-once-on-multiple-levels-e-g-color-and-shape>

Whittaker, M. (2023, April 12). How Does Bitcoin Mining Work? Forbes Advisor. <https://www.forbes.com/advisor/investing/cryptocurrency/bitcoin-mining/>

Wright, C. S. (2008). Bitcoin: A Peer-to-Peer Electronic Cash System. SSRN Electronic Journal. <https://doi.org/10.2139/ssrn.3440802>

X.P. Yang, J. Liu, G.X. Wang, et al., Experimental study of mechanical-capillary driven phase-change loop for heat dissipation of electronic devices and batteries, *Appl. Therm. Eng.* (2022) 210, doi: 10.1016/j.applthermaleng.2022.118350 .

Yang, Z., Gu, J., Luo, X., Qin, Z., Zhou, S., Wang, P., & Zhao, W. (2024, February). An RSM approach to optimize the thermal performance of novel type vortex generators. Progress in Nuclear Energy, 167, 104978. <https://doi.org/10.1016/j.pnucene.2023.104978>

Z. (2020, November 9). What is Ethash? Zerocrypted. <https://zerocrypted.com/what-is-ethash/>

Zarnick, E. (2022, July 18). What Is A Good GPU Temperature Range? (How Hot Is Too Hot?). ScreenRant. <https://screenrant.com/good-gpu-temperature-range-explained/>



## APPENDIX A

### PSM GANTT CHART

| BMCU 4972 - UNDERGRADUATE PROJECT I (PSM I)   |                                    |      |    |    |    |    |    |    |    |    |     |     |     |     |     |     |     |
|---|------------------------------------|------|----|----|----|----|----|----|----|----|-----|-----|-----|-----|-----|-----|-----|
| GANTT CHART PLANNING  |                                    |      |    |    |    |    |    |    |    |    |     |     |     |     |     |     |     |
| PROJECT TITLE: Optimization of GPU Thermal Management Via Response Surface Methodology (RSM) Analysis |                                    |      |    |    |    |    |    |    |    |    |     |     |     |     |     |     |     |
| NO.   | TASK LIST                          | WEEK |    |    |    |    |    |    |    |    |     |     |     |     |     |     |     |
|   |                                    | W1   | W2 | W3 | W4 | W5 | W6 | W7 | W8 | W9 | W10 | W11 | W12 | W13 | W14 | W15 | W16 |
| 1   | PSM I Briefing                     |      |    |    |    |    |    |    |    |    |     |     |     |     |     |     |     |
| 2   | PSM Topic Selection                |      |    |    |    |    |    |    |    |    |     |     |     |     |     |     |     |
| 3   | PSM Topic Finalisation             |      |    |    |    |    |    |    |    |    |     |     |     |     |     |     |     |
| 4   | Preliminary Literature Review      |      |    |    |    |    |    |    |    |    |     |     |     |     |     |     |     |
| 5   | Progress Report Preparation        |      |    |    |    |    |    |    |    |    |     |     |     |     |     |     |     |
| 6   | Secondary Literature Review        |      |    |    |    |    |    |    |    |    |     |     |     |     |     |     |     |
| 7   | Seminar Slide Preparation          |      |    |    |    |    |    |    |    |    |     |     |     |     |     |     |     |
| 8   | Seminar Presentation               |      |    |    |    |    |    |    |    |    |     |     |     |     |     |     |     |
| 9   | Progress Report Submission         |      |    |    |    |    |    |    |    |    |     |     |     |     |     |     |     |
| 10  | Tertiary Literature Review         |      |    |    |    |    |    |    |    |    |     |     |     |     |     |     |     |
| 11  | Laboratory Test Selection          |      |    |    |    |    |    |    |    |    |     |     |     |     |     |     |     |
| 12  | Methodology Investigation          |      |    |    |    |    |    |    |    |    |     |     |     |     |     |     |     |
| 13  | Expected Test Result Investigation |      |    |    |    |    |    |    |    |    |     |     |     |     |     |     |     |
| 14  | Final Report Preparation           |      |    |    |    |    |    |    |    |    |     |     |     |     |     |     |     |
| 15  | Final Report Submission            |      |    |    |    |    |    |    |    |    |     |     |     |     |     |     |     |

**BMCU 4984 - UNDERGRADUATE PROJECT II (PSM II)**

**GANTT CHART PLANNING**

**PROJECT TITLE:** Optimization of GPU Thermal Management Via Response Surface Methodology (RSM) Analysis

| NO. | TASK LIST   | WEEK |    |    |    |    |    |    |    |    |     |     |     |     |     |     |     |     |
|-----|---|------|----|----|----|----|----|----|----|----|-----|-----|-----|-----|-----|-----|-----|-----|
|     |   | W1   | W2 | W3 | W4 | W5 | W6 | W7 | W8 | W9 | W10 | W11 | W12 | W13 | W14 | W15 | W16 | W17 |
| 1   | PSM II Briefing   |      |    |    |    |    |    |    |    |    |     |     |     |     |     |     |     |     |
| 2   | ASUS TUF GAMING 3060 GPU Set Up                                 |      |    |    |    |    |    |    |    |    |     |     |     |     |     |     |     |     |
| 3   | Preliminary Test Run  |      |    |    |    |    |    |    |    |    |     |     |     |     |     |     |     |     |
| 4   | Test run for fan speed optimization using stock thermal pad     |      |    |    |    |    |    |    |    |    |     |     |     |     |     |     |     |     |
| 5   | Actual run of experiment for stock thermal pad                  |      |    |    |    |    |    |    |    |    |     |     |     |     |     |     |     |     |
| 6   | Synthesis data obtained using RSM analysis                      |      |    |    |    |    |    |    |    |    |     |     |     |     |     |     |     |     |
| 7   | Prepare nickel thermal pad for upcoming test                    |      |    |    |    |    |    |    |    |    |     |     |     |     |     |     |     |     |
| 8   | Progress Report Preparation                                     |      |    |    |    |    |    |    |    |    |     |     |     |     |     |     |     |     |
| 9   | Progress Report Submission                                      |      |    |    |    |    |    |    |    |    |     |     |     |     |     |     |     |     |
| 10  | Actual Run of Experiment using nickel thermal pad               |      |    |    |    |    |    |    |    |    |     |     |     |     |     |     |     |     |
| 11  | Prepare copper thermal pad for upcoming test                    |      |    |    |    |    |    |    |    |    |     |     |     |     |     |     |     |     |
| 12  | Synthesization of data obtained for three types of thermal pad  |      |    |    |    |    |    |    |    |    |     |     |     |     |     |     |     |     |
| 13  | Final Report Preparation and Submission                         |      |    |    |    |    |    |    |    |    |     |     |     |     |     |     |     |     |
| 14  | Seminar Slide Preparation                                       |      |    |    |    |    |    |    |    |    |     |     |     |     |     |     |     |     |
|     | Seminar Presentation + Correction of final report if applicable |      |    |    |    |    |    |    |    |    |     |     |     |     |     |     |     |     |
| 15  | Hardbound Report Submission                                     |      |    |    |    |    |    |    |    |    |     |     |     |     |     |     |     |     |